DETECTION AND SYNCHRONIZATION OF DIRECT-SEQUENCE SPREAD-SPECTRUM SIGNALS

A Dissertation
Presented to
The Academic Faculty

By

Derrick A. Chu

In Partial Fulfillment
of the Requirements for the Degree
Doctor of Philosophy in the
School of Electrical and Computer Engineering
Department of Electrical and Computer Engineering

Georgia Institute of Technology

May 2022

DETECTION AND SYNCHRONIZATION OF DIRECT-SEQUENCE SPREAD-SPECTRUM SIGNALS

Thesis committee:

Dr. John R. Barry, Advisor
School of Electrical and Computer Engineering
Georgia Institute of Technology

Dr. Aaron D. Lanterman
School of Electrical and Computer Engineering
Georgia Institute of Technology

Dr. Xiaoli Ma
School of Electrical and Computer Engineering
Georgia Institute of Technology

Dr. Gordon L. Stüber
School of Electrical and Computer Engineering
Georgia Institute of Technology

Dr. Wenjing Liao
School of Mathematics
Georgia Institute of Technology

Date approved: February 10th, 2022

The final verdict will not be in the obituaries. The final verdict will be when the Ph.D. students dig out the archives, read my old papers, assess what my enemies have said, sift the evidence and seek the truth.

Lee Kuan Yew

To Xie Nan

ACKNOWLEDGMENTS

I would like to express my deepest gratitude to my advisor Professor John R. Barry. This dissertation would not have made it to its current state without his patient mentoring and constructive criticism. He has an uncanny ability to ask deceptively simple questions that stimulate deep, multi-dimensional thought. He has been very patient and supportive throughout the whole Ph.D. process despite my frequent mistakes, and he has my thanks for that.

I would like to thank my undergraduate advisor, Professor Benjamin S. Williams, along with my then mentor, Dr. Philip W.C. Hon, for putting up with my immaturity and incessant questions during my early years as an undergraduate researcher at UCLA. They were both instrumental in building my foundation as a researcher, and Philip showed me the grit needed to push through the tough times of Ph.D. I would also like to thank my then teaching assistant and later colleague Dr. Brad Chun-Ting Liu for teaching me the miscellaneous, but nonetheless important skills needed to navigate graduate school.

My words cannot express my gratitude towards my wife, Xie Nan, for being supportive throughout my Ph.D. while dealing with her own hardships in graduate school. There were certainly many trying times for both of us, and it was always Nan who was by my side. I would also like to thank Yael (Steven) J. Toporek for helping both Nan and me in the founding of the fabled NettieHutt group.

I would like to acknowledge both Pepper and Nettie, two cats of the Chu family that provided indispensable support over digital media. Pepper passed away while I was still in graduate school, and the mantle of feline support now passes to Nettie. Pepper will always be in our hearts.

Finally, I want to thank my family and my friends for being part of my life all these years. I couldn't have done it without you all.

TABLE OF CONTENTS

LIST OF TABLES

LIST OF FIGURES

SUMMARY

Recent technological advancements in material science and aerospace engineering have progressed the developments of hypersonic aircraft with air-breathing engines and in-atmosphere hypersonic weapons. These hypersonic vehicles, which travel at speeds of Mach five or faster, are expected to change the face of modern naval warfare, due to their ability to facilitate surgical strikes on well-defended capital ships. To better coordinate these types of operations on a global scale, modern militaries have a growing interest in low-earth orbit (LEO) satellite communications. Compared to their geosynchronous counterparts, LEO satellite communication has significantly lower latency and reduced deployment costs, which makes them attractive for both military and commercial application.

The high speeds and rapid movement associated with both LEO satellites and hypersonic vehicles makes direct-sequence spread-spectrum (DSSS) communication particularly challenging. Many conventional DSSS acquisition algorithms assume the Doppler frequency is small and constant, and that the frame length is sufficiently short that the effects of time-varying channel delays can be ignored. These assumptions hold in neither the LEO satellite channel nor the hypersonic vehicle channel, both of which are considered a high-dynamic communication environment due to the presence of both large time-varying Doppler frequency shifts and time-varying channel delays, and subsequently conventional algorithms have poor acquisition performance.

Even with the expected introduction of hypersonic aircraft into modern military arsenals, its task of reconnaissance and intelligence gathering does not change substantially. One method of performing reconnaissance is to deploy a detector that will determine if there are DSSS signals buried in a particular frequency band. This is a difficult task when key parameters such as the spreading sequence and the carrier frequency are unknown. To further exacerbate the difficulty of the problem, in military applications the spreading code period is often so long that the detector cannot exploit autocorrelative properties to perform detection, which severely limits the number of feasible detection techniques.

This thesis proposes strategies for both the acquisition of DSSS signals in high-dynamic environments, and the detection DSSS signals in a noncooperative context. In particular, we propose *delay-Doppler efficient exhaustive search* (DEES), an algorithm that can acquire DSSS signals in the presence of both Doppler rate and large Doppler frequency shifts. For the detection problem, we propose a multi-antenna likelihood-ratio-test detector that can detect quadrature phase-shift keying (QPSK) coded DSSS signals that does not require knowledge of the spreading code. While military communications serve as the chief motivator for this thesis, the detection and synchronization strategies presented are not limited to military application. For instance, QPSK signal detection has commercial application in spectrum sensing where a user or node must ascertain whether a portion of the spectrum is available for use, and reliable DSSS acquisition is a necessity for satellite-based broadband internet systems that make use of code-division multiple access.

DEES is a computationally efficient algorithm that can acquire direct-sequence spread-spectrum signals in high-dynamic environments. DEES combines the second-order keystone transform and the fractional Fourier transform to mitigate the time-varying effects of the channel, before jointly estimating both the code phase offset and the Doppler frequency. Based on numerical simulation results, DEES provides improved acquisition performance over existing FFT-based acquisition algorithms without the computational complexity of a three-dimensional maximum-likelihood exhaustive search.

For the noncooperative DSSS detection problem, this thesis investigates the advantage of a multi-antenna detector that knows the signal has QPSK coded chips, when the spreading sequence is unknown to the detector, and when the spreading code period is longer than the detector observation window. We propose a likelihood-ratio-test detector that takes advantage of knowledge of the signal alphabet, whose complexity grows linearly with the observation window length, and that makes use of multiple antennas. The proposed alphabet-aware detector outperforms multi-antenna alphabet-unaware detectors, especially when the SNR is high, and the observation window is small. However, the performance advantage is not large, it diminishes further when the SNR is low, and it comes at the cost of higher computational complexity. In most cases, simpler alphabet-unaware detectors such as the energy detector provide comparable detection performance with less complexity.

CHAPTER 1

INTRODUCTION

The face of warfare and armed conflict is inextricably shaped by the technology of the time period. The past three decades have seen a rapid development of military technology to the extent that in some cases their theoretical and conceptual developments outstrip existing literature on military strategy and tactics [1]. We focus on two main technologies of interest: the hypersonic vehicle, and low-earth orbit (LEO) satellite constellations.

A hypersonic vehicle refers to an object, typically a missile, spacecraft, or airplane, that moves at speeds in excess of Mach 5, or speeds five times greater than the speed of sound. By itself, hypersonic flight is not a new development, with the North American Aviation X-15 having completed the first successful hypersonic flight in the 1950s, and with other intermittent developments such as the Boeing X-37, an orbital test vehicle developed in the early 2000s [2]. Recently, there has been growing interest from militaries to further develop in-atmosphere hypersonic vehicles due to the massive strategic advantages they would provide [3, 4].

Broadly speaking, we can categorize hypersonic vehicles into two categories: hypersonic aircraft and hypersonic weapons. Hypersonic aircraft are capable of achieving and maintaining hypersonic speeds in-atmosphere without the aid of a mother ship; that is the aircraft is self-sufficient and do not require an external platform to ferry them to a certain altitude before they can engage in hypersonic flight. In comparison to their rocket-boosted cousins, hypersonic aircraft that make use of propulsion systems such as scramjets or ramjets are lighter weight, as their engines can make use of the oxygen in the atmosphere which means the aircraft does not have to carry a tank of oxidizer, have greater maneuverability since they can take advantage of aerodynamic forces and are not constrained by rocket thrust, and finally air-breathing hypersonic aircraft can sustain high speeds for longer as their engines are more fuel efficient [5, 6]. This thesis focuses exclusively on air-breathing hypersonic aircraft.

Hypersonic aircraft are expected to provide the next generation of military intelligence, surveillance and reconnaissance due to their ability to penetrate existing air defenses and with the growing number of counter-stealth technologies that call into the question the future survivability of existing stealth reconnaissance platforms. However, as of writing, technical challenges associated with the air-frame and propulsion system have prevented a hypersonic aircraft from being flown or even constructed [7, 8].

There are three classes of hypersonic weapons: ballistic missiles, boost-glide vehicles, and cruise missiles [4]. Hypersonic ballistic missiles have been around for decades, and are launched into space before diving back down to earth to close in on its target. They have predicable trajectories which makes them relatively easy to track by radar, and they can be intercepted by other missiles as a defensive measure. On the other hand, recently developed hypersonic boost-glide vehicles and hypersonic cruise missiles launches are much harder to detect, and have trajectories that are harder to predict when compared to hypersonic ballistic missiles.

Similar to hypersonic ballistic missiles, hypersonic boost-glide vehicles are first launched via rocket or other launch vehicle. However, instead of being launched into space, boost-glide vehicles are launched into the mesosphere, approximately 50 to 80 km in altitude, where it can re-enter the upper atmosphere and use aerodynamic lift to glide as it slowly descends in altitude and travels towards its intended target [3, 4]. One of the key characteristics of boost-glide vehicles is their exceptional maneuverability. Unlike either ballistic missiles or cruise missiles, the glider can maneuver in any manner necessary (energy permitting), which from the defender's perspective makes it difficult to ascertain what the boost-glide vehicle's intended target is and where defense action must take place. The lethality of hypersonic boost-glide vehicles is further underscored by their low altitude trajectory, which means they can evade early warning radar systems, and their exceptional

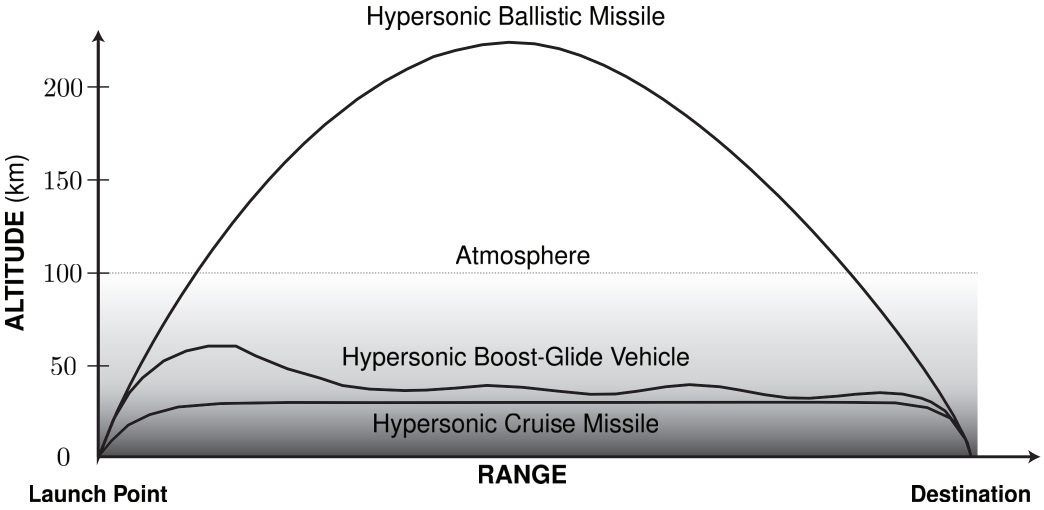

Figure 1.1: Typical flight trajectories of hypersonic weapons [4].

speed, which makes them difficult to detect and track by radar [4, 9].

Hypersonic cruise missiles are powered by supersonic ramjet and scramjet engines, and follow an even lower altitude flight path when compared to the boost-glide vehicle. Like the ballistic missile, the cruise missile has a relatively predictable trajectory as its travels at a nearly constant altitude and speed, but its low altitude coupled with its high speed allows it to skim under early warning radar systems, and by the time it is detected and tracked, there may be only precious moments to mount a defensive response. A summary of hypersonic weapon flight trajectories is shown in Fig. 1.1.

Naval warfare is one of the major arenas where both hypersonic weapons and hypersonic aircraft are expected to have a significant impact [1]. Hypersonic weapons greatly extend engagement ranges, and dramatically reduce the amount of time naval officers have to react and engage in defensive strategy. A coordinated and successful strike of hypersonic weapons against a carrier battlegroup could change the balance of naval forces in an entire theater in a matter of minutes. Furthermore, hypersonic aircraft could be used to not only safely perform reconnaissance on well-defended objectives, but they can also be used to deliver hypersonic weapons to perform surgical strikes on enemy carrier battlegroups. If aircraft-carrier-based hypersonic aircraft were feasible, they could be deployed from any major body of water and strike high value targets inland that are deep behind a web of air defenses.

Since hypersonic vehicles expands the scope of naval warfare, and increases time pressure for executive decision making, it is imperative that a reliable communication backbone is present such that naval vessels and other military units can coordinate with one another to mount an effective response. This could consist of coordinate between reconnaissance aircraft and the carrier battlegroup to determine if enemy forces have hypersonic cruise missiles that pose a serious threat to naval vessels, and that a preemptive strike is necessary while friendly forces have the element of surprise. Or it could be something more time sensitive such as communicating radar tracking information on an inbound hypersonic cruise missile to the relevant naval vessels within the battlegroup. While there are commercial communication systems that can be used in remote areas such as the open ocean, in practice the requirements of military communication systems are fundamentally different from commercial communication systems, and extend beyond geographical differences.

For one, it is difficult to predict geographically where exactly the next armed conflict will arise, so military communication networks are often ad hoc, multihop, rapidly deployable, and do not have the luxury of relying on well-planned infrastructure as commercial communication systems can. Military communication systems must also deal with contested electromagnetic spectrum; it is quite common for hostile forces to deploy jamming systems in an attempt to disrupt communication systems. Subsequently, military systems have a focus on low probability of detection (LPD), such that they may evade detection and deliberate jamming by hostile forces. In the event communication transmission are detected, the system is expected to have anti-jam and low probability of intercept (LPI) capabilities so to preserve tactical data links in jamming environments, and to secure data streams if they are intercepted by an eavesdropper. Finally, as military operations can span several theaters, communication systems must have a high degree of interoperability in joining space, naval, air, and land networks [10].

Satellite communications (satcom) are indispensable for global military operations due to their wide coverage, nuclear disaster survivability, anti-jamming capabilities, and their ability to utilize waveforms that have favorable LPD/LPI characteristics [11]. The framework for military satcom systems often consists of several ground stations, which are responsible for tracking, telemetry and control (TT&C), followed by the space constellation, which consists of several satellites that communicate with one another via crosslink and act as a network, and finally the user terminals which are terrestrial in nature, and can consist of naval vessels, fighter jets, or portable terminals carried by the warfighter. Historically, the military satcom systems have made use of satellites in geosynchronous (GEO) orbit. The main advantage of GEO satellites, which have an approximate altitude of $36,000$ km, is their stability, as their position relative to an observer on earth does not change, and the large coverage afforded by a single GEO satellite, which can cover entire geographic regions [11, 12].

This past decade has seen a growing interest in low-earth orbit (LEO) satellites for both military and commercial application [12, 13, 14, 15, 16, 17]. There are notable advantages afforded by LEO satellites that neither medium earth orbit (MEO) nor GEO satellites have. One of the main advantages of LEO satcom is afforded by the low $200-2000$ km orbit, which results in significantly lower latencies and reduced pathloss, which reduces transmit power requirements. This low latency makes LEO satellite a prime candidate for commercial internet service in areas underserved by terrestrial broadband, while the reduced transmit power requirements can improve LPD characteristics, making it attractive for military applications along with the reduced latency [12, 15, 17]. Furthermore, since radiation exposure is reduced at altitudes below 1000 km, LEO satellites are often smaller and lighter weight when compared to their MEO and GEO brethren, which lower constraints on launch vehicles and ultimately reduces deployment costs [13, 17]. LEO satellites can also be outfitted with a multiple spot beam antenna system, which is a system where a single antenna aperture produces multiple beams pointing in different directions. Along with the frequency reuse and multi-user advantage that this technology affords, it also improves the anti-jam capabilities of the communication system, as multiple spot beam satellites can more readily locate interference source compared to traditional single-beam satellites and respond accordingly [11].

Despite these LEO satellite advantages, there are several unique challenges associated with LEO satcom. Firstly, while the low altitude does substantially reduce latency, it also reduces the field of view and coverage of the satellite. This is often remedied by introducing a constellation of LEO satellites to serve a geographic area. However, unlike GEO or MEO satellites, LEO satellites have a short visibility window on the order of minutes [18], which requires that the user terminal rapidly synchronize with the LEO satellite during the initial transmission before handing off to another satellite as the original satellite leaves the terminal's visibility window [15, 19]. Secondly, LEO satellites have high relative velocities with respect to an observer on earth, which results in large time-varying Doppler frequency shifts, especially at high carrier frequencies [13, 15, 18, 20, 21]. Furthermore, the time-varying nature of channel can make it difficult for the transmitter to maintain accurate channel state information (CSI), which can hamper the performance of massive multiple input multiple output (MIMO) satellite systems [22]. A similar phenomenon can be found in the hypersonic vehicle channel [23]. Lastly, the LEO satellite channel is generally considered a multipath channel that undergoes Rician fading; this is due to the scattering from objects and physical features around the ground terminal [24, 25, 26, 27].

1.1 The Motivating Scenario

Up until this point, we have described hypersonic vehicles in a modern military context, and have shown their expected strategic importance in naval warfare. We have also described the advantages of satcom in military operations, and in-particular have pointed out the growing interest in LEO satcom. However, this thesis does not aim to discuss the change in

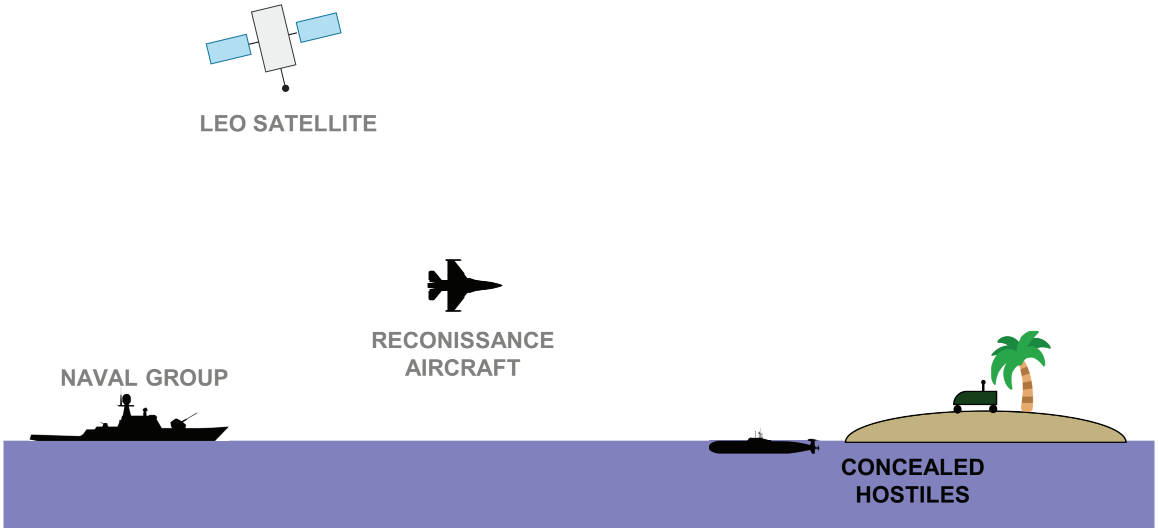

Figure 1.2: The motivating communication scenario. A naval vessel communicates with an aircraft performing reconnaissance on an island ahead of the naval fleet. The aircraft is unaware of the hostile forces on the island. A low-earth orbit satellite is used as a communication relay in the event the aircraft loses contact with naval command. Figure not drawn to scale.

strategy, tactic, or military doctrine that accompany these technological changes, nor will it attempt to evaluate the feasibility of deploying these technologies. Rather, it focuses on the communication problems that should be present if these technologies were deployed onto the battlefield, and proposes solutions to them.

Since the scope of any military operation is generally vast, we instead propose a hypothetical scenario inspired by the previous discussion and analyze the communication problems that are present.

We consider the hypothetical scenario shown in Fig. 1.2, which depicts a friendly naval battlegroup on the open ocean in the bottom left-hand corner, a friendly aircraft performing reconissance very far away from the naval battlegroup, and a friendly LEO satellite passing above. The enemy forces consist of a submarine and other anti-ship defenses situated on an island ahead of the naval battle group; the friendly forces are assumed to be unaware of their presence. The objective of the aircraft is to gather intelligence on the island, determine whether it is a neutral or contested region, then report its finding back to naval command. It may do so via a direct line of sight link, or in the event that is unavailable, it can utilize the LEO satellite as an intermediary.

Both enemy and friendly forces are assumed to utilize direct-sequence spread-spectrum (DSSS) communications. Spread-spectrum refers to a set of techniques in which a narrowband signal is spread in bandwidth in the frequency domain before transmission. In the case of DSSS, the narrowband signal is modulated by a pseudorandom sequence known as the spreading code, and the resulting spreaded signal has a lower power spectral density which makes it difficult to distinguish from noise. A receiver that has knowledge of the spreading sequence can take advantage of processing gain, which is equal to the ratio of the bandwidth of the spreaded signal to the bandwidth of the original narrowband signal, and “boost” the SNR of wideband signal by despreading it and recovering the narrowband signal in the process. Due to these favorable LPD properties, along with jam and multipath resistance, DSSS communications is a staple of military communication systems [28, 29]. While DSSS signals have been used in commercial code-division multiple access (CDMA) cellular systems, military DSSS communication systems generally have much higher processing gains, with certain signals buried 30 dB below the noise floor, and much longer spreading code periods; it is not unusual for spreading code periods to be on the order of 2^{26} or longer [30].

While the reconnaissance aircraft can make use of an active probing technique such as radar to determine whether hostile forces are present on the island, doing so removes any element of covertness that the aircraft has, and it could possibly be neutralized without having delivered mission-vital information back to command. Even if it did manage to avoid attack, its presence would alert enemy forces and any element of surprise that friendly forces had would now be lost. An alternative strategy is to utilize a passive detection technique. For instance, the aircraft may employ a detector that is designed to detect the presence of DSSS signals. The reasoning here is, if there are hostile forces present on this island, they are likely communicating with one another, and these communication signals can be detected. However, since friendly forces are unlikely to know the spreading sequence associated with the enemy's DSSS communication system, the detector is unable to take advantage of processing gain and "dig up" any potential signals buried in the noise, which makes this noncooperative detection task particularly difficult.

Nonetheless, once the aircraft has made a determination as to whether enemy communication signals are present, and subsequently hostile forces should be present near the island, it must relay this intelligence back to naval command. While the aircraft now has knowledge of the spreading sequence as it is an authorized user of the friendly communication system, it still must perform synchronization before it is able to communicate via the air-to-ship (AtS) channel or via LEO satcom. This can be a difficult task, as the LEO satellite channel is characterized by a time-varying Doppler frequency shift and time-varying channel delays. Furthermore, if the reconnaissance aircraft is traveling at hypersonic speeds, the AtS channel will suffer from similar Doppler effects. In either case, the naval vessel's onboard communication system needs to be robust enough to perform DSSS acquisition even in the face of large, time-varying Doppler frequency shifts, which is no trivial task.

We have identified two main communication problems in this hypothetical scenario: noncooperative DSSS detection and DSSS synchronization in high-dynamic environments. While the scenario depicted in Fig. 1.2 serves as a key motivation for this thesis, a realistic model that captures the minute details of both the AtS and LEO satellite channel, along with the intricacies of present or future state-of-the-art military communication systems is beyond the scope of this thesis. The reasons for this are twofold. Firstly, for obvious reasons, there is a lack of publicly available information regarding network protocols, key system parameters, physical waveform aspects and so forth for modern military communication systems. While there is unclassified information for legacy military communication systems, these systems are often too dated to provide guidance on more modern systems. At best, we can only speculate as to what features maybe present in such systems, and provide an educated guess as to what the relevant system parameters are. Secondly, while there have been several attempts to characterize the AtS channel, including several measurement campaigns, these have been performed with civilian aircraft which are significantly less agile than their military counterparts and are often restricted to subsonic speeds. In the case of hypersonic aircraft, there are no empirical channel measurements as such an aircraft has, as of writing, never even flown. This, along with the fact electromagnetic or physics-based simulations are beyond the scope of this thesis, severely dampens our ability to characterized the hypersonic vehicle channel beyond a surface level. Despite these limitations, we can still proceed in solving both problems of interest.

The aims of this thesis are as follows:

1. Identify key characteristics and impediments of the air-to-ship channel, with a focus on those that will greatly affect DSSS acquisition. Understand what additional channel impediments are present if the aircraft is traveling at hypersonic speeds.

2. Develop an algorithm that can acquire DSSS signals in high-dynamic environments where time-varying Doppler frequency shifts and time-varying channel delays are present. The low-earth orbit satellite channel is already known to exhibit these characteristics, and DSSS acquisition in such an environment becomes even more challenging with the long spreading codes typically utilized in military systems.

3. Develop a noncooperative DSSS detection technique that is applicable when the detector observation window length is smaller than the spreading code period, which is a reasonable assumption in the scenario of interest. In particular, this thesis investigates the performance advantage of an "alphabet-aware" multi-antenna detector, and knows the chip modulation scheme.

This thesis is organized as follows: Chapter 2 completes the first task in the previous list by taking a first-principles approach to gain intuition into the physical phenomena present, then by surveying existing AtS channel models and measurement campaigns. Chapter 2 also provides a literature survey of both noncooperative DSSS detection techniques, and DSSS acquisition techniques, and further elucidates aims two and three of this thesis. Chapter 3 introduces the core form of DEES, our proposed DSSS acquisition algorithm, while Chapter 4 augments the core form to be suitable for high-dynamic environments. Chapters 5 investigates the benefits of alphabet-awareness in noncooperative DSSS detection, and discusses several detection strategies that are viable when the detector observation window is short relative to the spreading code period. Finally, Chapters 6 summarizes the main contributions of this thesis and provides future direction.

CHAPTER 2

BACKGROUND AND LITERATURE SURVEY

This chapter is divided into three sections, each of which addresses one of the aims of this thesis discussed in the previous chapter. The first section discusses air-to-ship channel modeling and existing measurement campaigns, before delving into aspects of the hypersonic vehicle channel. The second and third section discuss direct-sequence spread-spectrum (DSSS) acquisition and noncooperative DSSS detection, respectively. For each section, we provide a comprehensive literature survey, along with the necessary background information needed to better understand the results presented later in this thesis.

2.1 Maritime Air-to-Ship Channel

To the best of our knowledge, there are no existing channel models for hypersonic aircraft operating in maritime environments, and due to the fact such aircraft have not yet been flown, there are no existing empirical measurements. However, there are several air-to-ship (AtS) channel models that exist if the aircraft is subsonic. We first provide a brief introduction of electromagnetic scattering theory to better understand the physical phenomena present in the channel, then move onto simplified multi-ray AtS models and existing measurement campaigns. Finally, we discuss potential plasma effects that should be accounted for when communicating with hypersonic vehicles.

As was discussed in the previous chapter, rigorous channel modeling is not an aim of this thesis. Rather, the goal of this section is to identify key characteristics of the AtS which will serve as guidance in developing a simplified time-varying channel impulse response $h(t, \tau)$. With a passband $h(t, \tau)$, an equivalent baseband channel model relating the transmit and receive signal samples can then be derived.

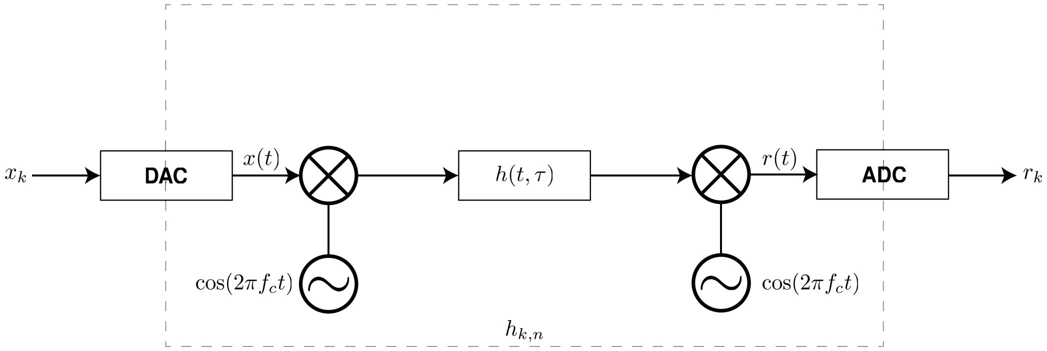

Figure 2.1: Block diagram of transmitter-receiver system model. Since both the source signal x_k and received signal r_k are digital, we can model an equivalent baseband channel with impulse response $h_{k,n}$.

An example of this is shown in Fig. 2.1; this model which will serve as the basis for modeling the baseband IQ samples r_k at the receiver and eavesdropper, in the case of the DSSS acquisition and noncooperative DSSS detection problems, respectively. Depending on the modulating symbol x_k, an IQ upconverter (and downconverter) is used in place of the single in-phase upconverter present in Fig. 2.1. Throughout this thesis, we will assume the analog to digital converters (ADC) and digital to analog converters (DAC) are ideal, and make use of ideal sinc pulses. Subsequently, other components present in the radio-frequency chain such as filter and amplifiers, have been ignored.

2.1.1 Scattering of Electromagnetic Waves from Rough Surfaces

We take a first-principles approach to better understand the physical phenomena that is present in the AtS channel. Once we have a handle on how electromagnetic waves propagate and scatter from rough surfaces, we can assess what existing AtS channel models are appropriate for the scenario in Fig. 1.2. We are particularly interested in rough surface scattering theory, as the ocean's surface is not perfectly smooth, and given that the wavelengths of radio-frequency electromagnetic waves are on the order of centimeters, it would not be appropriate to approximate them as such.

Consider a harmonic plane wave with unit amplitude incident on a rough surface described by the height function $\zeta(x, y)$. The electric field of the incident wave can be

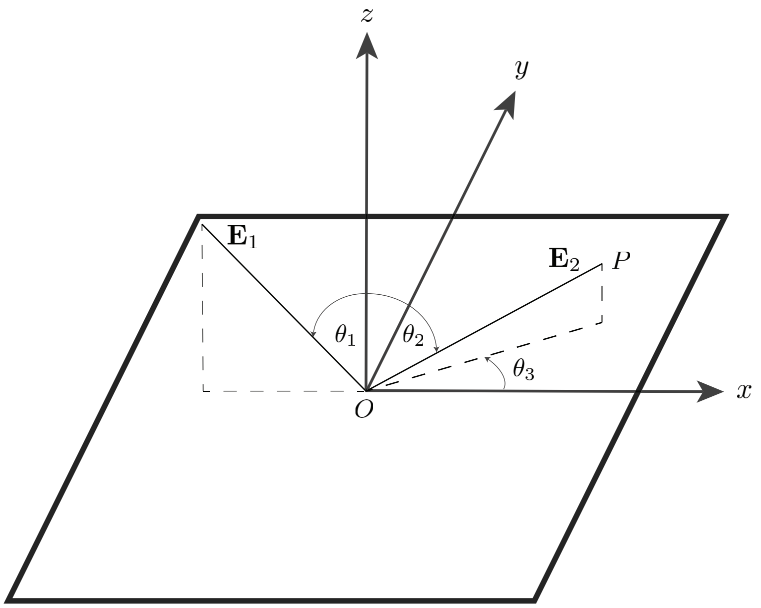

Figure 2.2: Scattering geometry with incident plane wave $\mathbf{E}_1$ and scattered wave $\mathbf{E}_2$.

described as:

$$\mathbf{E}_1 = e^{j\omega t} e^{j\mathbf{k}\cdot\mathbf{r}}, \tag{2.1}$$

where $\omega = 2\pi f$ is the radian frequency, t is the time variable, $\mathbf{r} = \langle x, y, z \rangle$ is the observation vector, and $\mathbf{k} = \langle k_x, k_y, k_z \rangle$ is the wavevector. The magnitude of the wavevector is equal to the wave number $|\mathbf{k}| = \sqrt{k_x^2 + k_y^2 + k_z^2} = 2\pi/\lambda$ where λ is the wavelength.

We can characterize the incoming wave as incident on the surface with some angle θ_1, and the reflected wave can be characterized with angles θ_2 and θ_3. This is shown in Fig. 2.2. Let P be an observation point a distance R' away from a point O on the surface $(x_0, y_0, \zeta(x_0, y_0))$. The scattered field $\mathbf{E}_2$ at point P is given by the Helmholtz integral [31, 32]:

$$\mathbf{E}_2(P) = \frac{1}{4\pi} \iint\limits_S \left(\mathbf{E}_1 \frac{\partial \psi}{\partial \mathbf{n}} - \psi \frac{\partial \mathbf{E}_1}{\partial \mathbf{n}} \right) dS, \tag{2.2}$$

where S is the reflection surface, $\mathbf{n}$ is the surface normal vector, and $\psi = e^{-jk_2 R'}/R'$. A closed form solution is generally not known for (2.2). However, for the case in which the surface's height follows a Gaussian distribution, there are closed-form solutions [31, 33].

A Gaussian scattering surface can be characterized by its height standard deviation σ_h and its surface correlation length l_{corr} [31, 33]. We consider a scattering surface of area $A = l_x l_y$ where l_x and l_y are large compared to the incident wavelength and surface correlation length [31, 33]. The scattering coefficient is defined as:

$$\rho = \frac{E_2}{E_{\text{spec}}} \tag{2.3}$$

where E_2 is the amplitude of the scattered field $\mathbf{E}_2$ and E_{spec} is the amplitude of a wave reflected by a smooth, perfectly conducting surface [31, 32, 33].

For an infinitely conductive surface the averaged scattered power is [31, 32, 33, 34]

$$\langle\langle \rho\rho^* \rangle\rangle = e^{-g}\left(\rho_0^2 + \frac{\pi l_{\text{corr}} F^2}{A} \sum_{m=0}^{\infty} \frac{g^m}{m!m} e^{-\frac{v_{xy}^2 l_{\text{corr}}^2}{4m}}\right), \tag{2.4}$$

where

$$\rho_0 = \text{sinc}(v_x l_x)\text{sinc}(v_y l_y), \tag{2.5}$$

$$v_x = k(\sin(\theta_1) - \sin(\theta_2)\cos(\theta_3)), \tag{2.6}$$

$$v_y = k(-\sin(\theta_2)\sin(\theta_3)), \tag{2.7}$$

$$v_{xy} = \sqrt{v_x^2 + v_y^2}, \tag{2.8}$$

$$F = \frac{1 + \cos(\theta_1)\cos(\theta_2) - \sin(\theta_1)\sin(\theta_2)\cos(\theta_3)}{\cos(\theta_1)(\cos(\theta_1) + \cos(\theta_2))}, \tag{2.9}$$

$$\rho_0 = \text{sinc}(v_x l_x)\text{sinc}(v_y l_y), \tag{2.10}$$

and

$$g = k^2\sigma_h^2(\cos(\theta_1) + \cos(\theta_2))^2. \tag{2.11}$$

The ρ_0^2 term in (2.4) describes the power contributions from specular scattering, while the second term in the sum in (2.4) describes the power contributions from diffuse scattering

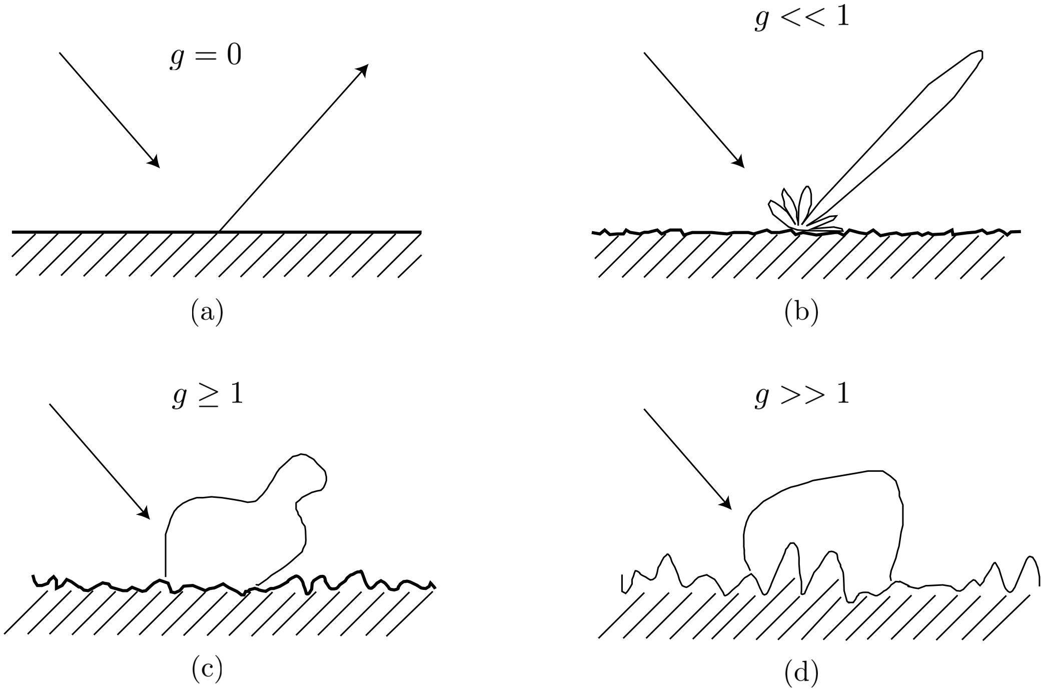

Figure 2.3: Effect of g on scattering electromagnetic wave scattering. The surfaces are: (a) smooth, (b) slightly rough, (c), moderately rough, and (d) very rough [31].

[33].

(2.11) defines g, a constant proportional to the surface roughness, which determines the proportion of the scattered wave that is specular or diffuse. For example, in Fig. 2.3, when g is small most of the scattered wave's power is from specular reflection. However, when g is large, the specular component largely disappears, and the scattered wave is dominated by diffuse scattering.

We have now established the basics of the Beckmann-Spizzichino rough surface scattering model, which can be used as a basis for simulating the time-varying channel impulse response $h(t, \tau)$. One possible simulation methodology is as follows. The transmitter and receiver are fixed at their locations of interest, and the surface between them is divided into a grid made up of equal-sized tiles of area A. Each tile is then excited with a plane wave whose incident angle is determined by the relative geometry of the tile of interest and the transmitter; the scattered power for that tile is then calculated at the receiver. As long as the dimensions of A are larger than the wavelength and correlation length, the total electric field at the receiver is the sum of all the contributions from each of the individual tiles [32, 33]. However, care should be taken such that each tile is significantly smaller than the distance between the transmitter and receiver, and that each tile is homogeneous in its electrical properties, e.g. it does not straddle a media boundary [32].

The aforementioned simulation methodology only represents the channel response at one particular time instance. The time-varying aspects of the channel can be simulated by moving the transmitter and receiver at each tick of the simulation clock, and recalculating the wave propagation and scattering.

2.1.2 Specular Reflection Models

Due to the complexity of the Beckmann-Spizzchino model, along with the computationally intensive simulations needed to generate the channel response, we now survey other maritime channel models that apply several simplifying assumptions to reduce model complexity. For example, several of these models calculate the specular and diffuse scattering contributions in a binary fashion, instead of having a smooth transition between the two as (2.4) suggests.

[35] describes an approach for calculating the bistatic microwave reflectivity of the sea surface at low grazing angles. While [35] does not provide an explicit time-varying channel impulse response $h(t, \tau)$, it does provide an approach for calculating the total received power in a rough sea environment that accommodates for other second-order effects such as finite-conductivity, surface curvature effects, and sea wave shadowing.

[35] asserts that along with the established line-of-sight (LoS) component that exists between the transmit and receive antennas, the none-line-of-sight (NLoS) contributions can be divided into three sub-categories: 1) specular reflection from the glistening region, 2) diffuse reflection from the glistening region, and 3) wide angle diffuse scattering. The glistening region refers to the general area if the LoS vector is projected onto the sea

surface, and contributes to most of the NLoS power. We specifically focus on the specular reflection portion of the model, since aside from very rough sea environments most of the reflected energy is due to specular contributions, and not diffuse [35, 36, 37]. The diffuse scattering as modeled in [35] has its roots in (2.4); the interested reader is referred to [35] for further reading.

We now describe a specular reflection model that accommodates for surface roughess, along with the curvature of the earth's surface, which must be accounted for when communicating over longer distances. This reflection model is not exclusive to [35], and has been discussed in [38, 39]. The specular reflection coefficient is:

$$\Gamma_s = \Gamma_0 \rho_s D \tag{2.12}$$

where Γ_0 is the Fresnel reflection coefficient, ρ_s is the surface roughness factor, and D is the spherical divergence factor.

The Fresnel reflection coefficients at a boundary interface for parallel and perpendicular polarization are [40, 41]:

$$\Gamma_{\parallel} = \frac{-\cos(\theta_1) + \sqrt{\frac{\epsilon_1}{\epsilon_2}}\sqrt{1 - (\frac{\epsilon_1}{\epsilon_2})\sin^2(\theta_1)}}{\cos(\theta_1) + \sqrt{\frac{\epsilon_1}{\epsilon_2}}\sqrt{1 - (\frac{\epsilon_1}{\epsilon_2})\sin^2(\theta_1)}}, \tag{2.13}$$

and

$$\Gamma_{\perp} = \frac{\cos(\theta_1) + \sqrt{\frac{\epsilon_2}{\epsilon_1}}\sqrt{1 - (\frac{\epsilon_1}{\epsilon_2})\sin^2(\theta_1)}}{\cos(\theta_1) - \sqrt{\frac{\epsilon_2}{\epsilon_1}}\sqrt{1 - (\frac{\epsilon_1}{\epsilon_2})\sin^2(\theta_1)}}, \tag{2.14}$$

where θ_1 is the incident angle measured from the surface normal to the incoming wave, where ϵ_1 and ϵ_2 refers to the complex permittivity of media one and media two, respectively, and where it was assumed $\mu_r = 1$ for both media. If media one is free space, then the ratio ϵ_2/ϵ_1 can be simplified as:

$$\frac{\epsilon_2}{\epsilon_1} \approx \epsilon_r - j60\lambda\sigma \tag{2.15}$$

where the approximation $1/2\pi\epsilon_0 c \approx 60$ was used, and where $\epsilon_0 = 8.854 \times 10^{-12}$ F/m is the permittivity of free space, and where $c = 3 \times 10^8$ m/s is the speed of light. While the relative permittivity and conductivity of sea water will depend on several factors such as frequency and salinity, in the microwave frequency range they may be approximated as $\epsilon_r = 80$ and $\sigma = 4$ mho/m [31, 35, 42].

The surface roughness factor is

$$\rho_s = e^{-\frac{p^2}{2}} I_0\left(\frac{p^2}{2}\right), \tag{2.16}$$

where

$$p = \frac{4\pi\sigma_H}{\lambda}\cos(\theta_1), \tag{2.17}$$

where $I_0(x)$ is the modified Bessel function of the zeroth order, and where σ_H is the root-mean-square (rms) wave height [38, 43]. For a calm sea σ_H is on the order of 0.01 m while for a rough sea σ_H is on the order of 1.03 m [31, 35]. From (2.16) and (2.12) it should be apparent that in this model, an increasingly rough surface attenuates contributions due to specular reflections. However, since there is no diffuse component in (2.12), a very rough surface in this model implies there are no reflection contributions. This is in contrast to the Beckmann-Spizzichino model in (2.4), which asserts that there is a smooth transition between specular and diffuse scattering depending on the surface roughness.

The spherical divergence factor, which must be accounted for when the separation between the transmitter and receiver is sufficiently large such that the curvature of the earth must be taken into account, is

$$D = \left[1 + \frac{2}{R_e \sin(\phi)} \frac{R_1 R_2}{R_1 + R_2}\right]^{-\frac{1}{2}} \tag{2.18}$$

where R_1 is the distance from transmitter to the specular reflection point, R_2 is the distance from the specular reflection point to the receiver, and R_e is the effective radius of the earth. ϕ is the angle subtended by the distance between the two terminals. The effective radius of the earth is larger than the actual radius of the earth in the microwave frequency range due to refraction in the atmosphere, and is $R_e = 8500$ km [35, 38, 39].

The specular reflection coefficient described in (2.12) accounts for surface roughness effects, finite conductivity, and earth curvature effects. In a calm sea environment, this specular reflection model when coupled with the LoS component results in a variation of the well-known two-ray model [44], which only differs from the classic one in the modeling of the reflection coefficient. There are other multi-ray models such as [45] that accommodate for evaporation ducts in tropical maritime environments, which increase the range of radio communications due to the waveguiding effect the duct has, or that accommodate for the diffuse scattering with a statistical model [46]. However, as will be seen in the next subsection which discusses empirical measurements, for a calm to mildly rough bodies of water, the contributions from diffuse scattering are minimal and a two ray model captures most of the effects.

2.1.3 Existing Channel Measurement Campaigns

In this subsection we briefly discuss the relevant results of several AtS measurement campaigns.

Several channel sounding campaigns involving a ground station near the shore line communicating with an aircraft or unmanned aerial vehicle (UAV) over the open ocean report a multi-ray channel model is consistent with measured data [36, 37, 47, 48]. The measurement setup in [37, 47] consists of a ground station communicating communicating with an S-3B fixed wing aircraft flying above the Pacific Ocean near Oxnard, CA. TThe measurements are performed at L-band ($960 - 977$ MHz) and ($5030 - 5091$ MHz). The aircraft engages in two flight patterns: the first consists of the aircraft flying directly away from the ground station in a straight line and at a fixed altitude, while the second consists of the aircraft flying an oval shaped pattern above the ocean. In both scenarios the aircraft maintains a fixed altitude of approximately 800 m and a fixed velocity of approximately 90 m/s. The maximum range between the aircraft and ground station is approximately 25 km for the oval shaped flying pattern and approximately 40 km for the straight line pattern. The angle of elevation from the ground station's perspective ranges from 2 to 40 degrees, and decreases the further the aircraft is away from the ground station.

The authors in [37, 47] state the channel can be modeled as a two-ray model with an intermittent third ray. The first ray is the LoS component between the ground station and the aircraft. The second ray is the specular reflected component from the ocean's surface, while the third ray is an intermittent component that arises from the scattering off clutter in the ocean such as large ships or platforms. The third ray was only present less than 2.5% of the time in measurement. The delay spread between the LoS component and the specularly reflected component was on the order of 70 ns but dropped to as low as 10 ns (minimum channel sounder resolution) as the aircraft flew further away from the ground station [37, 47]. The authors also state that ducting effects, which can reduce propagation loss to below free space levels, were largely absent during their measurement campaign. This is substantially different result from [48], which reports not only significantly evaporation ducting effects, but also reports multipath rays extending up to six rays. The presence of a significant evaporation duct could be explained due to the warmer climate in which the measurements were performed, while the multipath rays exceeding four were encountered a minority of the time ($< 1\%$ of measurements) and only when the UAV was operating at a low altitude of approximately 370 m [48, 49].

[36] reports a similar three ray phenomena as [37, 47] did. The measurement setup in [36] consisted of an aircraft flying at an altitude of approximately 760 m in a straight line away from a ground station, above the Pacific Ocean near Point Mugu, CA. The measurements were performed at 8.0 GHz. There were two sets of measurements taken,

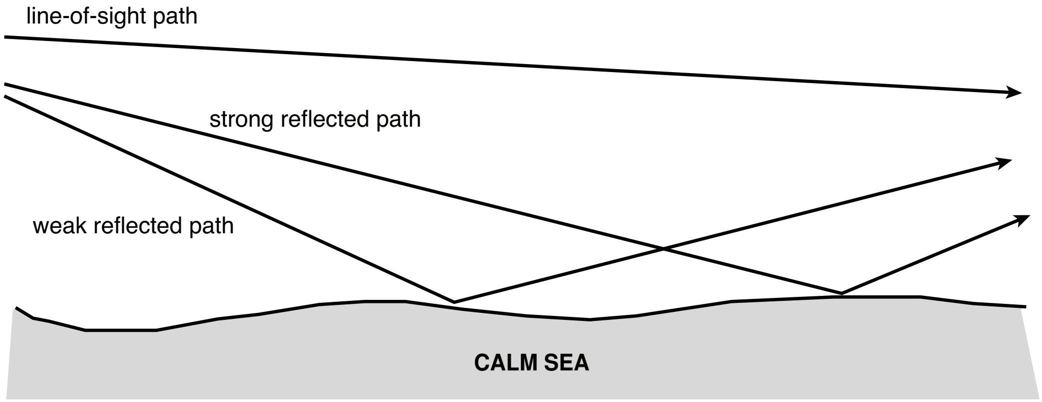

(a) Calm sea environment

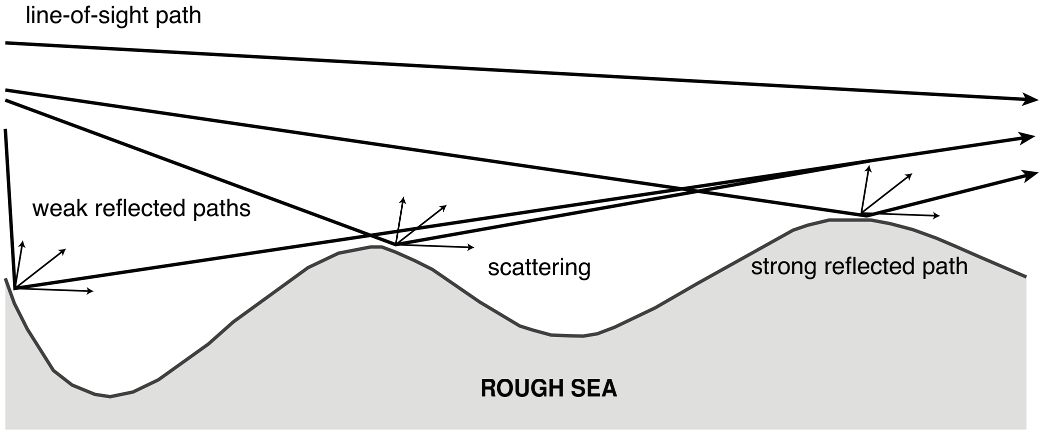

(b) Rough sea environment

Figure 2.4: Multipath ray contributions for (a) calm sea and (b) rough sea environments [36].

one in which the sea was in a calm state, and the other in a rough state. The calm sea measurements revealed a three ray phenomena similar to that in [37, 47]. The first multipath component is reported to have a mean normalized amplitude of 0.68 relative to the LoS component, while the third ray has a greatly reduced mean relative amplitude 0.06. For the rough sea measurements, the amplitude of the first multipath reflection is reduced to 0.52, while the third ray becomes more prominent in the power delay profile (PDP) and stronger in relative amplitude. Other weak multipath components are present in the rough sea environment due to diffuse scattering as visualized in Fig. 2.4(b). Based on the results in [36] the calm sea condition results in a more frequency selective channel.

2.1.4 Hypersonic Vehicle Channel

In this section, we discuss the adjustments to the AtS channel if the aerial platform is now a hypersonic aircraft. Since there are, as of writing, no existing empirical channel measurements, and the existing literature on in-atmosphere hypersonic aircraft from a channel modeling is somewhat sparse, there is a great limitation on knowing what physical phenomena maybe present at hypersonic speeds. However, it is certain that the high speeds will introduce Doppler effects to the channel, which will be discussed in the next subsection, while research from space re-entry vehicles suggest the plasma sheath could be present which will severely disrupt communications.

The plasma sheath refers to the layer of plasma that can form around a body that travels faster than hypersonic speeds and at high altitudes. The various shock waves that form at the front of a hypersonic vehicle will compress the surrounding air and heat it. This effect, coupled with atmospheric drag, can generate enough heat to dissociates and ionize surrounding molecules, which forms a sheath of plasma around the vehicle [50, 51, 52, 53, 54, 55]. The reader is referred to [56] for more information on how temperature, pressure, and density are affected due to the shockwaves at hypersonic speeds for a conical body.

One of the primary issues associated with the plasma sheath is communications blackout. The plasma sheath has been known to reflect and absorb electromagnetic radiation to the extent that it becomes impossible to communicate with the vehicle. This has been well documented with space re-entry vehicles such as the Apollo space capsules and during communications with the Columbia space shuttle [50, 52]. The attenuation caused by the plasma sheath can be significantly reduced by increasing the frequency of the incident electromagnetic wave such that it exceeds the plasma frequency (sometimes called the plasma resonant frequency or the electron plasma frequency) which is the frequency at which the electrons in the plasma oscillate at [51, 52, 57]. Even so, the plasma sheath has more communications impediments than just simple amplitude attenuation. The channel will experience large scale fading due to previous discussed reflection and absorption from the thickness of the sheath, and small scale frequency selective fading due to reflection, refraction, and inhomogenous properties within the plasma sheath itself [51, 57].

Given the adverse effects the plasma sheath has on communication and telemetry, several solutions have been previously proposed to mitigate plasma sheath effects. As stated previously, communication at frequencies above the plasma frequency can significantly reduce plasma sheath signal attenuation. However, the plasma frequency may be very high and require frequencies far above 15 GHz. As the frequency increases atmospheric absorption effects may be more pronounced, potentially mitgating “gains” from subverting the plasma sheath. Furthermore, antenna beamwidths at high frequencies are narrow, and it may be difficult for a ground station antennas to track the desired receiver [57]. We briefly discuss four other promising alternatives to high frequency communications: aerodynamic shaping, applied magnetic field, electrophilic injection, and plasma sheath matching. Aerodynamic shaping involves adjusting the shape of the hypersonic vehicle to have a sharper nose instead of a blunt one, thereby reducing the thickness of the plasma sheath and reducing the attenuation effect. However, this may not be possible in all cases, since a blunt-nosed hypersonic vehicle has more favorable thermal protective characteristics [58]. The application of a static magnetic field to the plasma sheath is another proposed solution. An externally applied magnetic field can confine the electrons within the plasma sheath, and create a “magnetic window” that can be communicated through [51, 52, 58]. However, the required magnetic field strength is usually quite large, and can be difficult to generate without equipment that may be impractically large or heavy for certain hypersonic vehicles [58]. Electrophilic injection involves the addition of gases or liquids that can reduce the plasma frequency by recombination of free electrons with the electrophilic materials [52]. Liquids such as water have already been experimentally tested with varying degrees of success [52, 58, 59]. Even so, the addition of large volumes of liquids or gases as a means of countering plasma sheath effects is still a prohibitive design point for hypersonic vehicles due to their weight [58]. Finally, [58] proposes a technique to impedance match the hypersonic vehicle’s antenna to the surrounding plasma sheath. While simulation results suggest in some conditions the matching technique can mitigate the effects from the plasma sheath and allow the antenna to radiate or receive freely, the matching bandwidth can severely constrain the communications bandwidth and induce dispersive effects if the matching bandwidth is not sufficiently large.

The characteristics of the plasma sheath are a complex function of a variety of factors, such as vehicle contour, altitude, Mach number, angle of attack, ablation rate, and so forth [51, 52]. For air-breathing hypersonic vehicles which operate in the Mach $6 - 10$ range and have operating altitudes from $25 - 30$ km, a communications blackout is generally not expected [52, 60]. Although there is a dearth of publicly available information for plasma sheath characteristics of hypersonic aircraft, they are expected to be relatively maneuverable, and make use of sharp leading edges which at the speeds and altitudes these vehicles are expected to operate at, which supposedly make the plasma sheath tenuous at best [54, 60].

2.1.5 Doppler Models

The previous discussion centered around multi-ray AtS channel models, but did not discuss the Doppler effects that would be present when communicating with fast moving aerial platforms such as hypersonic aircraft. This subsection will not attempt to formally augment the previously discussed models to accommodate for Doppler, nor will it discuss time-varying channel modeling in great detail, for which the reader is referred to [61]. Rather, this subsection discusses how time-varying Doppler effects arise for a simple LoS only channel, and also distinguishes between so-called "narrowband" and "wideband" Doppler models.

This subsection considers the following geometry for discussion. The transmitter is assumed to be stationary, while the receiver moves towards the transmitter with some velocity. Let $R(t)$ represent the instantaneous range between the transmitter and receiver. If the transmitter sends baseband signal $x(t)$, then the received baseband signal is:

$$r(t) = x(t - \tau(t))e^{-j2\pi f_c \tau(t)}, \tag{2.19}$$

where $\tau(t)$ is the time-varying channel delay, and f_c is the carrier frequency. If we adopt a second-order range model, then the instantaneous range is:

$$R(t) = R_0 + vt + \frac{1}{2}at^2, \tag{2.20}$$

where v is the initial velocity, and a is the constant acceleration. This polynomial range model is a consequence of kinematics and is independent of the delay model.

The main issue arises on how the time-varying delay $\tau(t)$ relates to $R(t)$. Two models are frequently presented in the literature: the so-called wideband Doppler model and the narrowband Doppler model [62]. In the former $\tau(t) = R(t - \tau(t))/v_p$, and in the latter $\tau(t) = R(t)/v_p$ where v_p is the wave propagation velocity. We will first discuss the wideband Doppler model in detail, then the narrowband model, which is considered as a special case of the former.

In the wideband Doppler model, sometimes called the exact model [63], the time-varying delay is related to the instantaneous range by the following relation:

$$\tau(t) = \frac{R(t - \tau(t))}{v_p}. \tag{2.21}$$

In comparison to radar literature, the factor of 2 is absent as there is no round-trip delay. Applying a Taylor series expansion to (2.21) and using (2.20), we can solve for $\tau(t)$ as:

$$\tau(t) = \alpha_w + \beta_w t + \gamma_w t^2 \tag{2.22}$$

where:

$$\alpha_w = \frac{R_0}{v_p}\big(1 - \frac{v}{v_p}\big), \tag{2.23}$$

$$\beta_w = \frac{v}{v_p}\big(1 - \frac{v}{v_p}\big) - \frac{aR_0}{v_p^2}, \tag{2.24}$$

$$\gamma_w = \frac{a}{2v_p} - \frac{3av}{2v_p^2}, \tag{2.25}$$

and where terms proportional to v_p^{-3} were ignored [63].

A particularly interesting phenomenon occurs to the received signal (2.19) when utilizing the wideband Doppler model. For simplicity we consider the case of constant velocity, which occurs when $a = 0$, and we assume radio waves are used, which means the wave propagation velocity is equal to the speed of light $v_p = c$. $\tau(t)$ can then be expressed as:

$$\tau(t) = \frac{R_0}{c + v} + \frac{v}{c + v}. \tag{2.26}$$

Substituting (2.26) into (2.19) yields:

$$\begin{aligned} r(t) &= x(t-\tau(t))e^{-j2\pi f_c \tau(t)} \\ &= x\Bigg(t-(\frac{R_0}{c+v}+\frac{v}{c+v}t)\Bigg)e^{-j2\pi f_c\left(\frac{R_0}{c+v}+\frac{v}{c+v}t\right)} \\ &= x\Bigg(\frac{c}{c+v}(t-\tau_0)\Bigg)e^{-j2\pi f_c\frac{c}{c+v}\left(\tau_0+\frac{v}{c}t\right)} \\ &= x(\mu_0(t-\tau_0))e^{j2\pi f_c\mu_0(\mu_0(t-\tau_0))}e^{-j2\pi f_c t} \end{aligned} \tag{2.27}$$

where $\mu_0 = c/(c+v)$, and $\tau_0 = R_0/c$.

The μ_0 term in (2.27) is called the Doppler stretch factor [64], and effectively time-scales the received signal [65]. If the receiver is moving towards the transmitter, then $\mu_0 > 1$ and the signal becomes compressed in time. If the receiver is moving away from the transmitter, then $\mu_0 < 1$ and the signal is stretched in time.

In practice it can be difficult to solve for $\tau(t)$ from (2.20) and (2.21), especially as higher order terms are adapted into the range model. We now consider the so-called narrowband Doppler model, which assumes (with no physical explanation) that the relationship between $R(t)$ and $\tau(t)$ is [62, 63]:

$$\tau(t) = \frac{R(t)}{v_p}. \tag{2.28}$$

The narrowband model is valid under the following conditions: (1) $|v/v_p| << 1$, and (2) $B/2 < f_c$ where B is the bandwidth of the transmitted signal [62]. In the context of pulsed radar this is the same as the “stop and hop” assumption, which is the assumption that the target of interest is static during the transmission and reception of a given radar pulse [63].

Assuming constant acceleration $\tau(t)$ is:

$$\tau(t) = \frac{R_0}{v_p} + \frac{v}{v_p}t + \frac{a}{2v_p}t^2. \tag{2.29}$$

When comparing (2.29) to (2.22), it can easily be seen that the narrowband Doppler model results in a significantly simpler $\tau(t)$.

In the case of a constant velocity, and $v_p = c$, the received signal for the narrowband model can be expressed as:

$$\begin{aligned} r(t) &= x(t-\tau(t))e^{-j2\pi f_c \tau(t)} \\ &= x\bigg(t\big(1-\frac{v}{c}\big)-\tau_0\bigg)e^{-j2\pi f_c(\frac{R_0}{c}+\frac{v}{c}t)} \\ &= x\bigg(t\big(1-\frac{v}{c}\big)-\tau_0\bigg)e^{-j2\pi f_c \tau_0}e^{j2\pi f_D t}, \end{aligned} \tag{2.30}$$

where f_D is the Doppler frequency. In comparison to (2.27), (2.30) does not have a Doppler stretch factor in either the signal or in the carrier phase term. (2.30) models the Doppler as a frequency shift, evidenced by the exp$(j2\pi f_D t)$ term. The wideband model instead has a frequency scaling due to the $\mu_0(t-\tau_0)$ in both the signal delay and in the carrier offset term [62].

Since this thesis is focused on radio-frequency communication ($|v/c| << 1$), and does not consider signal bandwidths on the order of the carrier frequency ($B/2 < f_c$), we make use of the narrowband approximation in modeling all Doppler effects.

2.2 Direct-Sequence Spread-Spectrum Acquisition

One of the first steps in direct-sequence spread-spectrum communications is synchronization. The receiver needs to obtain timing and frequency synchronization in order to properly despread and demodulate the received signal. Since the spreading sequences employed in DSSS communications often have “thumbtacky” autocorrelation characteristics and are designed to have low out-of-phase magnitude, a timing error of even a single chip duration is enough to prevent despreading at the receiver. Given the difficulty of initial synchronization, it is typically decomposed into a two step process. The first step is known as coarse acquisition, in which the receiver attempts to align its locally generated copy of the spreading code to within a chip (or fractions of a chip) with the received signal. The second step is known as tracking, in which the receiver makes use of several feedback mechanisms to maintain fine synchronization between the transmitter and receiver. As tracking loops are not the focus of this thesis, the reader is referred to [28, 66, 29] for additional information on standard techniques such as the delay lock loop (DLL).

Considering DSSS communication systems were developed as far back as World War II, and were declassified and available to the public as early as the 1970s, there exists a tremendous amount of literature on spread-spectrum synchronization [66]. We will briefly survey a few historic acquisition techniques that are pertinent to understanding spread-spectrum acquisition, before we discuss the more modern techniques in greater detail and identify gaps in their applicability.

2.2.1 Modeling the Acquisition Problem

To aid in our discussion of describing the DSSS acquisition problem, we will first introduce a received signal model. For the sake of discussion, suppose the continuous time baseband received signal is modeled as:

$$r(t) = \sqrt{P} d(t-\tau(t)) c(t-\tau(t)) e^{-j2\pi f_c \tau(t)} e^{j\phi'} + n(t), \tag{2.31}$$

where P is the instantaneous received power, $d(t)$ is the data signal, $c(t)$ is the spreading code signal, f_c is the carrier frequency in Hz, $\tau(t)$ is the time-varying channel delay, and $n(t)$ is AWGN. We can further simplify (2.31) by assuming a constant propagation delay, no data modulation, and no frequency uncertainty. These idealistic assumptions will be relaxed as the discussion progresses and in the subsequent subsection, but our current aims are to capture the essence of the acquisition problem. Applying these simplifications to (2.31) yields:

$$r(t) = \sqrt{P} c(t-\tau) e^{j\phi} + n(t), \tag{2.32}$$

where the constant phase terms have been amalgamated into the single exp(ϕ) term, and where τ represents the code phase offset. In this particular model, the code phase offset τ is synonymous with the constant channel delay. In practice, this is not the case as the shift registers that generate the local spreading code at the receiver will, assuming no a priori knowledge of the code phase offset, be initialized with random values. However, as the receiver is only concerned with aligning the locally generated code with the received signal, the contributions of either the channel or the shift register offset can often be abstracted by a single τ.

The spreading code signal can be modeled as:

$$c(t) = \sum_{k=0}^{N-1} c_k g(t - kT_c), \tag{2.33}$$

where c_k is the kth chip of the spreading sequence, T_c is the chip period, N is the period of the spreading code, and $g(t)$ is an amplitude shaping pulse. In practice, the sum limits in (2.33) may extend well beyond a single period when data modulation is present, the spreading code is short, or there is no absolute termination on the acquisition time. However, for burst communications, "push-to-talk" systems, or long spreading codes where it may be impractical to send multiple periods, (2.33) may be an accurate representation [67].

For historic reasons, acquisition can be thought of as a detection problem. This view can be seen from the serial search circuit, which searches over all possible code phase offsets in a sequential fashion. One possible realization of the serial search can be found in Fig. 2.5. The received signal is correlated with a spreading code shifted by the hypothesized code phase offset. The resulting signal is then passed through a bandpass filter (BPF) whose bandwidth is approximately $1/T_c$, then an envelope detector, and then finally integrated for T_d seconds. The result is then compared to a threshold. If it exceeds the threshold, the signal is considered acquired and the receiver proceeds to tracking. Otherwise, it is

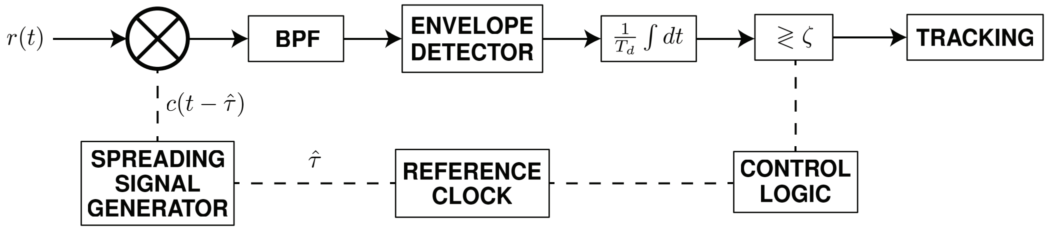

Figure 2.5: Topology of serial search circuit. Searches over all possible code phase offsets in a linear fashion.

assumed the candidate code phase offset is incorrect, the reference clock adjusts to select the new code phase offset, and the process repeats. Although such a device can be used to acquire a DSSS signal, it is seldom used in modern communications as a filter matched to the spreading sequence can accomplish acquisition faster than the system depicted in Fig. 2.5, and can do so with a smaller circuit footprint [29, 66].

In light of the previous discussion, it is more insightful to view acquisition as a two stage process: the first stage is the parameter estimation stage in which the receiver must estimate key parameters such as the code phase offset and the Doppler frequency. The second stage is the detection stage in which the receiver must determine, based on the estimated parameters, if the locally generated spreading code is sufficiently aligned with the received signal such that acquisition has been achieved, and the receiver can then proceed to the tracking phase.

If the acquisition process is performed digitally, that is $r(t)$ is sampled at the chip rate to produce a length N sequence r_k, then the estimation-detection view of acquisition can be formalized by the generalized likelihood ratio test (GLRT) [68]. The digitization of $r(t)$ also results in the discretization of the uncertainty space. For example, in (2.32), there would only be N possible candidate code phase offsets after sampling, where each candidate one corresponds to a particular cell. This one dimensional uncertainty region is visualized in Fig. 2.6.

As the name suggests, the GLRT is a generalized version of the LRT in which unknown parameters for each hypothesis are replaced by their maximum-likelihood estimates (MLE)

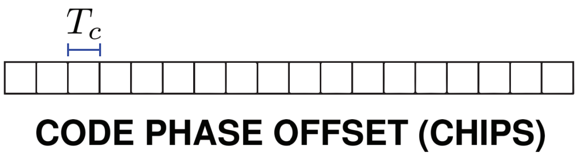

Figure 2.6: Visualization of the 1D uncertainty region corresponding to all possible code phase offsets.

[69, 70]. The GLRT decision statistic is:

$$\boldsymbol{\Lambda} = \frac{\arg\max\limits_{\boldsymbol{\theta}} f(\boldsymbol{r};\theta|\mathcal{H}_1)}{f(\boldsymbol{r}|\mathcal{H}_0)}, \tag{2.34}$$

where $\mathbf{r}$ is the vector of received signal samples, $\boldsymbol{\theta}$ is a vector of parameters consisting of the normalized code phase offset in chips, and the instantaneous received power P, the latter of which is considered a nuisance parameter in the acquisition problem, and where $\mathcal{H}_1$ is the hypothesis that the receiver has estimates of the parameters $\boldsymbol{\theta}$ that correspond with the aligned cells in the discretized uncertainty space, while $\mathcal{H}_0$ corresponds to all other misaligned cells. In practice, due to the favorable autocorrelation properties of DSSS signals, under $\mathcal{H}_0$ the distribution of $\mathbf{r}$ is only dependent on the noise [68, 71]. From (2.34) it should be apparent the estimation stage corresponds to the determination of the ML estimates under $\mathcal{H}_1$, while the detection stage consists of comparing the decision statistic itself to a threshold to determine if acquisition has been achieved.

Although it is intuitive to view the first stage of acquisition as the parameter estimation stage, we should emphasize that this is not a traditional estimation problem. Firstly, the goal here is not to obtain as precise of an estimate of the code phase offset (or any other parameter of interest) as possible; the estimate need only be sufficiently accurate such that it is within the pull-in range of the tracking loop. Secondly, the receiver is never actually certain if the DSSS signal is present before performing estimation, and subsequently the detection portion is still essential. Lastly, while (2.34) provides guidance on how to develop an acquisition module given a received signal model, it in no way captures the important performance metric of acquisition time T_{Acq}.

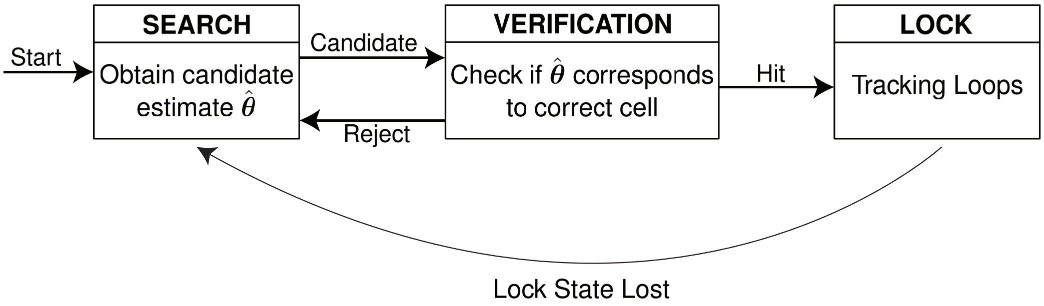

Figure 2.7: Summary of acquisition modes [74].

There are several classic techniques to improve the acquisition time in comparison to the serial search shown in Fig. 2.5. One way is to search the uncertainty region in a parallelized fashion. In essence, the aptly named parallel search consists of multiple branches where each branch correlates the received signal with spreading code $c(t - \tau_i)$ where τ_i is a candidate code phase offset. While the parallel search has rapid acquisition times in comparison to the serial search, it suffers from high computational complexity [29]. Rapid acquisition by sequential estimation (RASE) [72], and its subsequent improved versions [73], rely on making chip-by-chip decision on the sampled received signal, and use these decisions to seed the shift registers that generate the local spreading code. While RASE has acquisition times several linear factors shorter than the sequential search, and without the complexity of the parallel search, the technique is not feasible at low SNRs. We discuss more modern acquisition techniques that are feasible in the face of frequency uncertainty in the next subsection.

We close this subsection with a brief discussion of the different acquisition modes. The acquisition process is typically divided into three modes of operation [29, 68]:

1. The search mode.
2. The verification mode.
3. The lock mode.

When the acquisition module is in search mode, it is moving through the uncertainty region and develops an estimate of the parameter vector $\hat{\boldsymbol{\theta}}$. It then proceeds to the verification mode, where the candidate parameter cell(s) are now fixed, and where the receiver must determine if the candidate $\hat{\boldsymbol{\theta}}$ is sufficiently accurate such that the system can declare a lock and proceed to tracking. While we have described several search (parameter estimation) techniques, the receiver still has several degrees of design freedom in the verification (detection) stage. For example, in Fig. 2.5, the dwell or integration time T_d can be adjusted to reduce the probability of false-lock. A multi-dwell system can be utilized in which the output of the integrator must be passed through several detection stages before a lock can be declared. In the event that any of the detection stages do not have their thresholds exceeded, the detector declares acquisition has failed and returns to the search stage. Otherwise, if all detection stages pass, the receiver accepts $\hat{\boldsymbol{\theta}}$ as the correct estimate, and proceeds to tracking. If the system loses its lock state while tracking, it will return to the search stage and the process repeats. A summary of the acquisition modes is found in Fig. 2.7.

2.2.2 Modern Acquisition Techniques

We now discuss several modern DSSS acquisition techniques that are more computationally efficient and provider faster acquisition performance than the serial search shown in Fig. 2.5. Furthermore, these techniques are applicable to scenarios in which there is both code phase and frequency uncertainty. We begin with a simplification of the full received signal model in (2.31):

$$r(t) = \sqrt{P}c(t - \tau)e^{j2\pi f_D t}e^{j\phi} + n(t), \tag{2.35}$$

where it was assumed $\tau(t) = \tau_0 - \frac{v}{c}t$ follows a linear model, where v is the relative velocity between the transmitter and receiver and c is the speed of light. It was also assumed that since $|v/c| << 1$ the received signal's spreading code is offset by a constant amount, and does not experience a time-varying delay due to the $\frac{v}{c}t$ term [62].

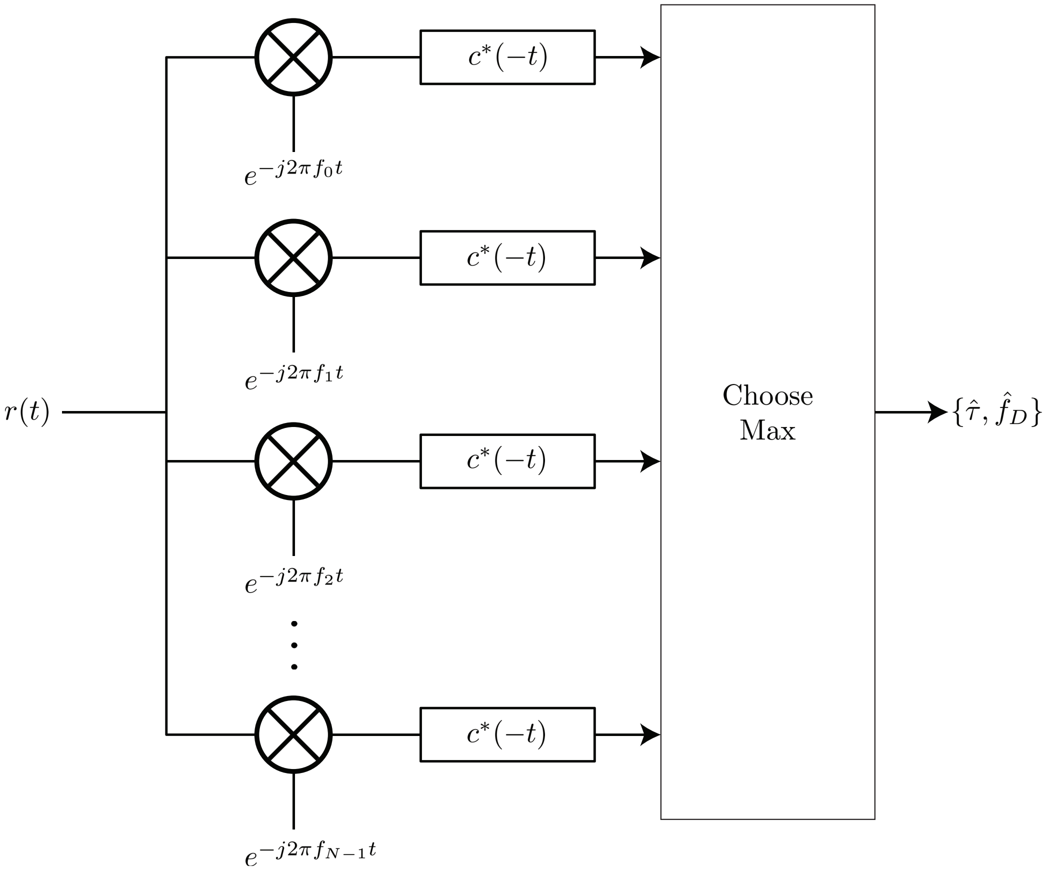

Figure 2.8: Implementation of the 2D exhaustive search in continuous time. The Doppler frequency and code phase offset estimate are obtained by selecting the branch with the largest correlation output.

As discussed in the previous subsection, the first stage of acquisition is the parameter estimation stage, where in this case the receiver must make a coarse estimate of both the code phase offset and the Doppler frequency $\{\tau, f_D\}$. Given that a linear search over all code phase offsets can be accomplished efficiently with a filter matched to the spreading code, it would seem intuitive to first compensate the received signal by the Doppler frequency. However, since the receiver rarely has a priori knowledge of f_D in the initial synchronization process, it must search for it. As there are now two variables that needs to be estimated, the uncertainty region is now 2D as visualized in Fig. 2.9.

One possibility is an exhaustive search over all possible Doppler frequencies. The received signal is first frequency shifted by one of the candidate Doppler frequencies f_i, and then passed through a filter matched to the spreading code. The branch with candidate

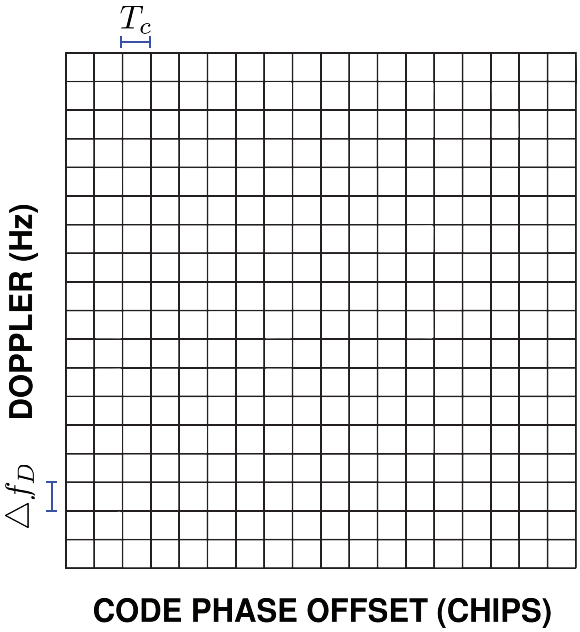

Figure 2.9: Visualization of the 2D uncertainty region corresponding to all possible code phase offsets, and all possible Doppler frequencies.

frequency f_i, closest to the actual Doppler frequency f_D, will result in the largest output as that branch will have the smallest residual Doppler shift. Thus selecting the largest output of all the branches will estimate the Doppler frequency $\hat{f}_D$, while the matched filter will estimate the code phase offset $\hat{\tau}$. Since it is impractical to search over all possible Doppler frequencies, the candidate Doppler f_i is typically drawn from a finite set $\{f_0, f_1, \ldots, f_{N-1}\}$. One possible implementation of this 2D exhaustive search is shown in Fig. 2.8. While this algorithm, up to quantization errors, is optimal [75], in practice its implementation is limited by its computational complexity.

We now survey several acquisition techniques that are capable of efficiently acquiring a DSSS signal and that have lower computational complexity when compared to the exhaustive search (or its discrete analog) shown in Fig. 2.8.

Double block zero padding (DBZP) is an acquisition algorithm that relies on partial circular correlations, block padding, and the FFT to jointly estimate the code phase offset and Doppler frequency. The algorithm is briefly summarized as follows: the received signal is first partitioned into N equal sized blocks. The $i + 1$th block is then duplicated and concatenated to the ith block, $i + 2$th block is duplicated and concatenated to the $i + 1$th block and so forth. The same is done for the local spreading code, except zeros are padded onto each block instead of concatenation. The partial circular convolutions of every two blocks of the received code and every two blocks local code is are then performed, and the results stored in a matrix. This process is repeated for all permutations of the local code, until all possible code phases have been tried. Then a column-wise FFT is performed on the matrix to efficiently search for the correct Doppler frequency. There are several other renditions of DBZP, such as modified versions to deal with data modulation or complexity improvements [76, 77].

General zero padding (GZP) is another spread-spectrum acquisition algorithm, originally designed to directly acquire the precision spreading code used in GPS. GZP is briefly summarized as follows: The received signal is segmented into equal sized blocks each of length N, then zero padded with N zeros. The received signal is then correlated with a local spreading code, and the first N samples of the result are incoherently integrated and tested against a threshold. If the test statistic exceeds a threshold, acquisition is declared, otherwise the next batch of samples from the received signal are tested. Search over for the Doppler frequency is accomplished by circularly shifting the local spreading code code. Since frequency shift is accomplished by exploiting this DFT property, the frequency resolution is limited to $\triangle f = 1/NT_s$ in which T_s is the sampling frequency. The interested reader is referred to [30, 78, 79] for more details.

There are several other spread spectrum acquisition methods that involve a technique known as “code-folding”, in which sections of the spreading code are “folded” onto itself in order to reduce the number of code phases to be searched. Some of these techniques include XFAST [80, 81], as well as dual-folding based algorithms such as the one in [82]. While these techniques present faster methods to acquire the phase of the spreading code, they do not provide substantial improvements to code Doppler estimation, especially when compared to DBZP. In fact the dual code folding acquisition scheme presented in [82] still uses the circular shift technique utilized in [78]. The interested reader is left to references [80, 81, 82] for more information.

In [83, 84, 85] a spread spectrum acquisition technique based on partial-matched-filtering (PMF) and the FFT is presented. The algorithm works by segmenting the length M spreading code into P filters, each of which contain X chips of the total spreading code. P must be chosen such that it is an integer, and $XP = M$. In the absence of any a priori information about the phase of the spreading code, the whole received signal must be passed through each of the PMFs to produce P total partial correlations, which are then stored in a matrix. The receiver then takes the FFT and magnitude of this matrix, and then selects the largest peak. Based on the indices of the rows and columns, the receiver is able to determine the associated code phase offset and Doppler frequency. However, [83, 84, 85] does not discuss the applicability of PMF-FFT to a multipath channel or a RAKE receiver, and do not discuss design trade-offs associated with the number of partial filters P.

[86, 87] describe a frequency domain based approach to PMF-FFT spread spectrum acquisition. Instead of proceeding with matched filtering and convolution in the time domain as [83] did, the authors instead make use of the short-time-Fourier-Transform (STFT) with variable window sizes as well as an STFT “inverse” to rapidly compute the partial correlations. However, the authors of [86, 87] state that in general an overlapping window leads to a decrease in detection probabilities and an increase in false alarm probabilities.

In contrast to the previous acquisition algorithms, which broadly speaking perform partial correlations before engaging in Doppler processing, there exists another class of acquisition algorithm that make use of differential processing [88, 89, 90]. Although these algorithms vary in their implementation, the basic idea is to delay the received signal by a chip and correlate it with itself. The resulting output is then correlated with a one-chip delay-correlated version of the local spreading code before proceeding to additional processing. The advantage of this differential processing is the effects of Doppler offset and data modulation are removed, while the correlation properties of the spreading code are still maintained. The drawback of differential processing based algorithms is they have poor acquisition performance with weak signals [68, 90].

Up until this point we have discussed DSSS acquisition techniques that are applicable when the Doppler frequency is constant, and the code phase offset is static, which is how $r(t)$ in (2.35) is modeled. While this is often a valid assumption in terrestrial commercial communications, it does not hold when the Doppler frequency is high, the spreading code is long [30, 91], and/or if the Doppler is time-varying. We first discuss the case in which the code phase offset varies linearly with time, and then shift the discussion to quadratically time-varying code phase offsetse and time-varying Doppler.

As the previous discussion has shown, while there are an abundance of techniques that can acquire DSSS signals with static code phase offsets, however, there are comparatively fewer that are applicable when the code phase varies linearly with time. [91] describes circularly correlation with multiple data bits (CCMDB) algorithm, which as the name suggests relies on circular correlations and coherent accumulations to perform acquisition. CCMDB handles the linearly time-varying code phase offset and Doppler frequency shift by producing multiple Doppler-compensated replicas of the spreading code, each one compensated by a candidate Doppler frequency. To reduce computational burden, at each step of the algorithm CCMDB discards Doppler bins that are unlikely to contain the correct Doppler. CCMDB handles data modulation by estimating the most likely sequence of data bits and compensating accordingly. For details the interested reader is referred to [91]. [92] takes a different approach and augments an existing modified DBZP algorithm to remove the time-varying effects from post-correlation matrix. [92] proposes the use of stretch processing and generalized keystone transforms to mitigate the time-varying effects, and noncoherent integration before estimating relevant parameters. [93] proposes a two stage acquisition algorithm where in the first stage the keystone transform is utilized

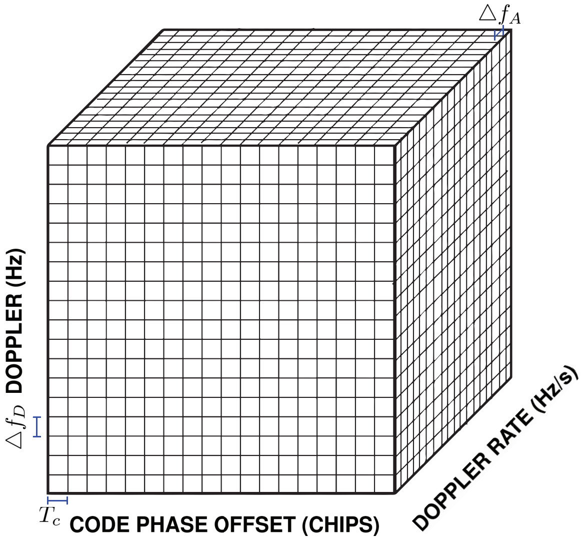

Figure 2.10: Visualization of the 3D uncertainty region corresponding to all possible initial code phase offsets, all possible initial Doppler frequencies, and all possible Doppler rates.

to compensate for linear code phase drift and prolong coherent integration times, while in the second stage the Doppler frequency is estimated using differential detection.

There are even fewer techniques that are viable when there is a time-varying Doppler frequency shift. When the Doppler rate is high and/or the spreading code is long, this can result in a time-varying code phase offset that has both a linear and quadratic component. These so-called high-dynamic environments have been reported in low-earth orbit (LEO) satellite communications [15, 18, 20, 21], along with hypersonic vehicle and space communications [94, 95, 23]. The introduction of a non-zero Doppler rate expands the uncertainty region by yet another dimension as seen in Fig. 2.10. The acquisition system must be designed such that the initial Doppler frequency resolution $\triangle f_D$ and the Doppler rate resolution $\triangle f_A$ are precise enough to be within the pull-in range of the tracking loops. Otherwise, the system will fail to maintain a lock and will return to the acquisition mode due to the poor initial Doppler estimates.

[96, 97] proposes an algorithm based on the fractional Fourier transform (FrFT) to estimate and compensate for Doppler rate in DSSS signals. [97] discusses the optimal FrFT bin that should be chosen in relation to the Doppler rate. [98] uses a convex optimization

algorithm to estimate the code phase and Doppler frequency assuming the Doppler rate is constant.

There have been several techniques pioneered in the field of radar signal processing that can estimate and compensate for target acceleration (proportional to Doppler rate), before jointly estimating the range and velocity [99, 100, 101, 102]. These techniques make use of various transforms such as the Radon-fractional-Fourier transform [103], modified-axis-rotation transform with Lv's transform [99], time-reversing-transform (TRT) [100], and keystone transform [101, 102, 104, 105]. While many of these techniques can estimate and compensate for a non-zero Doppler rate, they are all developed under the assumption that the transmitted signal is a linear frequency modulated (LFM) chirp, and many use specific properties of LFM signals [106] which makes them unsuitable for DSSS acquisition.

As this brief survey of DSSS acquisition techniques have shown, there are a vast number of existing techniques that are applicable when the Doppler frequency is constant and the code phase offset is static. While there are a handful of techniques that can accommodate for linearly time-varying code phase offsets, there are relatively few that can do so when the Doppler frequency shift is also time-varying. Given the relative dearth of acquisition algorithms viable in high-dynamic environments, we focus our efforts in developing one that can acquire DSSS signals in the face of both time-varying Doppler frequencies and quadratically time-varying code phase offsets.

2.3 Existing Noncooperative Direct-Sequence Spread-Spectrum Signal Detection Techniques

Noncooperative detection of direct-sequence spread-spectrum (DSSS) signals is generally difficult since the detector has no knowledge of key parameters such as the spreading sequence, the chip rate, or the type of spreading code used, and subsequently cannot easily detect the presence of the DSSS signal buried in noise [28, 66, 107, 29]. We emphasize

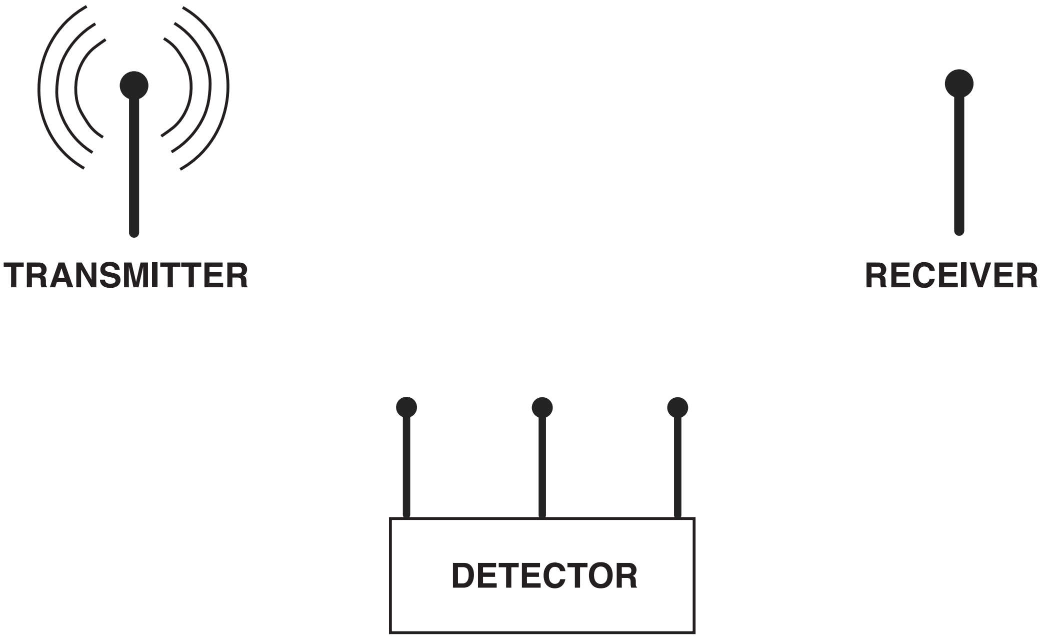

Figure 2.11: Visualization of the noncooperative detection problem. The detector deployed by the eavesdropper must make a determination if a signal is present in its noisy observations.

that this is a *detection* problem and not an interception problem. It is sufficient for an eavesdropper to determine the presence of the DSSS signal in noise; it is not necessary to demodulate the information-bearing bits.

In such a problem it is typical to assume that the transmitter is unaware of the eavesdropper's presence, and subsequently does not employ any countermeasures when delivering its payload to the authorized receiver [28, 29]. A setup of this can be seen in Fig. 2.11.

The detection problem can be phrased in terms of a binary hypothesis test:

$$\begin{cases} \mathcal{H}_1 : r_k = s_k(\boldsymbol{\theta}) + n_k \\ \mathcal{H}_0 : r_k = n_k \end{cases} \tag{2.36}$$

where r_k represents the baseband IQ samples at the detector, n_k is AWGN, and s_k is the signal from the transmitter modified by some vector of parameters $\boldsymbol{\theta}$. Under the alternative hypothesis $\mathcal{H}_1$, the received signal consists of signal and noise, while under the null hypothesis $\mathcal{H}_0$ there is just noise.

One strategy to derive a detector decision statistic is to apply the likelihood ratio test (LRT) to the problem in (2.36), which by the Neyman-Pearson lemma results in the optimal detector [69, 70, 108]. However, the LRT can only be applied to (2.36) if the PDFs under both hypotheses are completely known. This is rarely the case, as the distribution of the vector $\boldsymbol{\theta}$, which models unknown such as channel effects, is generally not known to the receiver and presents direct application of the LRT.

It is possible to develop a test that is independent of the unknown vector $\boldsymbol{\theta}$, and is normally performed in an ad hoc fashion. If such a test is optimal in the Neyman-Pearson sense, then it is referred to at the uniformally most powerful (UMP) test and can be computed independent of $\boldsymbol{\theta}$. However, the UMP test seldom exists, and in many cases the vector $\boldsymbol{\theta}$ must be handled directly [69, 70, 108].

There are two primary approaches that are viable in the event $\boldsymbol{\theta}$-independent test fails. The first is to assume a distribution for the unknown vector $\boldsymbol{\theta}$ and apply the LRT as usual. There are two drawbacks to this approach: the first is if $\boldsymbol{\theta}$ has large dimensionality it can be difficult to derived a closed-form likelihood-ratio, and the second is even if a detector statistic can be derived, its performance is highly dependent on the assumed distribution. An alternative approach is to apply the generalized likelihood ratio test (GLRT), which models the unknown under each hypothesis as deterministic, and replaces them with their maximum-likelihood estimates [69, 70, 108]. While there is no general optimality condition associated with the GLRT, in practice it can work quite well [108].

Despite the favorable low probability of detection (LPD) characteristics of DSSS signals, they are not impervious to detection by an eavesdropper [28, 29]. Depending on the amount of a priori knowledge known and the structure of the signal, there are several techniques that may be used to noncooperatively detect a DSSS signal and even estimate its spreading sequence. We first discuss a plethora of techniques which we will broadly categorize as “correlation-based”. Generally speaking these techniques exploit some aspect of the autocorrelation function of the spreading code, and require that the detector observation window length be longer than the spreading code period. We then discuss other detection techniques that do not have such a stipulation on the detector observation window length. For brevity, we will refer to the case in which the observation window length is longer than the spreading code period as the “long window” case, and the case in which the observation window length is shorter than the spreading code as the “short window” case.

2.3.1 Correlation-Based Detection Techniques

Since there are a wide variety of detection techniques that exist under our umbrella term of “correlation-based”, we first discuss techniques that are specifically developed for short spreading codes, which are spreading sequences with a period equal or shorter then the symbol duration. We then shift the discussion to detection of long-code DSSS signals, where the spreading code period is longer than the symboling period [28].

There are several short-code DSSS signal detection techniques. [109] proposes a technique that relies on the fluctuations of autocorrelation estimators derived from windowed segments of the received signal to be greater when a DSSS signal present as opposed to when one is absent. [110, 111] improve upon this algorithm with averaging and wavelet transformation augmentations; the end result is improved detection performance at low SNR. [112] proposes an delay-multiply based autocorrelation technique that makes use of a wavelet transform. [113] uses an FFT-based technique that exploits the autocorrelative properties of the short spreading code to detect the DSSS signal. Explicit knowledge of the carrier frequency is assumed. [74, 114] proposes a semi-blind detection based on eigenanalysis. The carrier frequency and spreading code period is assumed to be known.

Once the DSSS signal has been detected, a reasonable next step for the eavesdropper is to estimate relevant signal parameters. These can include, but are not limited to, the chip period, the symbol period, the carrier frequency, the spreading code period, and even the spreading sequence itself. [74, 115, 114] describes two different methods to approximate the period of a short spreading code using eigenanalysis and windowing-correlation based technique. [116] suggests a technique to estimate the carrier frequency of the detected DSSS signal assuming M-PSK modulation.

There have been several attempts to estimate a short code's spreading sequence from the detected DSSS signal. [117] proposes a low SNR eigenanalysis method to estimate the spreading sequence. The paper proves for a short spreading code the concatenation of eigenvectors corresponding to the segmented received signal's correlation matrix is the spreading code used to spread the signal. [118] proposes a low complexity iterative algorithm to estimate the spreading code sequence. [119] makes improvements to this algorithm such that performance does not degrade with increasing spreading code length.

The detection and estimation of long-code DSSS signals is substantially more difficult. This is because the period of the spreading code is longer than the symbol period, and the polarity changes of the signal within a given spreading code period can damage the autocorrelative properties of the spreading sequence [119, 120]. For this reason [120] introduces an information symbol transition matrix to overcome this problem, then makes use of eigenanalysis to estimate the spreading sequence. [119] proposes a "missing-data" model which allows one to model a long-code DSSS signal as a short-code DSSS signal with missing data (zeros). A slightly modified short code spreading sequence estimation algorithm is then used. [107] presents a long-code estimation technique that explicitly exploits properties of maximal-length sequences. [121] presents a blind algorithm to determine if the detected DSSS signal uses a long or short spreading code.

Given the previous discussion, there exists an abundance of techniques that can noncooperatively detect DSSS signals and even estimate the spreading sequence for the long window case. However, military DSSS communication systems use very long spreading codes which would make it impractical for an eavesdropper to make use of any of these correlation-based techniques.

2.3.2 Detection Techniques for Short Windows

There are comparatively fewer detection techniques that an eavesdropper can utilize for the short window case. We now provide a brief survey of a few of them.

[122] describes a phase-shift keying (PSK) detection technique whose complexity grows linearly with observation window length, does not require knowledge of the noise variance, but only takes advantage of a single antenna for detection. The detection technique, which the authors name the "simplified generalized likelihood ratio" (S-GLR) achieves similar performance as a detector derived from the universally most powerful invariant (UMPI) test. [123] proposes a cyclostationary detector which looks for cyclic features at integer multiples of the chip period and symbol period. However, the detection technique requires the signal have excess bandwidth at the detector, and also requires oversampling with at least two samples per chip for reasonable detection performance. There are several multi-antenna signal detection techniques that have been pioneered for passive radar applications and that provide substantial performance benefit over their single-antenna counterparts [124, 125, 126, 127, 128], but they either assume the signal is unknown or require knowledge of the transmitted sequence to perform detection.

The energy detector (ED), also known as a radiometer, is well-studied and has seen widespread use due to its versatility. The ED does not require any a priori knowledge of the signal, has low computational complexity, but suffers from performance degradation in the face of noise uncertainty [74, 129, 130, 131, 132, 133, 134, 135]. If there is any degree of uncertainty surrounding either the noise statistics or noise power, the detection threshold could be set sub-optimally, and performance may suffer as a result [130]. Lastly, an energy detector normally needs a long observation window length and stable noise floor to detect a DSSS signal at low SNR while still maintaining a low false-alarm rate [136].

The advantage of a detector that has knowledge of the signal alphabet or signal structure has received considerably less attention in the literature. [137] showed that at low SNR an ED has similar performance to a Neyman-Pearson optimal single-antenna detector that knows the signal alphabet. In [138] an ED is shown to have similar performance to a detector that knows the signal has an OFDM structure. However, to the best of our knowledge the relative performance of multi-antenna alphabet-unaware and multi-antenna alphabet-aware detectors has not been reported in the literature.

Given the inherent difficulty of noncooperative DSSS detection, coupled with the fact military communication systems employ long spreading codes which make it impractical to use a correlation-based detection technique, an eavesdropper should exploit every possible advantage to improve detection performance. In particular, we consider the case in which the detector does not have knowledge of the spreading sequence, the type of spreading code used, or the modulating information bits. On the other hand, we assume the detector is “alphabet-aware”, that is it does have a priori knowledge of the modulating chips. We focus in on the specific case of QPSK modulated chips, and explore the advantage of an multi-antenna alphabet-aware detector and compare its performance to other multi-antenna alphabet-unaware detectors. While there is existing work that explores PSK-specific detection techniques such as [122], along with a comparison of BPSK detection to ED at low SNRs in the context of cognitive radio [137], to the best of our knowledge there is *no prior published work* that addresses the added dimension of multiple antennas at the detector.

2.4 Summary

In this chapter we have surveyed many existing air-to-ship channel models, empirical measurements, along with electromagnetic wave scattering theory. We have ascertained that the air-to-ship channel has several multipath components, where the chief multipath component is the specular reflection from the sea surface in a calm sea environment. Other intermittent multipath components arise from diffuse scattering from objects on the ocean surface, or in the case of a rough sea from the waves themselves. However, the diffuse power contributions are often small when compared to specular contributions in calm sea conditions, and generally are stochastic in nature. When the distance between the transmitter and receiver is sufficiently large, the curvature of the earth must also be taken into account; this large distance reduces the intensity of specular reflection. Large Doppler shifts are present due to the relative motion of the hypersonic vehicle with respect to the ship, but can still by characterized by the narrowband Doppler model. For air-breathing hypersonic vehicles operating around Mach $6 - 10$ and with altitudes around $25 - 30$ km, the plasma sheath is thin and tenuous at best.

Given the vast existing literature for direct-sequence spread-spectrum acquisition, we have surveyed but a small portion. Despite the abundance of existing techniques, the vast majority of them are only applicable in the face of constant Doppler frequency, and static code phase offsets. We have identified few techniques suitable for acquisition in an environment characterized by both time-varying Doppler frequency shifts and time-varying channel delays, which are key characteristics of high-dynamic communication environments such as LEO satcom.

Finally, we have surveyed noncooperative direct-sequence spread-spectrum detection techniques. While there are many existing detection techniques, most of them rely on exploiting the autocorrelative properties of the spreading code, and subsequently require that the detector observation window is longer than the spreading code period. These detection techniques are generally unsuitable for detecting military communication systems, which employ long spreading codes as a countermeasure. While there are techniques that do not have rely on the autocorrelative properties of the spreading code, there is no known prior published work that explores the advantage of a multi-antenna detector that knows the signal alphabet.

CHAPTER 3

DSSS ACQUISITION FOR STATIC CODE PHASE OFFSETS

In this chapter, we develop a computationally efficient DSSS acquisition technique that is applicable to scenarios in which the channel Doppler frequency is constant, and the code phase offset is static. As the previous chapter has shown, there are several existing techniques such as DBZP [139, 76] or PMF-FFT [83, 84, 85] that can be used to efficiently acquire a DSSS signal under the aforementioned conditions. However, many of these techniques were developed in an ad hoc fashion, lack certain channel estimation abilities which may be useful to the receiver outside of spread-spectrum synchronization, and their applicability to multipath environments such as the AtS channel has not been explored.

We propose the *core form* of delay-Doppler efficient exhaustive search (DEES), an efficient algorithm that can acquire DSSS signals in a multipath channel environment with constant Doppler, and that can also provide secondary channel estimation capabilities. We derive core DEES from the optimal exhaustive search, and compare the performance of both of these algorithms via numerical simulations.

It is contradictory to discuss DSSS acquisition in a channel in which the code phase offset is static and the Doppler frequency is constant, since it is physically impossible to have a static code phase offset and a non-zero Doppler frequency [62, 64]. Despite this, the constant-Doppler-static-code-phase-offset model is often used when the Doppler frequency shift is small, and the frame length is sufficiently short such that the time-varying effects of the channel can be ignored. In the following chapter, we will expand the DSSS acquisition problem to high-dynamic communication environments in which both the code phase offset and the Doppler frequency is no longer static. We will then augment the core DEES algorithm to be applicable to such harsh channel environments.

3.1 Received Signal Model

It is typical to decompose spread-spectrum synchronization into a two step process: the first is coarse acquisition and the second is fine tracking. As was shown in Chapter 2, we can further decompose the coarse acquisition step into estimation and detection stages. In this chapter, we focus on the estimation portion of acquisition.

We assume a simplified received signal model in which the baseband IQ samples at the receiver are:

$$r_k = \alpha x_{k-d_0} e^{j\omega_D k} + n_k, \tag{3.1}$$

where α is an unknown complex channel gain, $\omega_D = 2\pi f_D T_c$ is the normalized radian Doppler frequency, f_D is the Doppler frequency in Hz, T_c is the chip period, $f_s = 1/T_c$ is the sampling frequency, and the components of the noise vector n_k are *i.i.d.* $\mathcal{CN}(0, 2\sigma^2)$. The transmitted binary DSSS signal x_k is assumed to be known to the receiver, and is non-zero only for $k \in \{0, 1, \ldots, L-1\}$. To handle non-integer code phase offsets d_0, we define $x_{k-d} = \sum_n x_n \text{sinc}((k-n)-d)$; for readability this interpolating sinc is suppressed. We assume that the code phase offset is restricted to the range $d_0 \in \mathcal{D} = \{-d_{\text{max}}, \ldots, 0, \ldots, d_{\text{max}}\}$ but is otherwise unknown, and that the normalized Doppler frequency ω_D is restricted to the range $|\omega_D| \leq \omega_{\text{max}}$, but is otherwise unknown.

The model introduced in (3.1) has some limitations, but it captures the essence of DSSS acquisition. In practice, there may be a multipath channel, in which case we can view our model as the contribution from one particular channel path. In practice there will also be an extra constant phase factor of $e^{-j2\pi f_c d_0 T_c}$ where f_c is the carrier frequency in Hz, but it does not appreciably change the problem, and thus has been omitted to simplify notation.

This chapter is concerned with the following problem: Given knowledge of the received signal model in (3.1), estimate the parameters $\{d_0, \omega_D\}$ that maximizes the statistic:

$$z = \left| \sum_{k=-\infty}^{\infty} r_k x^*_{k-\hat{d}_0} e^{-j\hat{\omega}_D k} \right|^2, \tag{3.2}$$

where $\hat{d}_0$ is the estimate of d_0 and $\hat{\omega}_D$ is the estimate of ω_D.

3.2 Derivation of the core DEES Algorithm

In the following we will derive the core DEES algorithm from a simplified version of the received signal model in (3.1), and then we will slowly address some of the practical limitations of the model. We proceed in four stages: (1) we remove α from the picture by temporarily assuming $\alpha = 1$; (2) we start with an exhaustive 2D search over all possible code phase offsets and Doppler frequencies, and derive an efficient implementation based on a bank of partitioned matched filters and the FFT; (3) we relax the $\alpha = 1$ assumption, and modify the algorithm to also estimate α; (4) we relax the single-path assumption, and modify the algorithm to accommodate for a multipath channel and RAKE receiver.

When $\alpha = 1$, the maximum-likelihood (ML) estimates for ω_D and d_0 can be found from an exhaustive search over all possible candidate code phases and Doppler frequencies, where for each candidate Doppler frequency ω and code phase d the received signal r_k is multiplied by $e^{-j\omega k}$, then correlated with the delayed spreading code x_{k-d}. This is equivalent to the nested optimization:

$$\{\hat{\omega}_D, \hat{d}_0\} = \arg\max_{\omega, d} \mathrm{Re}\{\sum_k e^{-j\omega k} r_k x^*_{k-d}\} \tag{3.3}$$

where $\mathrm{Re}\{\}$ takes the real part of its argument. Alternatively, the ML Doppler estimate can be expressed explicitly as a nested optimization:

$$\hat{\omega}_D = \arg\max_{\omega} \max_{d} \mathrm{Re}\{\sum_k e^{-j\omega k} r_k x^*_{k-d}\}, \tag{3.4}$$

where the ML delay estimate would be the value of d that maximizes the inner expression when ω is the value that maximizes the outer maximum. The advantage of this alternative form is that the inner optimization can be implemented efficiently using a matched filter. In particular, the value of d that maximizes the inner sum can be found by passing $e^{-j\omega k} r_k$

through a filter matched to x_k, producing the output

$$\tilde{y}_k = e^{-j\omega k} r_k \ * \ x^*_{-k}, \tag{3.5}$$

and choosing d as the time instant at which the real part of the MF output achieves its maximum value.

Since x_k is of length L, we can select an integer N that divides L evenly, and partition the length L signal into N segments, each of length L/N. In particular, let us define the nth segment, for $n \in \{0, 1, ..., N-1\}$, by

$$x_k^{(n)} = x_{k+L/N} w_k, \tag{3.6}$$

where w_k is the rectangular window $w_k = 1$ for $k \in \{0, 1, \ldots, L/N - 1\}$, and $w_k = 0$ for other k. According to this definition, all segments are non-zero only for k in this same interval. A visualization of this can be seen in Fig. 3.1(a), which shows a generic signal partitioned into N segments, and Fig. 3.1(b) which shows the rectangular window w_k. In terms of these segments, the original transmitted signal can be decomposed into the sum:

$$x_k = \sum_{n=0}^{N-1} x^{(n)}_{k-nL/N}. \tag{3.7}$$

Furthermore, in terms of the signal segments, the matched filter output of (3.5) can be written as:

$$\begin{aligned}\tilde{y}_k &= e^{-j\omega k} r_k \ * \ x^*_{-k} \\ &= e^{-j\omega k} r_k \ * \ \sum_{n=0}^{N-1} x^{*(n)}_{-k-nL/N} \\ &= \sum_{n=0}^{N-1} e^{-j\omega(k+nL/N)} r_{nL/N+k} \ * \ x^{*(n)}_{-k}.\end{aligned} \tag{3.8}$$

The last line of (3.8) describes a parallel implementation of the length-L MF, in which the

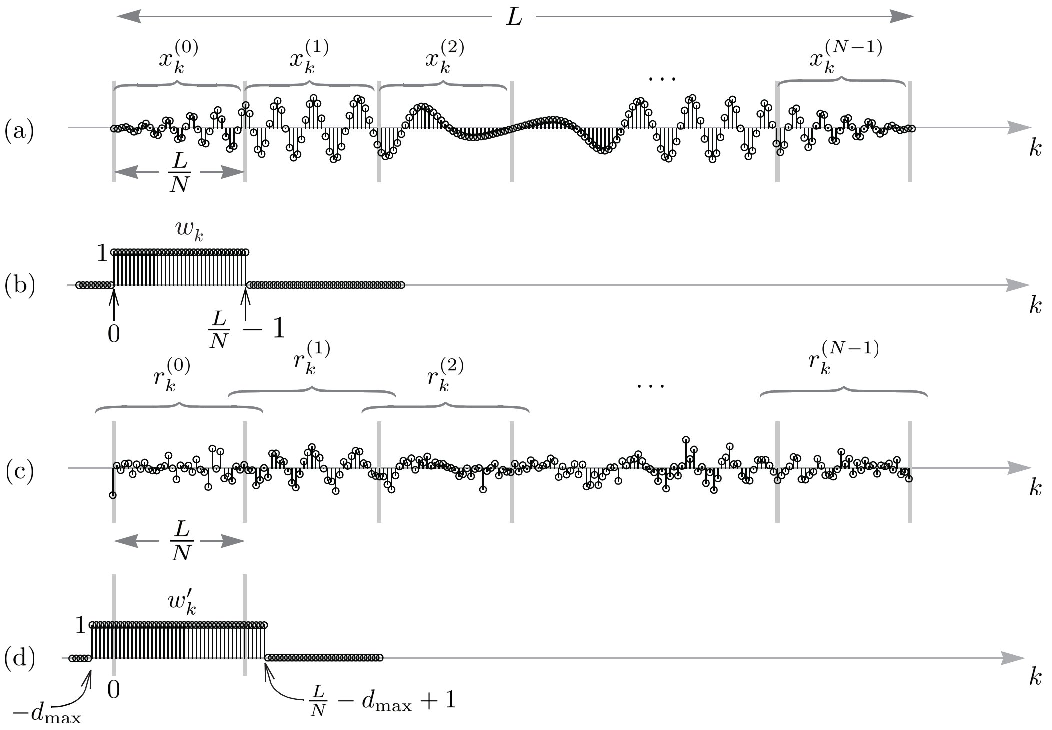

Figure 3.1: Time domain plots of (a) generic signal x_k partitioned into N segments, (b) windowing function w_k, (c) received signal r_k partitioned into N overlapping segments, (d) windowing function w'_k.

MF output is computed by adding the outputs of a bank of N matched filters, each of length L/N, one for each signal segment.

The fact that the d is restricted to $\mathcal{D}$ implies that we need not compute the MF output $\tilde{y}_k$ for all possible k; rather, $\tilde{y}_k$ need only be evaluated for $k \in \mathcal{D}$. When k is restricted in this manner, we can replace the input $e^{-j\omega(k+nL/N)}r_{k+nL/N}$ to the n-th segment MF by a windowed version that explicitly discards the irrelevant portions of the received signal, namely:

$$\tilde{r}_k^{(n)} = e^{-j\omega(k+nL/N)}r_{nL/N+k}w'_k, \tag{3.9}$$

where w'_k is a unit-height rectangular window that is non-zero only in the interval $k \in \mathcal{I}' = \{-d_{\text{max}}, \ldots, L/N + d_{\text{max}} - 1\}$. A visualization of the segmented received signal and w'_k can be found in Fig. 3.1(c) and Fig. 3.1(d), respectively.

3.2.1 Constant-Phase Approximation

A key step in our derivation is to recognize that, when the window w'_k in (3.9) is sufficiently short, or equivalently when the candidate normalized Doppler ω is sufficiently small relative to the window length $L/N + 2d_{\text{max}}$, the phase factor $e^{-j\omega k}$ in (3.9) will be approximately constant over the duration of the window, taking the same value throughout the duration of the window that it takes at time $k = 0$. We denote this as the constant-phase approximation (CPA). Under CPA, we can approximate the factor $e^{-j\omega k}$ by 1 in (3.9), so that the input to the n-th MF can be written as:

$$\tilde{r}_k^{(n)} \approx e^{-j\omega nL/N} r_{nL/N+k} w'_k. \tag{3.10}$$

The importance of this approximation stems from the fact that the time-varying phase term multiplying the input to the n-th MF has been replaced by a constant $e^{-j\omega nL/N}$, independent of time k. We can therefore move this constant factor from before each MF to *after*. In particular, instead of feeding $\tilde{r}_k^{(n)}$ as the input the n-th MF, we can instead feed the following signal as the input to the n-th MF:

$$r_k^{(n)} = r_{nL/N+k} w'_k, \tag{3.11}$$

and then multiply the signal coming out of the n-th MF by the constant $e^{-j\omega nL/N}$ before adding. Thus, while we began with an exhaustive search that first compensates for Doppler, segments the result, and then feeds these segments to a bank of MF's, the approximation of (3.10) allows us to perform these functions in reverse order, namely, to first segment the received signal, feed the segments to a bank of MF's, and compensate for the Doppler afterwards.

Let $y_k^{(n)}$ denote the output of the n-th MF at time k, when the uncompensated segment $r_k^{(n)}$ from (3.11) is its input. We can then approximate the output of the overall MF in

(3.8) by multiplying each segmented MF output by the appropriate constant before adding, yielding

$$y_k = \sum_{n=0}^{N-1} e^{-j\omega nL/N} y_k^{(n)}. \tag{3.12}$$

For k fixed, this can be viewed as a sampled DTFT of the MF bank outputs $y_k^{(n)}$, viewed as a function of n. For the special case when the set of candidate frequencies ω is restricted to be of the form $\omega = 2\pi m/L$ for $m \in \mathcal{M} = \{0, \pm 1, \ldots, \pm(N/2-1)\}$, (3.12) reduces to the discrete-Fourier transform, since then:

$$y_k = \sum_{n=0}^{N-1} e^{-j2\pi mn/N} y_k^{(n)}, \tag{3.13}$$

can be viewed as the m-th DFT coefficient of the vector $[y_k^{(0)}, ..., y_k^{(N-1)}]$. Thus, instead of performing an expensive search over all possible Doppler frequencies, N candidate Doppler frequencies can be simultaneously searched with a single instance of the DFT, which can be efficiently implemented with an FFT [140].

A block diagram of one possible implementation of the core DEES algorithm is shown in Fig. 3.2. The received sequence r_k is partitioned into N segments, and each segment $r_k^{(n)}$ is passed through a filter matched to that segment of the spreading code, with impulse response $x_{-k}^{*(n)}$. The MF outputs are then collected into a $N \times D$ matrix $\mathbf{Y}$, where the entry in row $n \in \{0, 1, ...N-1\}$ and column $k \in \mathcal{D}$ is $y_k^{(n)}$, and where $D = 2\lceil d_{\text{max}} \rceil + 1$. From the $N \times D$ matrix $\mathbf{Y}$ we create the $N \times D$ matrix $\mathbf{Z}$ by taking the FFT of the columns of $\mathbf{Y}$.

The maximum normalized Doppler frequency tested by the FFT is $2\pi(N/2-1)/L$. To prevent aliasing we must have $N > \omega_{\text{max}} L/\pi + 2$, where $\omega_{\text{max}} = 2\pi f_c T_c b_{0,\text{max}}$ is the maximum normalized radian Doppler frequency. This places a lower bound on the number of segments needed. On the other hand, the DFT resolution, with no zero-padding, is given by $\triangle f = 1/(LT_c)$. In other words, the maximum normalized Doppler frequency tested is affected by the choice of N, but the frequency resolution is independent of the number of

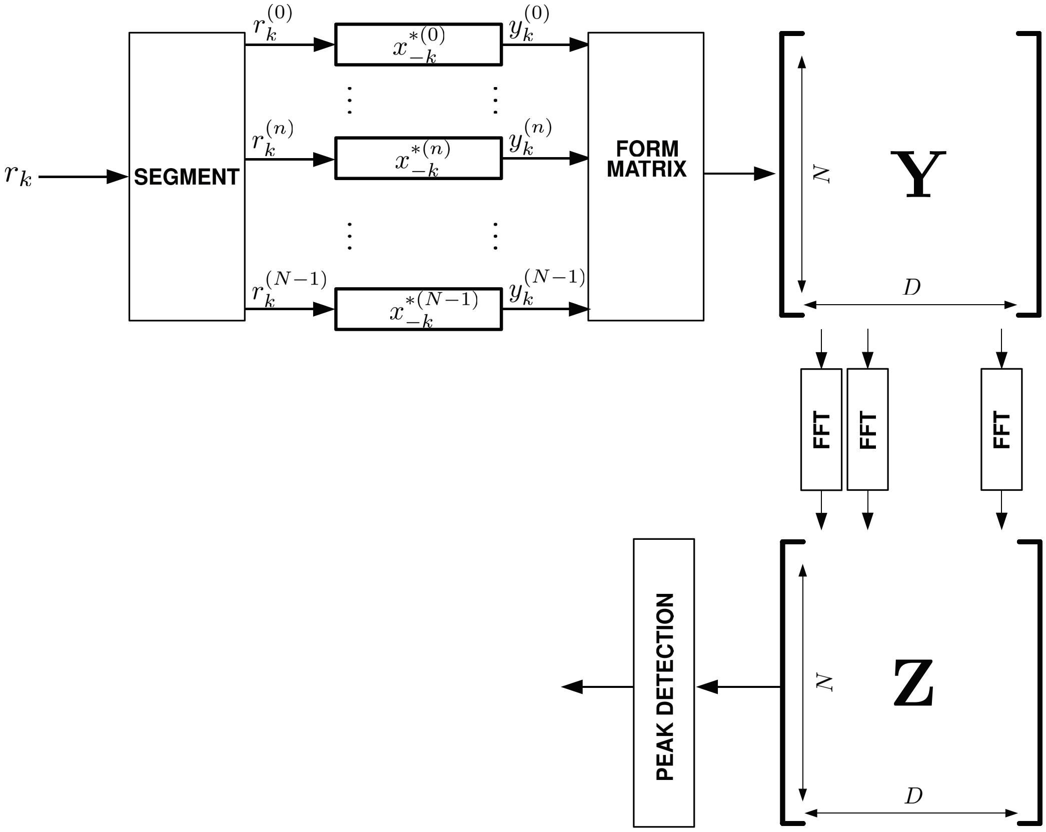

Figure 3.2: Block diagram of the core delay-Doppler efficient exhaustive search (DEES) algorithm.

segments N, and is determined by the signal length L and sampling frequency $f_s = 1/T_c$.

We now discuss how to obtain estimates of d_0 and ω_D. Since DSSS signals have, ideally, thumbtack autocorrelation characteristics, one strategy to produce estimates is to search for distinct peaks in $|\mathbf{Z}|$. The code phase offset and Doppler frequency can be jointly estimated with row index $m \in \mathcal{M}$ and column index $k \in \mathcal{D}$, namely $\hat{\omega}_D = 2\pi m/L$ and $\hat{d}_0 = k$. In the case of a multipath channel and RAKE receiver, this process can be repeated where $\{d_0, \omega_D\}$ is estimated independently for each path. The receiver zeros-out the peak it just estimated in $|\mathbf{Z}|$ before moving onto the next one. In this case, the receiver must have a priori knowledge of the number of channel paths present. For visualization an example is shown in Fig. 3.3 for a two path channel.

Up until this point we have assumed that the channel gain $\alpha = 1$. While a non-unity α does not affect the estimation process for $\{d_0, \omega_D\}$, core DEES can obtain coarse channel gain estimates from $\mathbf{Z}$. We now briefly derive the channel gain estimate $\hat{\alpha}$.

The output of the nth partitioned matched filter is:

$$\begin{aligned}
y_k^{(n)} &= r_k^{(n)} \ * \ x_{-k}^{*(n)} \\
&= r_{nL/N+k} w'_k \ * \ x_{-k}^{*(n)} \\
&\approx \alpha x_{k-d_0}^{(n)} e^{j\omega_D(k+nL/N-d_0)} \ * \ x_{-k}^{*(n)} \\
&= \alpha e^{j\omega_D(nL/N+d_0)} x_{k-d_0}^{(n)} e^{j\omega_D(k-d_0)} \ * \ x_{-k}^{*(n)},
\end{aligned} \tag{3.14}$$

where in the third line it was assumed that due to the favorable autocorrelation characteristics of DSSS signals the contributions of the correlations of segments surrounding the nth segment are negligible.

Substituting (3.14) into (3.13) yields:

$$\begin{aligned}
y_k &= \alpha \sum_{n=0}^{N-1} e^{j(\omega_D - 2\pi m)nL/N} e^{j\omega_D d_0} x_{k-d_0}^{(n)} e^{j\omega_D(k-d_0)} \ * \ x_{-k}^{*(n)} \\
&= \alpha \sum_{n=0}^{N-1} e^{j(\omega_D - 2\pi m)nL/N} e^{j\omega_D d_0} A^{(n,n)}[k - d_0, \omega_D),
\end{aligned} \tag{3.15}$$

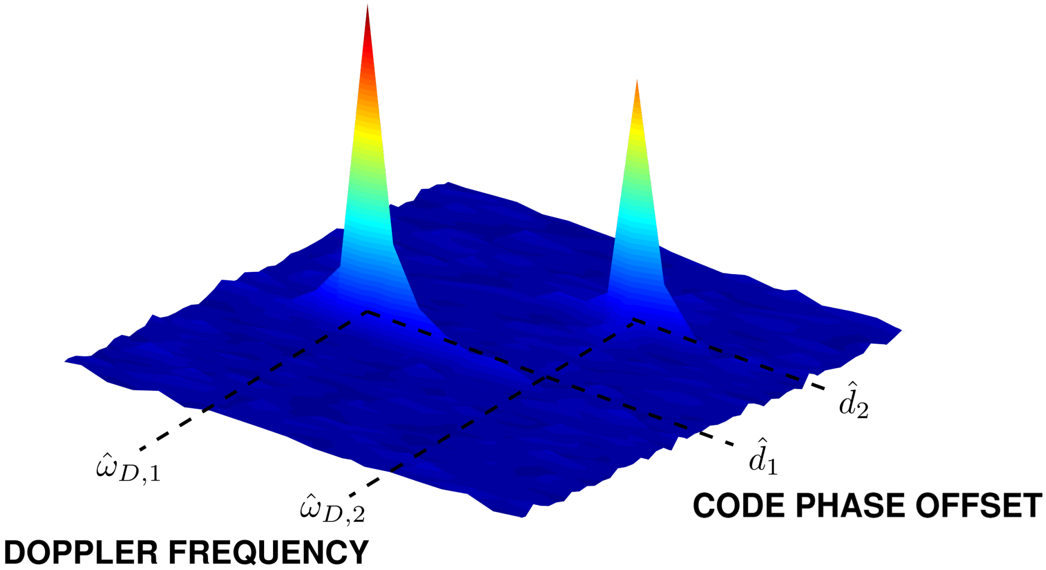

Figure 3.3: Depiction of $|\mathbf{Z}|$ at high SNR for a two path channel. Doppler frequency estimates can be obtained from the row indices, while estimates of the code phase offsets are obtained from column indices. Channel gain estimates for each path can be obtained from the corresponding complex amplitudes in $\mathbf{Z}$.

where $A^{(n,n)}[k, \omega_D) = x_k^{(n)} e^{j\omega_D k} \ast x_{-k}^{*(n)}$ is the discrete ambiguity function[1] of the nth transmitted signal segment.

From (3.15) we can estimate α. Let Z_{mk} denote the entry in $\mathbf{Z}$ where m is the row index and k is the column index of the corresponding peak in $|\mathbf{Z}|$, then:

$$\hat{\alpha} = \frac{Z_{mk}}{\sum_{n=0}^{N-1} e^{j\hat{\omega}_D \hat{d}_0} A^{(n,n)}[0, \hat{\omega}_D)}. \tag{3.16}$$

It should be apparent from (3.16) that both the Doppler estimate and the code phase offset estimate must be obtained prior to $\hat{\alpha}$. Subsequently, the channel gain estimates produced by core DEES are highly dependent on the accuracy of $\{\hat{d}_0, \hat{\omega}_D\}$, and should be viewed as an auxiliary feature with limited accuracy.

It is important to note that the only difference between core DEES and an exhaustive search is the constant phase approximation in (3.10). Thus as long as CPA holds, core DEES will produce the same estimates as an exhaustive search with the same quantization

---

[1] See [141] for more details on ambiguity functions.

constraints.

3.3 Numerical Simulations

To assess the performance of core DEES, we characterize its DSSS acquisition performance in a synthetic channel as a function of SNR and compare it against the exhaustive search. We then assess core DEES's channel estimation performance in a multipath channel.

While the optimal exhaustive search (ES) can be described by (3.3), in practice it is necessary to search over a finite space. Subsequently, we implement (3.3) by means of a 2D grid search in which the received signal r_k is compensated by $e^{-j\omega_n k}$, for candidate Doppler frequencies $\{\omega_0, \omega_1, \ldots\ \omega_{N-1}\}$, then passed through a filter matched to the full length L x_k; this is essentially a discrete time implementation of Fig. 2.8. This search can be used to generate coarse estimates for d_0 and ω_D, but are are limited in precision by both N and the quantization of the code phase search. To alleviate these issues, we utilize these estimates as seeds for a numerical search that can find the local maximum of the objective function in (3.3). Thus our implementation of ES consists of a 2D grid search followed by a numerical local maximization algorithm. In particular, we make use of the interior-point constrained optimization routine within MATLAB.

To compare the acquisition performance between core DEES and the exhaustive search just described, we measured their probability of acquisition P_A for a fixed false alarm rate P_{FA}. P_A and P_{FA} are calculated by the fraction of trials that the decision statistic (3.2) exceeds threshold ζ when the signal component of r_k is present and absent, respectively. We assume that inaccurate estimates of $\{d_0, \omega_D\}$ will result in a negligible correlation.

For each SNR we simulate 10^5 trials, where each trial has both independent noise and parameter realizations. Each parameter is drawn from a uniform distribution ranging from $\pm$ its maximum value; for example d_0 is drawn from $\mathcal{U}(-d_{0,\text{max}}, d_{0,\text{max}})$. The phase of the channel gain α is uniformly distributed, and $|\alpha|$ is drawn from $\mathcal{U}(1, 5)$.

We consider a system with $f_c = 2$ GHz, $f_s = 1/T_c = 1$ MHz, $L = 8200$; this results in a Doppler resolution of $\triangle f = 121.95$ Hz. For the channel parameters we set $d_{0,\text{max}} = 50$ and $\omega_{\text{max}} = 0.0251$ which corresponds to a maximum Doppler shift of 2 kHz. We first consider the case of a channel with a single path.

Our simulation results suggest that in practice, core DEES provides acquisition performance similar to that of the 2D grid search. This is evidenced by the closeness of the blue (core DEES) and light blue (2D grid search) curves in Fig. 3.4(a), which plots P_A vs. SNR (dB) for a fixed $P_{FA} = 10^{-3}$. However, both core DEES and the 2D grid search underperform ES which is neither constrained by a 1-chip quantization error in the code phase offset estimate nor constrained by the Doppler resolution $\triangle f = 1/LT_c$. This is apparent in Fig. 3.4(b) where the mean absolute error for the exhaustive search's code phase estimate $\hat{d}_0$ (green solid curve) does not obtain a lower bound and continues to decrease as the SNR increases. While it does appear the MAE of the Doppler estimate for ES obtains a lower bound, this is an artifact due to the stopping criteria of the numerical solver, and not inherent to the ES itself.

For core DEES and the 2D grid search we can verify that the lower bounds on the MAE for $\hat{d}_0$ and $\hat{f}_D$ are in accordance with theoretical values. We consider the expected value of the MAE of an estimator $\hat{\theta}$ that takes discrete values $\{-\triangle/2, \triangle/2\}$ when the true value θ is uniformly distributed within the bin $\mathcal{U}(-\triangle/2, \triangle/2)$. If $X = |\theta - \hat{\theta}|$, then $\mathbb{E}[X] = \mathbb{E}[X|\hat{\theta} = -\triangle/2]P[\hat{\theta} = -\triangle/2] + \mathbb{E}[X|\hat{\theta} = \triangle/2]P[\hat{\theta} = \triangle/2] = \triangle/4$. For the system of interest $\triangle f = 121.95$ Hz and $\triangle d_0 = 1$ chips, which imply the MAE of the Doppler estimate approaches $\triangle f/4 = 30.48$ Hz and the MAE of the code phase offset estimate approaches $\triangle d_0/4 = 0.25$ at high SNR. Fig. 3.4(b) corroborates both of these claims.

From Fig. 3.4 is it apparent that core DEES achieves similar performance as the 2D grid search, although both of these techniques underperform the exhaustive search. However, these limitations largely due to the quantization error in the code phase offset estimate and the Doppler resolution. The former may be remedied by oversampling at the receiver,

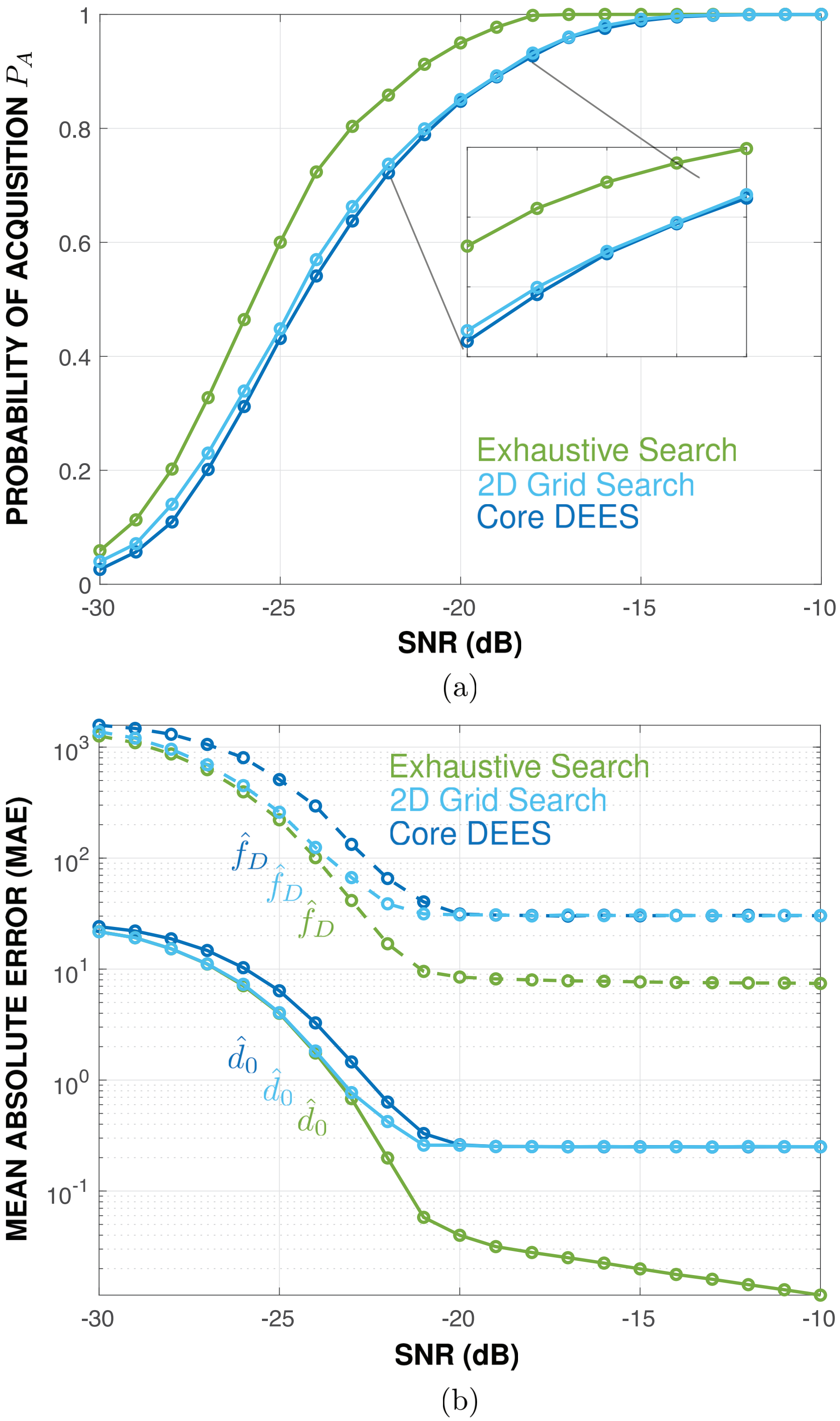

Figure 3.4: (a) Probability of acquisition P_A vs. SNR (dB) for the exhaustive search, 2D grid search, and core DEES with $L/N = 20$, for a fixed $P_{FA} = 10^{-3}$. The inset plot is a magnified section of the same set of curves. (b) Mean absolute error (MAE) for $\hat{d}_0$ (solid lines) and $\hat{f}_D$ (dashed lines) for the same simulation in (a).

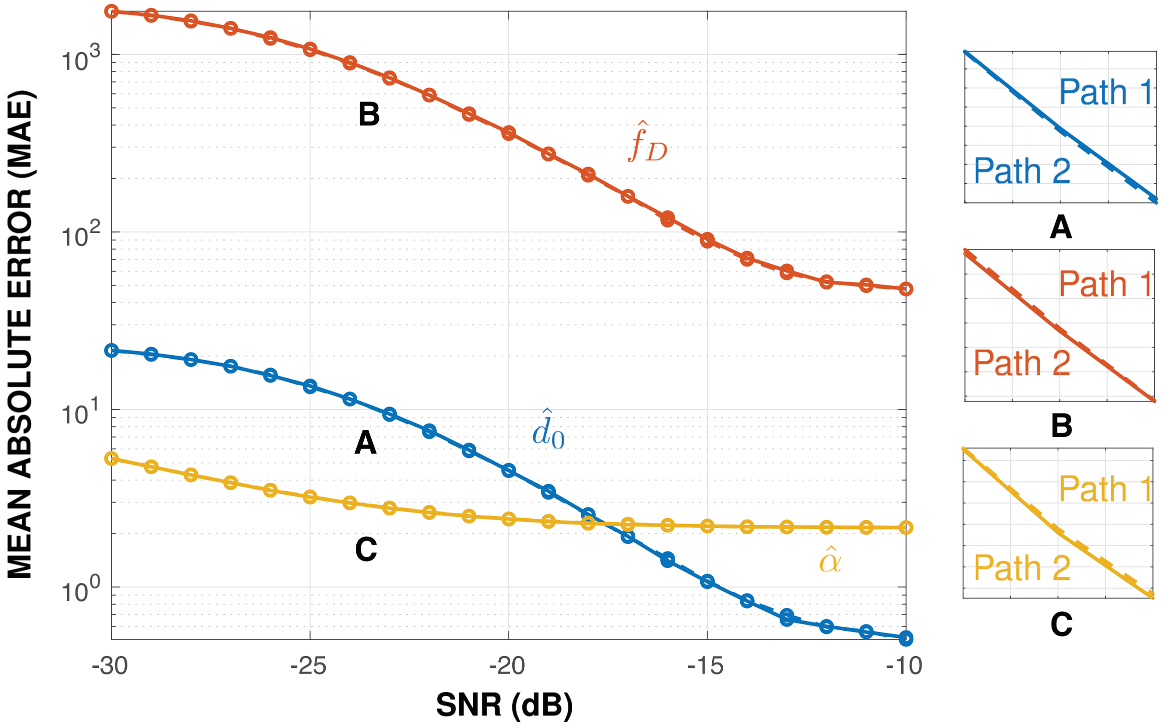

Figure 3.5: Mean absolute error (MAE) for $\hat{d}_0$ (blue curves), $\hat{f}_D$ (red cures) and $\hat{\alpha}$ (gold curves) for core DEES in a two path channel. The subplots on the right of the figure are zoomed-in plots of the same set of curves from $-24 \leq \text{SNR (dB)} \leq -22$. The dashed lines of the same color indicate the MAE for the estimates associated with the second channel path.

giving a sub-chip resolution, and the latter also by increasing the sampling rate or by increasing L if possible.

Finally we shift our attention to the estimation capabilities of core DEES in a multipath environment. We use the same channel parameters as before, however, we now enforce that the delay of the second channel path differs from the delay of the first channel path by at least one chip, e.g. $|d_{0,1} - d_{0,2}| \geq 1$, such that both paths may be clearly resolved.

As can be seen from Fig. 3.5 core DEES is capable of estimating both the code phase offset and the Doppler frequency independently for each of the two channel paths. Since the range of channel parameters are the same for both paths, the MAE curves for the second channel path (dotted lines) overlaps with that of the first (solid curves); this is more easily seen in the subplots on the side. Using (3.16), core DEES can obtain channel estimates for both channel paths. However, not only are these estimates dependent on the accuracy of both $\hat{d}_0$ and $\hat{\omega}_D$, but they are also constrained by the quantization error of both estimates. Subsequently, even as the SNR increases and the accuracy of $\hat{d}_0$ and $\hat{\omega}_D$ improve, the MAE of $\hat{\alpha}$ also achieves a lower bound. These channel estimates may be used to seed the automatic gain control in other systems within the receiver, but are too coarse for diversity combining or other applications requiring a high degree of accuracy.

3.4 Effect of Segment Size on Performance and Complexity

Up until this point we have placed a minimal amount of restrictions on how the number of segments N should be chosen. While the number of segments should be selected such that $N > \omega_{\max} L/\pi + 2$, in practice this still leaves a wide variety of values that N could take. In this section, we discuss the trade-offs associated with N, and show that when N is large the Doppler losses are minimized, but at the cost of higher computational complexity.

There are two main causes for the Doppler losses in core DEES. The first is the Doppler mismatch between the nth segment of the received signal and the nth matched filter, which leads to an amplitude loss as it is equivalent to slicing the ambiguity function $A^{(n,n)}[0, \omega_D)$ away from its maximum value at $A^{(n,n)}[0, 0)$. The second is the frequency response inherent to the core DEES algorithm.

This frequency response can be understood from the amplitude of the peaks in $|\mathbf{Z}|$. We begin the analysis with quantity Z_{mk}, which we first introduced in (3.16):

$$\begin{aligned} Z_{mk} &= \alpha e^{j\omega_D d_0} \sum_{n=0}^{N-1} e^{j(\omega_D - \omega)nL/N} A^{(n,n)}[0, \omega_D) \\ &= \alpha e^{j\omega_D d_0} A_{L/N}[0, \omega_D) \sum_{n=0}^{N-1} e^{j(\omega_D - \omega)nL/N} \\ &= \alpha e^{j\omega_D d_0} A_{L/N}[0, \omega_D) e^{-j(\omega_D - \omega)\frac{N-1}{2}\frac{L}{N}} \frac{\sin((\omega_D - \omega)L/2))}{\sin((\omega_D - \omega)L/2N))}, \end{aligned} \tag{3.17}$$

where the candidate Doppler frequency $\omega = 2\pi m/L$ has been abstracted for visualization purposes, and where in the second line $A^{(n,n)}[0, \omega_D)$ was replaced with $A_{L/N}[0, \omega_D)$, which is the ambiguity function of a length L/N sequence of 1s. This can be done since only at the 0 time lag does $A^{(n,n)}[0, \omega_D) = A_{L/N}[0, \omega_D)\ \forall n$.

We can then define the normalized peak amplitude β as the amplitude of Z_{mk} divided by the peak amplitude when $\omega_D = 0$. Namely:

$$\beta = \left| \frac{A_{L/N}[0, \omega_D)}{L} \frac{\sin((\omega_D - \omega)L/2)}{\sin((\omega_D - \omega)L/2N)} \right|. \tag{3.18}$$

It should be apparent from (3.18) that the Doppler mismatch during the partitioned matched filtering results in an amplitude reduction, as evidenced by the $A_{L/N}[0, \omega_D)$ term, while the Doppler compensation by FFT has a frequency dependent response, as evidenced by the $\sin((\omega_D - \omega)L/2)/\sin((\omega_D - \omega)L/2N)$ term. This term gives rise to scalloping loss, in which the amplitude of the peaks in $|\mathbf{Z}|$ is reduced if the Doppler frequency falls between two FFT bins [83, 141].

β achieves a maximum value of unity only when $\omega_D = 0$; this holds even when $\omega = \omega_D$, as the loss due to the $A_{L/N}[0, \omega_D)$ term is irreversible. However, as a whole the Doppler loss can be reduced by reducing L/N. This is seen in Fig. 3.6 which plots β vs. Doppler frequency (Hz) for $L/N = \{10, 20, 50, 100, 205\}$ for simulated data (solid curves) and analytical expressions (3.18) (dashed curves). When the channel Doppler frequency f_D is low, the choice of L/N does not have a noticeable affect on β as evidenced by the overlap of all the curves in the left-half of the figure. However, as the Doppler frequency increases, it is apparent that a larger segment size results in a decrease in β. At $f_D = 2$ kHz $\beta \approx 0.75$ when $L/N = 205$, compared to $\beta \approx 0.99$ when $L/N = 20$.

Based on the results in Fig. 3.6, it would appear when utilized core DEES a smaller segment size should be used to curb Doppler losses. Selecting a smaller segment size results in a larger N, which ultimately will increase the computational complexity of core

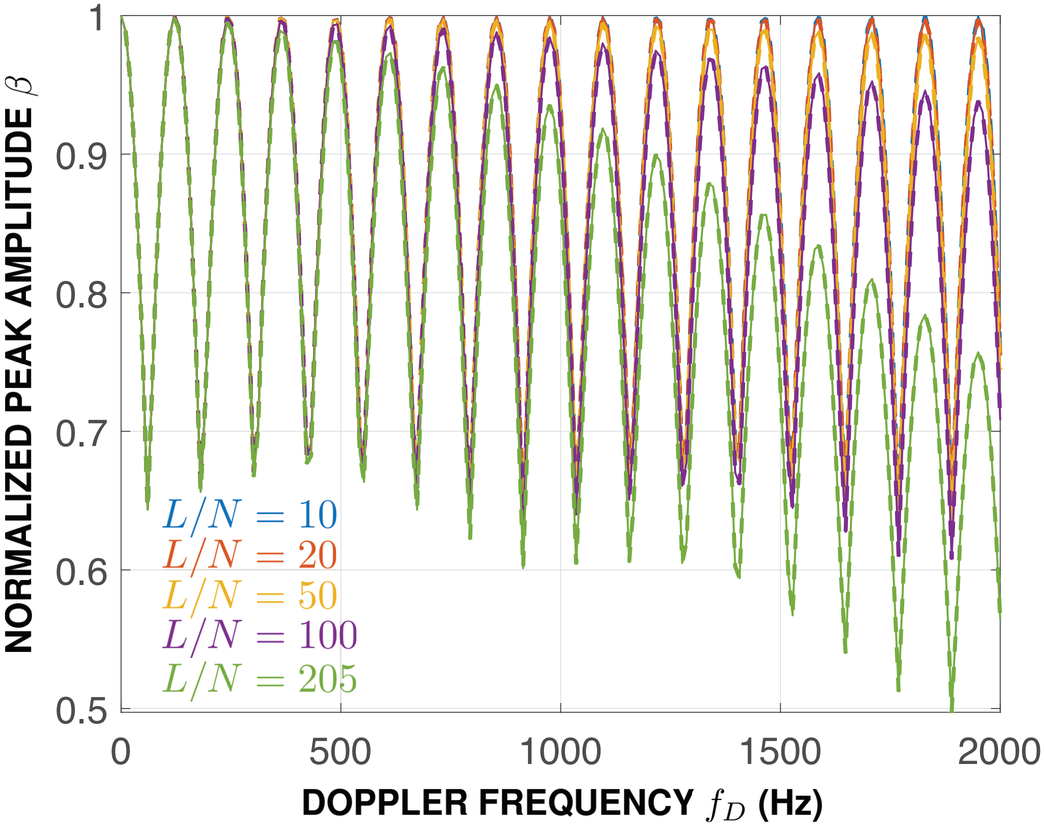

Figure 3.6: Doppler loss β vs. Doppler frequency (Hz) for core DEES for a family of segment sizes L/N. Solid curves indicate simulation results, while dotted curves indicate analytical expressions.

DEES. Thus there exists a trade off between robustness to high Doppler frequencies, and computational complexity.

We now characterize the complexity of core DEES and compare it to the complexity of the exhaustive search, whose implementation was described in the previous section. We will show that core DEES always has lower computational complexity than the exhaustive search for an equivalent number of candidate Doppler frequencies, due to the computational efficiency afforded by the FFT.

We define complexity as the number of computations required to obtain estimates of $\{d_0, \omega_D\}$. We consider each complex add or complex multiply as one operation, and assume that memory loads and register shifts have negligible computational cost. For example, the computation of $(a + b)$ is considered to be one operation. Vectorization of matrices is assumed to be computationally negligible as well.

Using this methodology we can compute the complexity of the exhaustive search. Assuming the received signal r_k is of length $(L + D)$, for a given candidate Doppler ES requires $(L + D)$ multiplications to compensate the r_k by $e^{-j\omega_n k}$ and $(L + D)(2L - 1)$ operations to search over all possible code phase offsets with a MF implementation. For N candidate Doppler frequencies, this results in a total computational complexity of $\mathcal{O}(2NL(L + D) + \psi)$ where ψ is the complexity associated with the local maxima search, and is implementation dependent.

There are several methods for implementing the DFT core DEES requires. One way is to utilize an N-point FFT as shown in Fig. 3.2 which we assume has computational complexity order $\mathcal{O}(N \log_2 N)$ [140]. The complexity cost associated with the partitioned matched filtering is $\mathcal{O}(\mathcal{D}(2L - N))$, while the computational cost associated with the FFT of the columns of $\mathbf{Y}$ is $\mathcal{O}(\mathcal{D}N\log_2(N))$. Thus the complexity of core DEES is $\mathcal{O}(D(2L + N[\log_2(N) - 1]))$.

An interesting case arises when the number of partitions N is selected such that $\omega_{\text{DFT}} = \pi N/L < \omega_{\max}$, which implies that there are more candidate Doppler frequencies that are

Table 3.1: Summary of Algorithm Complexities

DETECTOR	COMPLEXITY ORDER
Exhaustive Search	$\mathcal{O}(2NL(L+D)+\psi)$
core DEES FFT	$\mathcal{O}(D(2L+N[\log_2(N)-1]))$
core DEES Pruned FFT	$\mathcal{O}(D(2L+N[\log_2(K)-1]))$

searched over than are actually required; in this case, not every output of the FFT needs to be computed. The computational complexity of a pruned FFT, in which only K of the N outputs are required is assumed to be $\mathcal{O}(N\log_2 K)$. When considering pruned FFTs, the complexity of core DEES reduces to $\mathcal{O}(D(2L+N[\log_2(K)-1]))$ where $\omega_{\text{max}}L/\pi+2\leq K<N$.

The computational complexity of core DEES scales as $\mathcal{O}(N[\log_2(N)-1])$ with respect to the number of segments. Given the previous discussion on amplitude degradation in $|\mathbf{Z}|$ due to Doppler mismatch, the segment size L/N should be selected to keep Doppler mismatch to a tolerable level, but not so small such that N is large and the computational complexity is high. Even when incorporating FFT pruning, a large number of segments will still incur a high complexity as pruning only affects the $\log_2(K)$ term, and not the linear N dependency.

The computational complexities of both ES and core DEES are summarized in Table 3.1. It is apparent that even when $\psi=0$, which corresponds to the 2D grid search, the computational complexity of ES is strictly greater than that of core DEES, whose complexity is greatly reduced due to the partitioned matched filtering and the FFT.

3.5 Summary

In this chapter we have introduced core DEES, an efficient algorithm derived from the optimal exhaustive search that can acquire DSSS signals with static code phase offsets and constant Doppler frequencies. It achieves similar acquisition performance when compared to the 2D grid search, and mildly underperforms the exhaustive search chiefly due to quantization limitations. core DEES provides auxiliary channel estimation capabilities, and can take advantage of a multipath channel environment if the number of channel paths is known. Its greatest drawback is its inability to deal with time-varying channel code phase offsets which are present when Doppler frequencies are large and when the spreading code is long. These limitations will be addressed in the next chapter.

CHAPTER 4

DSSS ACQUISITION FOR TIME-VARYING CODE PHASE OFFSETS

In this previous chapter, we proposed core DEES, an efficient algorithm that can acquire direct-sequence spread-spectrum signals when the Doppler frequency is constant, and the code phase offset is static. However, when the Doppler frequency is large, the Doppler rate is high, or when the frame is long, the time-varying effects of the channel can no longer be ignored, and the code phase offset can no longer be modeled as static. A communication environment characterized by these channel impediments is sometimes referred to as a high-dynamic environment [23, 94, 95].

Rather than develop a brand new acquisition algorithm from scratch, we propose several augmentations to the core DEES algorithm that will allow it to handle both time-varying code phase offsets and a time-varying Doppler frequency [142]. We begin with an adjustment to the received signal model described in (3.1) to better model the channel effects present in a high-dynamic communication environment. We then showcase the efficacy of the proposed augmentations, and then finally we compare the acquisition performance of DEES, the augmented version, and core DEES in the LEO satellite channel. This chapter assumes the reader is familiar with the mechanics of core DEES's operation, along with the associated notation.

4.1 Received Signal Model

Given the vast existing literature on DSSS acquisition for static code phase offsets and constant Doppler [28, 76, 83, 84, 86, 87, 91, 143], we specifically focus on the time-varying Doppler aspect of the problem, and ignore non-essential features such as data modulation which have been discussed in [76]. As in Chapter 3, we focus our efforts on the estimation portion of acquisition, and leave the detection stage untouched.

The baseband IQ samples at the receiver are modeled as:

$$r_k = \alpha x_{k-d_k} e^{-j\omega_0 d_k} + n_k, \tag{4.1}$$

where α is an unknown complex channel gain, $\omega_0 = 2\pi f_c T_c$ is the normalized radian carrier frequency, f_c is the carrier frequency in Hz, T_c is the chip period, $f_s = 1/T_c$ is the sampling frequency, and the components of the noise vector n_k are *i.i.d.* $\mathcal{CN}(0, 2\sigma^2)$. The transmitted binary DSSS signal x_k is assumed to be known to the receiver, and is non-zero only for $k \in \{0, 1, \ldots, L-1\}$. To account for the case when d_k in (4.1) is not an integer, we define $x_{k-d} = \sum_n x_n \text{sinc}((k-n)-d)$; for readability this interpolating sinc is suppressed.

To reflect the presence of both Doppler rate and Doppler frequency shift, we adopt a quadratic model for the code phase offset d_k, namely:

$$d_k = d_0 - b_0 k - b_1 k^2, \tag{4.2}$$

where d_0 is the initial code phase offset in chips, $b_0 = f_{D,0}/f_c$ is a constant proportional to the initial Doppler frequency $f_{D,0}$ in Hz, and $b_1 = f_A T_c/(2f_c)$ is a constant proportional to the Doppler rate f_A in Hz/s, which is assumed to be constant.

The receiver is assumed to have knowledge of the maximum values of the coefficients in (4.2), i.e. $|d_0| \leq |d_{0,\text{max}}|$, $|b_0| \leq |b_{0,\text{max}}|$, and $|b_1| \leq |b_{1,\text{max}}|$. Furthermore, implicit in (4.1) is the assumption that the maximum possible Doppler frequency shift is just a small fraction of the chip rate, that is $|b_{0,\text{max}} + Lb_{1,\text{max}}/2| f_c T_c << 1$. Subsequently, the receiver has knowledge of the maximum code phase offset d_{max}, and the maximum normalized radian Doppler frequency shift ω_{max}.

The received signal model in the previous chapter (3.1) can be viewed as a special case of (4.1), in which the Doppler rate is zero ($b_1 = 0$), the constant phase shift due to d_0 $e^{-j\omega_0 d_0}$ is ignored, and $|b_0 L| << 1/2$ such that the code phase offset can be approximated as static $d_k \approx d_0$.

This chapter solves the following problem: given knowledge of the received signal model in (4.1) and the quadratic model in (4.2), estimate the parameters $\{d_0, b_0, b_1\}$ that maximize the acquisition statistic [68, 144]:

$$z = \left| \sum_{k=-\infty}^{\infty} r_k x^*_{k-\hat{d}_k} e^{+j\omega_0 \hat{d}_k} \right|^2, \tag{4.3}$$

where $\hat{d}_k$ is the estimate of d_k.

4.2 Time-Varying Code Phase Offsets

Core DEES, or any partial-correlation-FFT based DSSS acquisition technique, will experience two main problems when utilized in a high-dynamic environment [145]. The first is known as code phase migration (CPM), which arises from the fact the time-varying channel delay will cause the code phase offset to shift over time as core DEES performs its partitioned matched filtering. The second is known as Doppler frequency migration (DFM), and arises from the fact the channel Doppler frequency is time-varying. The combination of both of these effects will prevent coherent integration from the FFT of the columns of $\mathbf{Y}$, resulting in indistinct peaks in $|\mathbf{Z}|$, which greatly reduces core DEES's acquisition performance.

An example of this can be seen in Fig. 4.1(a), where the left-half of the figure depicts $|\mathbf{Y}|$ in the segment-code phase plane, where CPM for a two path channel is present. Since the FFT applied to $\mathbf{Y}$ can only capture signal energy in a given column, the post-integration SNR is significantly reduced. The right-half of Fig. 4.1(a) depicts $|\mathbf{Z}|$ in the code phase-Doppler plane, after the FFT of the columns of $\mathbf{Y}$. The two jagged lines indicate DFM is present for both channel paths.

Instead of deriving a new algorithm from the 3D exhaustive search over $\{d_0, b_0, b_1\}$ in a similar fashion to how core DEES was derived from the 2D exhaustive search in (3.4), our approach is to utilize several signal processing techniques to eliminate the time-varying effects of the channel, and then use core DEES to acquire the static signal. This will adjust the problem from an expensive 3D search to a 2D one with some additional post-processing, where in Chapter 3 we have established core DEES provides performance comparable to the 2D exhaustive search.

Our approach is to utilize a second-order keystone transform (SOKT)[146, 102] to mitigate the quadratic component of CPM, then use a fractional Fourier transform (FrFT) to estimate the Doppler rate, compensate for it with a complex phase factor, and finally apply another SOKT to remove any residual CPM and DFM. We first discuss each step in the ideal case in which digitization is a non-issue, then discuss a practical implementation of this approach.

Ignoring the noise component, the output of the nth MF is:

$$\begin{aligned} y_k^{(n)} &= r_k^{(n)} \, * \, x_{-k}^{*(n)} \\ &\approx \alpha x_{k-d_{nL/N}}^{(n)} e^{-j\omega_0 d_{nL/N}} \, * \, x_{-k}^{*(n)}, \end{aligned} \tag{4.4}$$

where in the last line it was assumed that since CPA holds the delays within a given signal segment will not change, i.e. $d_{k+nL/N} \approx d_{nL/N}$.

Taking the DTFT of (4.4) with respect to k and expanding $d_{nL/N}$ yields:

$$Y(n,\omega') = \alpha X(n,\omega') X^*(n,\omega') e^{-j(\omega_0+\omega')d_0} e^{j(\omega_0+\omega')(b_0 nL/N + b_1 (nL/N)^2)}, \tag{4.5}$$

where ω' is the discrete-time radian Fourier frequency and $X(n,\omega')$ is the DTFT of $x_k^{(n)}$. The exp$(j\omega' b_0 nL/N)$ term in (4.5) is responsible for the linear component of CPM, while the exp$(j\omega' b_1 (nL/N)^2)$ term is responsible for both the quadratic component of CPM and DFM.

First proposed in the context of synthetic aperture radar, the keystone transform (KT) is able to correct for linear time-varying delays without a priori knowledge of the target's velocity [147]. The KT has since been extended to a "second-order" form which can blindly correct for quadratic time-varying delays. The SOKT is [102, 146]:

$$n = \sqrt{\frac{\omega_0}{\omega_0 + \omega'}} n' \tag{4.6}$$

where n' is the transformed index. The "second-order" arises from the fact the scaling term $\omega_0/(\omega_0 + \omega')$ is raised to the $1/2$th power; the first-order keystone transform (FOKT) lacks such a factor.

Substituting (4.6) into (4.5) yields:

$$Y(n', \omega') = \alpha X(n', \omega') X^*(n', \omega') e^{-j(\omega_0+\omega')d_0} e^{jb_0 n' L/N \sqrt{\omega_0(\omega_0+\omega')}} e^{j\omega_0 b_1 (n' L/N)^2}, \tag{4.7}$$

where $X(n', \omega')$ is $X(n, \omega')$ after applying the SOKT. The exp$(jb_0 n' L/N \sqrt{\omega_0(\omega_0 + \omega')})$ term in (4.7) indicates that CPM and DFM still remain, as can be seen in Fig. 4.1(b). However, this component cannot be rectified with another keystone transform due to the presence of the exp$(j\omega_0 b_1 (n' L/N)^2)$ term. Our strategy is to utilize the FrFT to estimate the Doppler rate and then multiply (4.7) by exp$(-j\omega_0 \hat{b}_1 (n' L/N)^2)$ to remove the nuisance term, and apply another SOKT to remove any residual CPM.

We now briefly introduce the fractional Fourier transform, then show how the FrFT can be applied to estimate b_1. The FrFT is a generalization of the canonical Fourier transform, and is characterized by a single parameter β. The continuous time FrFT of signal $x(t)$ is [148, 149, 150, 151]:

$$X(\beta, u) = \int_{-\infty}^{\infty} x(t) K_\beta(t, u) dt, \tag{4.8}$$

where the parameter β can be interpreted as a rotation angle, and $K_\beta(t, u)$ is:

$$K_\beta(t, u) = \begin{cases} \sqrt{1 - j\cot(\beta)} e^{j\pi\phi(t,u,\beta)} & \beta \neq n \\ \delta(t - u) & \beta \in 2n\pi \\ \delta(t + u) & \beta \in (2n \pm 1)\pi \end{cases}, \tag{4.9}$$

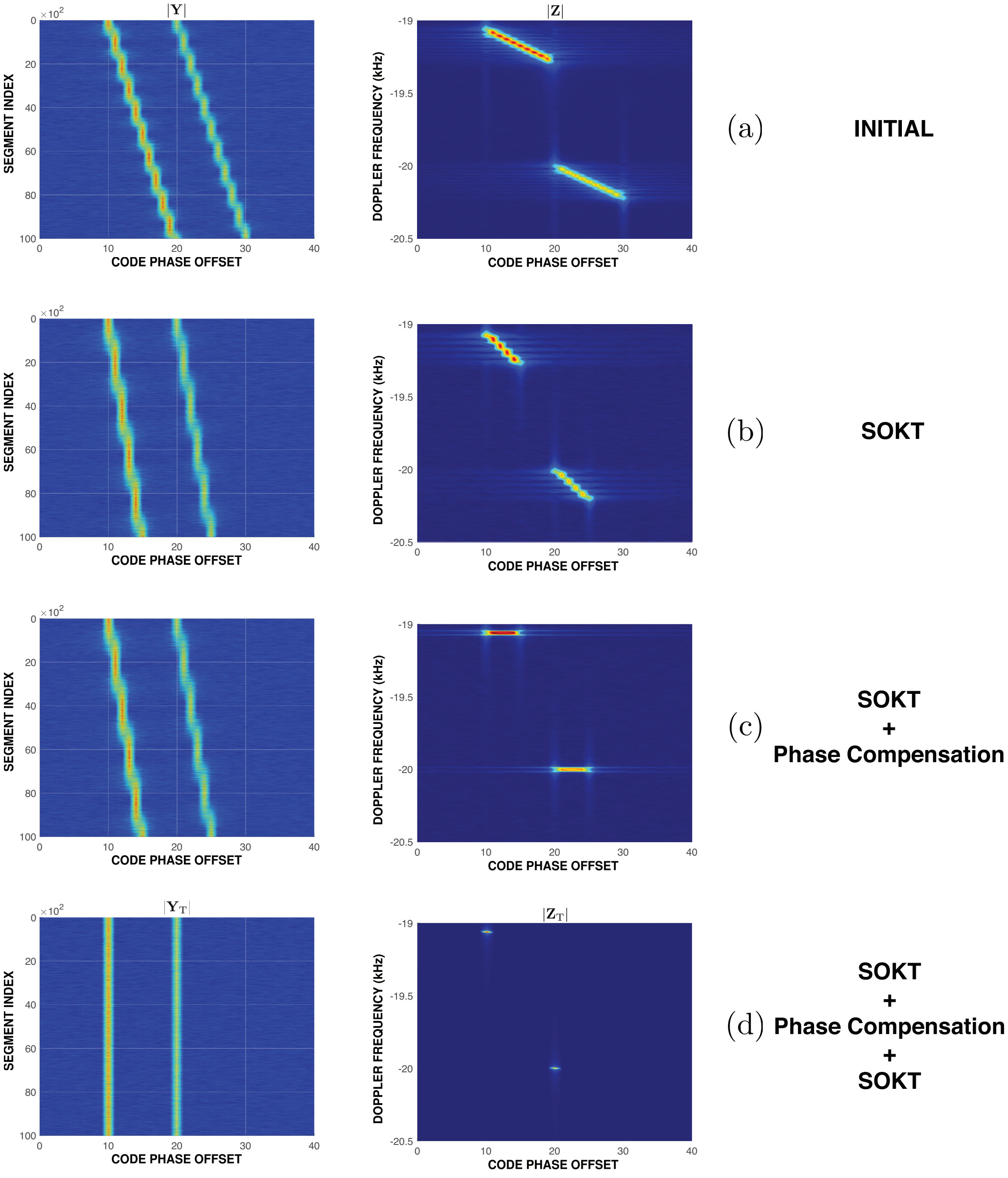

Figure 4.1: Visualization of matrices $|\mathbf{Y}|$ and $|\mathbf{Z}|$ with no transforms applied (a), a second-order keystone-transform (SOKT) applied (b), an SOKT and phase compensation applied (c), an SOKT, phase compensation, followed by another SOKT applied (d). Two path channel with $d_0 = \{10, 20\}$, $f_{D,0} = \{-19.1, -20.0\}$ kHz, and $f_A = \{-1.3, -1.3\}$ kHz/s. SNR $= -10$ dB, $L/N = 1000$.

where $\phi(t, u, \beta) = t^2\text{cot}(\beta) + u^2\text{cot}(\beta) - tu\ \text{csc}(\beta)$, and $n \in \mathbb{Z}$. The FrFT is equivalent to the canonical Fourier transform when $\beta = \pi/2$, is the inverse Fourier transform when $\beta = -\pi/2$, and $\beta = 0$ corresponds to the identity operator [149, 150, 151]. Additional properties of the FrFT, along with the FrFT of several common signals can be found in [148].

Perhaps one of the most intuitive ways to view the FrFT is in the time-frequency plane. The FrFT is then a transform operator which rotates these axes counter-clockwise by angle β [150, 152]; a visualization of this can be seen in Fig. 4.2(a). From this representation, it should be clear that the FrFT is 2π periodic with respect to its transformation angle β. However, for angles in which β is not a multiple of $\pi/2$, the FrFT of the signal is not immediately obvious, and it may be more instructive to view the FrFT as the decomposition of the signal in terms of chirps [150].

The FrFT can be used to estimate the chirp rate of an LFM signal [101, 96, 149, 152]. If $x(t)$ is an LFM signal of the form $Ae^{j\pi(\mu t^2+2f_0t+\phi_0)}$, then an estimate of its chirp rate $\hat{\mu}$ can be obtained from [101]:

$$\hat{\mu} = -\text{cot}(\hat{\beta}), \tag{4.10}$$

where

$$\hat{\beta} = \arg\max_{\beta} |X(\beta, u)|^2. \tag{4.11}$$

The chirp-rate estimation capabilities of the FrFT can be better understood from the time-frequency plane described earlier. An LFM chirp has the distribution of a slant edge or line in the time-frequency plane, since as the name suggests the frequency increases linearly with time [149, 152]. Since the FrFT is an energy preserving transform, sweeping the angle of the FrFT will rotate this slant edge and adjust how concentrated the energy is in the magnitude spectra of the transformed signal. At the optimal angle, the magnitude of the FrFT of an LFM chirp has a distinct peak, as seen in Fig. 4.2(b). Subsequently, (4.11) is a formalization of this process, which can be completed with a brute-force search over all possible β, or with a more efficient algorithm such as the golden section search algorithm as proposed in [149].

If its amplitude were constant, (4.7) can be approximated as an LFM signal with respect to n' with equivalent chirp rate $2b_1 f_c$. Since the channel gain α is already assumed to be a constant, the only remaining term that must be constant is $X(n', \omega')X^*(n', \omega')$. That term corresponds to the Fourier transform of the autocorrelation of a DSSS signal of length L/N, which is ideally a constant. Thus we may approximate $X(n', \omega')X^*(n', \omega')$ as having constant amplitude when the segment size L/N is sufficiently large. The Doppler rate, proportional to b_1, can then be estimated in a similar fashion as (4.10). The post-SOKT and phase compensation can be visualized in Fig. 4.1(c).

If the estimates are accurate enough such that $\hat{b}_1 \approx b_1$, then multiplying (4.7) by $\exp(-j\omega_0 \hat{b}_1 (n'L/N)^2)$ and taking another SOKT yields:

$$Y(n'', \omega') = \alpha X(n'', \omega')X^*(n'', \omega')e^{-j(\omega_0+\omega')d_0}e^{j\omega_0 b_0 n'' L/N}, \tag{4.12}$$

where n'' is the post-SOKT index. From (4.12) it is apparent that there is no longer any coupling between ω' and $\{b_0, b_1\}$, which indicates that the effects of both CPM and DFM have been removed. This can be seen in Fig. 4.1(d), where the energy in $|\mathbf{Z}_\mathrm{T}|$ has been focused into two distinct peaks. The SOKTs and phase compensation via FrFT remove the time-varying aspect of both the code phase and the Doppler shift, and fixes them at an arbitrary point; we chose the initial code phase offset and initial Doppler to allow for easy estimation of $\{d_0, b_0\}$.

We now discuss a practical implementation of these core DEES augmentations. Since it is not feasible to take the DTFT on the output of the N matched filters to produce (4.5), an FFT of the rows of $N \times D$ matrix $\mathbf{Y}$ are instead taken to produce matrix $\mathbf{\Gamma}$. The next step is to apply the second-order keystone transform to each of the columns of $\mathbf{\Gamma}$. Since the variable n cannot simply be substituted as (4.6) suggests, the SOKT must be implemented

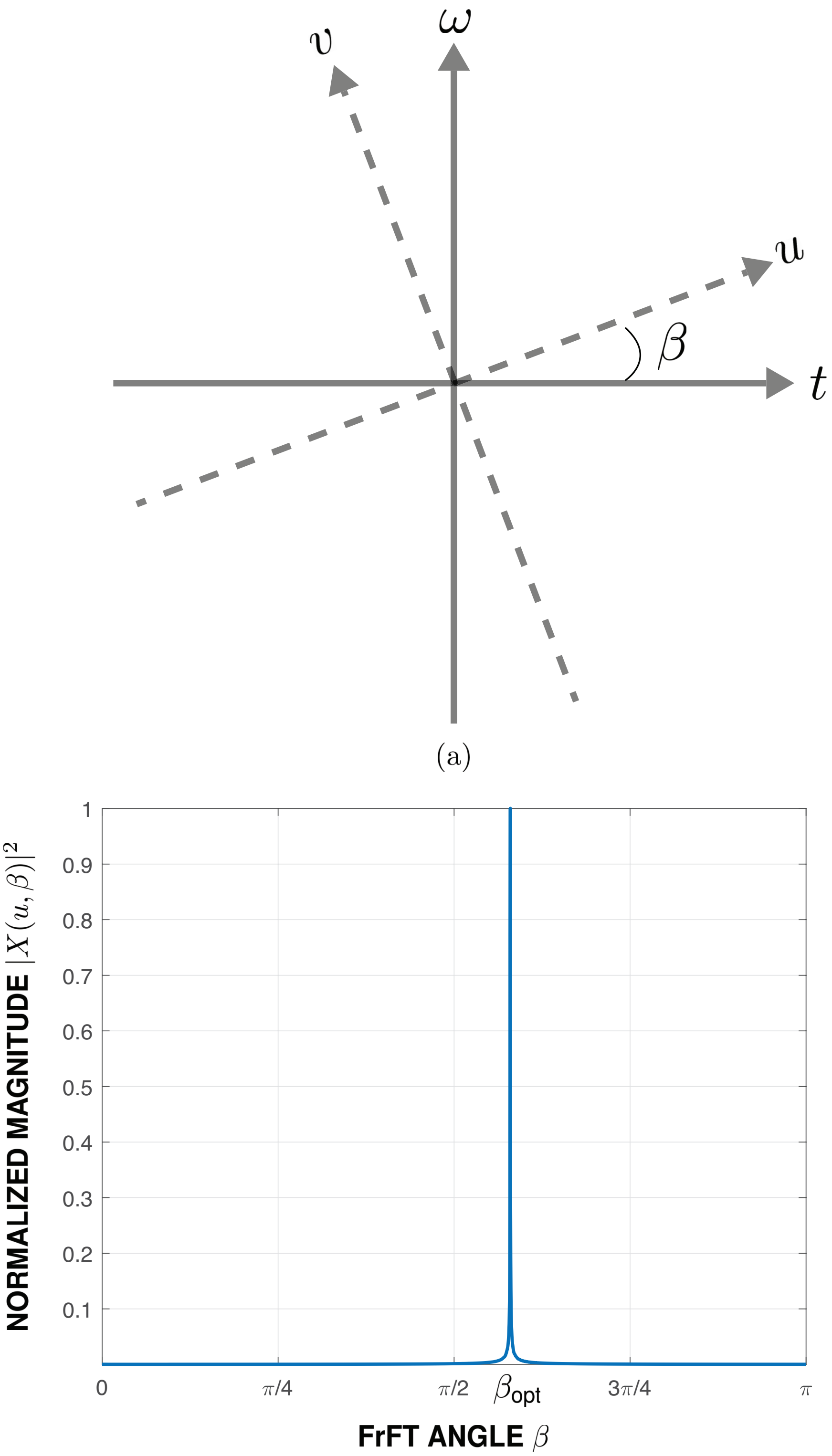

(a)

(b)

Figure 4.2: (a) Illustration of the fractional Fourier transform in the time-frequency plane. The FrFT can be interpreted as a rotational transformation of this plane. (b) Fractional Fourier transform of an LFM chirp signal as a function of FrFT angle β. At the optimal angle, the magnitude of the transform is characterized by a distinct peak.

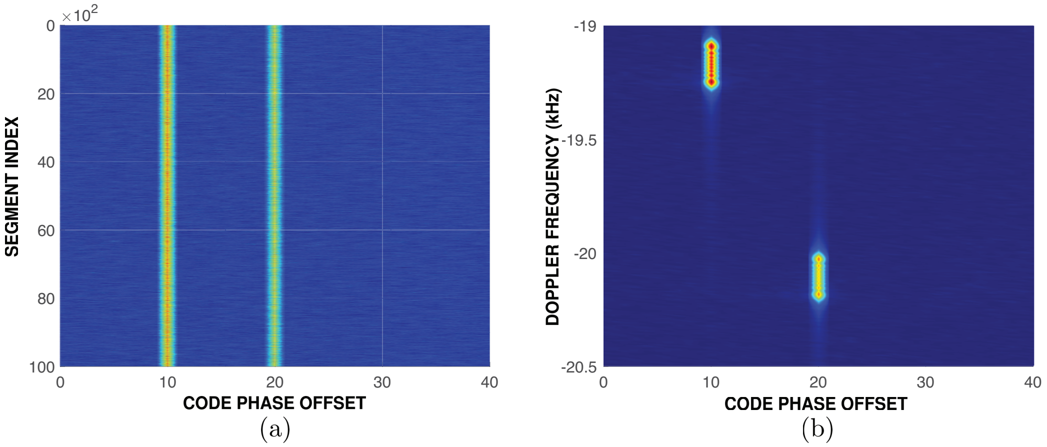

Figure 4.3: Matrices $|\mathbf{Y}|$ (a) and $|\mathbf{Z}|$ (b) after the application of two second-order keystone transforms. Since the exponential phase compensation by the fractional Fourier transform is absent, Doppler frequency migration is still present.

with an interpolation technique, such as sinc interpolation [113]:

$$\Gamma'_{n',l} = \sum_{n=0}^{N-1} \Gamma_{nl} \mathrm{sinc}\left[\sqrt{\frac{\omega_0}{\omega_0 + \frac{2\pi l}{D}}} n' - n\right], \tag{4.13}$$

to produce matrix $\mathbf{\Gamma}'$, where Γ_{nl} refer to the nth row and lth column of $\mathbf{\Gamma}$.

A discrete FrFT is then applied to each of the columns of $\mathbf{\Gamma}'$, to obtain estimates of the equivalent chirp rates $\hat{\eta}_l = -\cot(\hat{\beta}_l)N/(T_cL)^2$, where $\hat{\beta}_l$ is the optimal FrFT angle of the lth column and $N/(T_cL)^2$ is a sampling correction factor for the discrete FrFT [153]. In principle, $\hat{\eta}_l = \hat{\eta} = 2b_1f_c/T_c \; \forall l$. However, in practice this is not the case as the signal has been corrupted by noise and the $X(n',\omega')X^*(n',\omega')$ term in (4.7) is only approximately constant. To improve the accuracy of b_1, it is advantageous to average each of the individual estimates:

$$\hat{b}_1 = \frac{T_c}{2f_c}\frac{1}{D}\sum_{l=0}^{D-1}\hat{\eta}_l. \tag{4.14}$$

At low SNR the accuracy of $\hat{b}_1$ can further be improved by removing extraneous values of $\hat{\eta}_l$, corresponding to $\hat{b}_1$ exceeding $b_{1,\max}$, before taking the mean.

The columns of $\mathbf{\Gamma}'$ are then multiplied by complex phase factor $\exp(-j\hat{b}_1\pi(n'T_cL/N)^2)$, resulting in matrix $\mathbf{\Gamma}''$. An SOKT is applied to the columns of $\mathbf{\Gamma}''$ in a similar fashion as

(4.13), and finally an IFFT is applied to the rows of the resulting matrix to obtain $N \times D$ matrix $\mathbf{Y}_{\mathrm{T}}$. A block diagram of the augmented DEES is shown in Fig. 4.4, where an FFT of the columns of $\mathbf{Y}_{\mathrm{T}}$ is taken in accordance with the core DEES algorithm. In effect, the DEES algorithm is the same as the core DEES algorithm, except matrix $\mathbf{Y}$ has been post-processed to produce matrix $\mathbf{Y}_{\mathrm{T}}$.

We now briefly discuss the DEES's viability in a multipath channel environment. As was discussed in the previous chapter, and as Fig. 3.3 illustrated, core DEES can acquire a DSSS signal in a multipath environment so long as the number of the channel paths is known to the receiver. For the implementation shown in Fig. 4.4, DEES is usable in a multipath environment so long as all the channel paths have the *same* Doppler rate. This limitation is due to the phase compensation $\exp(-j\hat{b}_1\pi(n'T_cL/N)^2)$ applied to matrix $\mathbf{\Gamma}'$ which implicitly assumes there is only one Doppler rate.

As presented, the efficacy of the DEES algorithm is predicated on the accuracy of the Doppler rate estimate $\hat{b}_1$ in (4.14); we had previously assumed that they are sufficiently accurate such that $\hat{b}_1 \approx b_1$ such that (4.12) holds. We now consider the case in which this condition does not hold. Since the estimation error of $\hat{b}_1$ will depend on the channel, we consider the case in which DEES does not make use of the FrFT to obtain Doppler rate estimates (e.g. $\hat{b}_1 = 0$), and instead applies two SOKTs successively.

Applying another SOKT to (4.7) results in

$$Y(n'', \omega') = \alpha X(n'', \omega') X^*(n'', \omega') e^{-j(\omega_0+\omega')d_0} e^{j\omega_0 b_0 n'' L/N} e^{j\frac{\omega_0^2}{\omega_0+\omega'} b_1 (n'' L/N)^2}. \tag{4.15}$$

From 4.15 it is apparent that while the linear component of CPM has been removed, as there is no coupling between b_0 and ω' in the exponent, both CPM and DFM are still present as evidenced by the $\exp(j\frac{\omega_0^2}{\omega_0+\omega'} b_1 (n'' L/N)^2)$ term.

However, in practice the double SOKT can still mitigate some of the time-varying effects of the channel if the CPM contributions from the b_1 component of d_k are

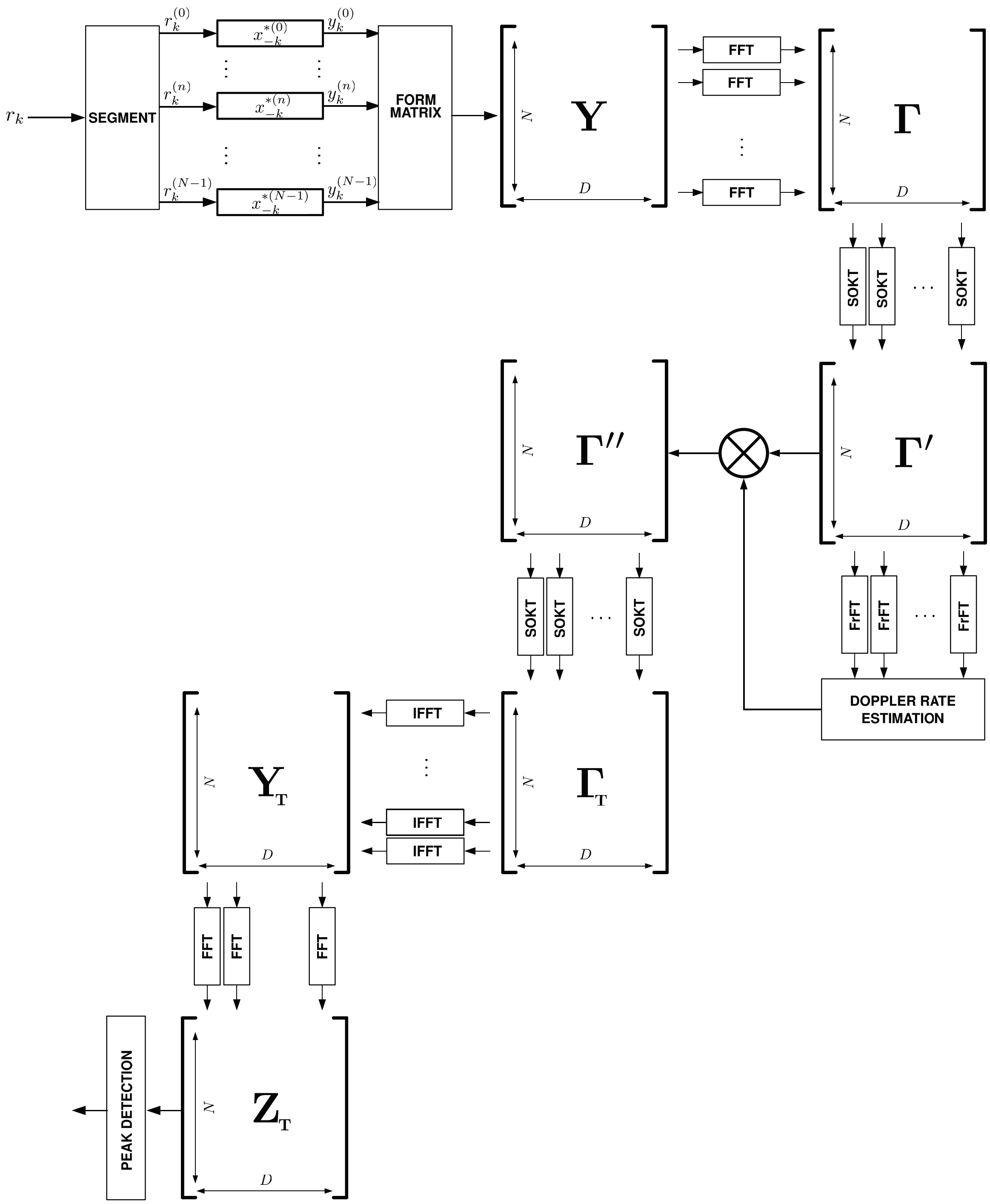

Figure 4.4: Block diagram of the delay-Doppler efficient exhaustive search (DEES) algorithm.

small. This is evidenced in Fig. 4.3 where the residual component of CPM due to the exp$(j\frac{\omega_0^2}{\omega_0+\omega'}b_1(n''L/N)^2)$ term is small and less than one code phase offset bin. Although DFM is still present as seen in Fig. 4.3(b), the energy is still contained in the correct initial code phase offset bins, which will result in an accurate estimate of $\hat{d}_0$, however, the same cannot be said of $\hat{b}_0$.

4.3 Special Case: Zero Doppler Rate

In light of both (3.1) and (4.1), we have not considered the case in which the Doppler rate is zero, and thus $d_k = d_0 - b_0k$ follows a linear model instead of a quadratic one. This corresponds to the case in which the Doppler frequency is constant, but still sufficiently large (or the spreading code is sufficiently long) such that the time-varying effects of the channel cannot be ignored.

In this case, core DEES will have to deal with a code phase offset that varies linearly with time, however, the issue of time-varying Doppler frequencies is no longer present. While DEES, as implemented in Fig. 4.4, can acquire DSSS signals in such an environment, it is unnecessarily burdened by both the SOKT and the FrFT which are used to mitigate the effects of a constant Doppler rate. We now propose a simpler augmentation to core DEES to handle the case of linear time-varying code phase offsets.

With $b_1 = 0$ the DTFT of the output of the nth MF is:

$$Y(n,\omega') = \alpha X(n,\omega')X^*(n,\omega')e^{-j(\omega_0+\omega')d_0}e^{j(\omega_0+\omega')(b_0nL/N)}, \tag{4.16}$$

where ω' is the discrete-time radian Fourier frequency as before. Realizing that the linear CPM is caused by the exp$(j\omega' b_0 nL/N)$ term, we apply a first-order keystone transform (FOKT) to (4.16) which results in:

$$Y(n',\omega') = \alpha X(n',\omega')X^*(n',\omega')e^{-j(\omega_0+\omega')d_0}e^{j\omega_0(b_0n'L/N)}. \tag{4.17}$$

From (4.17) all CPM has been removed since ω' is no longer coupled with b_0. Thus, for the case of a constant Doppler frequency, core DEES need only be augmented with a single FOKT. One possible implementation of this augmentation is shown in Fig. 4.5, where the FOKT must be implemented with interpolation in a similar manner as (4.13).

Interestingly, the absence of the FrFT indicates a single linear transformation can be applied to $\mathbf{Y}$ to produce $\mathbf{Y}_{\mathrm{T}}$, since the Fourier transform and the keystone transform are both linear transforms. This implies that a matrix could be used to obtain $\mathbf{Z}_{\mathrm{T}}$ from $\mathbf{Y}$ instead of the FFT/IFFT and interpolation implementation in Fig. 4.5.

We now develop, step by step, a transformation matrix $\mathbf{T}$ that relates $\mathbf{z}_{\mathrm{T}}$ and $\mathbf{y}$, which are the vectorized versions of $\mathbf{Z}_{\mathrm{T}}$ and $\mathbf{Y}$, respectively. The $ND \times 1$ vector $\mathbf{y}$ is:

$$\mathbf{y} = \left[y_k^{(0)}, y_k^{(1)}, \ldots, y_k^{(N-1)} \right]^T . \tag{4.18}$$

In accordance with Fig. 4.5, the first step is to apply a DFT to each row of the matrix $\mathbf{Y}$ to produce matrix $\mathbf{\Gamma}$. This can be performed by multiplying (4.18) by the $ND \times ND$ transformation matrix $\mathbf{W}$:

$$\mathbf{W} = \begin{bmatrix} \mathbf{W}_D & & & \\ & \mathbf{W}_{D,} & & \\ & & \ddots & \\ & & & \mathbf{W}_D \end{bmatrix}, \tag{4.19}$$

where the off partitions of $\mathbf{W}$ are zero. $\mathbf{W}_D$ is a D-point DFT matrix with entries shifted

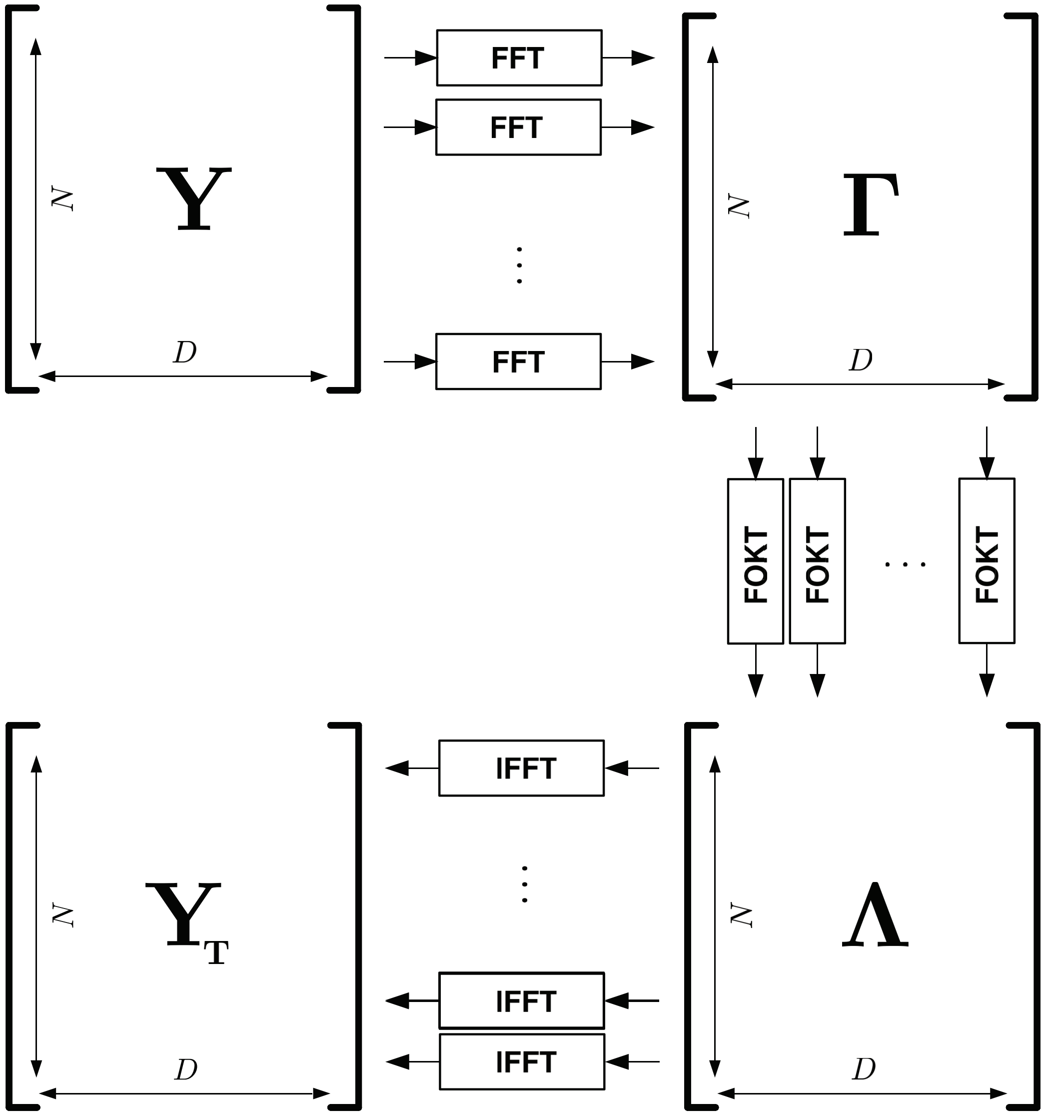

Figure 4.5: Block diagram of the first-order keystone-transform augmentation of core DEES. Only a first-order keystone transform is necessary if Doppler frequency is constant.

to correspond with the convention in (3.13):

$$\mathbf{W}_D = \begin{bmatrix} 1 & w^{\lfloor D/2 \rfloor+1} & w^{2\lfloor D/2 \rfloor+1} & \dots & w^{(D-1)\lfloor D/2 \rfloor+1} \\ 1 & w^{\lfloor N/2 \rfloor+2} & w^{2\lfloor D/2 \rfloor+2} & \dots & w^{(D-1)\lfloor D/2 \rfloor+2} \\ \vdots & \vdots & \vdots & \vdots & \vdots \\ 1 & 1 & 1 & \dots & 1 \\ \vdots & \vdots & \vdots & \vdots & \vdots \\ 1 & w^{\lfloor D/2 \rfloor} & w^{2\lfloor D/2 \rfloor} & \dots & w^{(D-1)\lfloor D/2 \rfloor} \end{bmatrix}. \tag{4.20}$$

where $w = \exp(-j2\pi/D)$ is the primitive Dth root of unity, and where the lower brackets indicate the "floor" operator. The inverse of unitary matrix $\mathbf{W}_D$ is simply $\mathbf{W}_D^{-1} = \mathbf{W}_D^{\dagger}/D$, where $\mathbf{W}_D^{\dagger}$ is the conjugate-transpose of $\mathbf{W}_D$.

The entries of $\mathbf{\Lambda}$ are related to the entries of $\mathbf{\Gamma}$ with relationship:

$$\Lambda_{\tilde{n}l} = \sum_{n=0}^{N-1} \Gamma_{n,l} \operatorname{sinc}\left(\frac{\omega_0}{\omega_0 + \omega'} \tilde{n} - n \right). \tag{4.21}$$

This linear transform can be implemented with transformation matrix $\mathbf{A}$:

$$\mathbf{A} = \begin{bmatrix} \mathbf{A}_{0,0} & \mathbf{A}_{0,1} & \dots & \mathbf{A}_{0,N-1} \\ \mathbf{A}_{1,0} & \mathbf{A}_{1,1} & \dots & \mathbf{A}_{0,N-1} \\ \vdots & \vdots & \vdots & \vdots \\ \mathbf{A}_{N-1,0} & \mathbf{A}_{N-1,1} & \dots & \mathbf{A}_{N-1,N-1} \end{bmatrix}, \tag{4.22}$$

where $\mathbf{A}_{\tilde{n},n}$ is a $D \times D$ diagonal matrix with entries $a(\tilde{n}, n, i) = \operatorname{sinc}\left(\frac{\omega_0}{\omega_0 + 2\pi(i)/D} \tilde{n} - n\right)$ for $i \in \{0, 1, \dots, D-1\}$.

The final step in the core DEES algorithm is to take an N-point FFT of the columns of matrix $\mathbf{Y}_{\mathrm{T}}$ to produce $\mathbf{Z}_{\mathrm{T}}$. Unfortunately, the adjustment from an FFT along the columns to that of an FFT along the rows prevents direct application of a matrix whose structure is similar to (4.20). Instead we must utilize matrix $\mathbf{B}$:

$$\mathbf{B} = \begin{bmatrix} \mathbf{W}_{\lfloor N/2 \rfloor+1,0} & \mathbf{W}_{\lfloor N/2 \rfloor,1} & \cdots & \mathbf{W}_{\lfloor N/2 \rfloor,N-1} \\ \mathbf{W}_{\lfloor N/2 \rfloor+2,0} & \mathbf{W}_{\lfloor N/2 \rfloor+2,1} & \cdots & \mathbf{W}_{\lfloor N/2 \rfloor+2,N-1} \\ \vdots & \vdots & \vdots & \vdots \\ \mathbf{W}_{\lfloor N/2 \rfloor,0} & \mathbf{W}_{\lfloor N/2 \rfloor,1} & \cdots & \mathbf{W}_{\lfloor N/2 \rfloor,N-1} \end{bmatrix}, \tag{4.23}$$

where $\mathbf{W}_{n,l} = w^{(n,l)}\mathbf{I}_N = e^{-j2\pi\frac{n}{N}l}\mathbf{I}_N$, and where $\mathbf{I}_N$ is the $N \times N$ identity matrix.

The total transformation matrix is then:

$$\mathbf{T} = \frac{1}{D}\mathbf{B}\mathbf{W}^{-1}\mathbf{A}\mathbf{W} \tag{4.24}$$

such that $\mathbf{z}_{\mathrm{T}} = \mathbf{T}\mathbf{y}$. The vector $\mathbf{z}_{\mathrm{T}}$ can then be un-vectorized to produce matrix $\mathbf{Z}_{\mathrm{T}}$.

The matrix implementation of the FOKT augmentation for core DEES has niche application, and is not merely an intellectual curiosity. We now compare the computational complexity of the matrix implementation to the FFT implementation as seen in Fig. 4.5, and show that only when N and D are very small is the matrix implementation cheaper to compute.

We follow the same method for computing computational complexity as in Chapter 3, where each complex add or complex multiply as one operation, and assume that memory loads and register shifts have negligible computational cost. Vectorization of matrices is assumed to be computationally negligible as well.

For the FFT implementation, the FFT and IFFT to produce $\mathbf{Y}$ and $\mathbf{Y}_{\mathrm{T}}$, respectively, have a net computational complexity of $\mathcal{O}(2ND\log_2(D))$. The sinc interpolation for the FOKT requires a total of $\mathcal{O}(6ND)$ operations. The FFT of the columns of $\mathbf{Z}_{\mathrm{T}}$ has complexity $\mathcal{O}(ND\log_2(N))$. Thus the total computational complexity of the FFT implementation is $\mathcal{O}(2ND(\log_2(D\sqrt{N}) + 3))$.

The matrix implementation is straight forward to compute, as it involves the multiplication of $ND \times ND$ matrix $\mathbf{T}$ with $ND \times 1$ vector $\mathbf{y}$. The matrix multiplication can be analyzed as the dot product of two length ND vectors, performed ND times, for a total complexity of $\mathcal{O}(2ND(ND-1))$.

We can express the relative complexity of both implementations as:

$$G = \frac{\eta_{\text{Matrix}}}{\eta_{\text{FFT}}} = \frac{ND - \frac{1}{2}}{\log_2(D\sqrt{N}) + 3} \tag{4.25}$$

As (4.25) suggests, the matrix implementation is only more efficient when both N and D are extremely small. For example, $N = 2$ and $D = 3$ already results in similar computational complexities. While intuitively it may seem more efficient to compute $\mathbf{Z}_{\text{T}}$ from $\mathbf{Y}$ in a single transformation, for practical values of N and D the FFT implementation is actually more efficient.

4.4 Numerical Results

To demonstrate the efficacy of DEES, we characterize its acquisition performance in the LEO satellite channel as a function of SNR, and showcase its performance improvement over the core DEES algorithm.

We measure performance as probability of acquisition P_A for a fixed false alarm rate P_{FA}. P_A and P_{FA} are calculated by the fraction of trials that the decision statistic (4.3) exceeds threshold ζ when the signal component of r_k is present and absent, respectively. We assume that inaccurate estimates of $\{d_0, b_0, b_1\}$ will result in (4.3) having a negligible correlation. Since core DEES does not produce Doppler rate estimates, we assume $\hat{b}_1 = 0$ when computing (4.3).

For each SNR we simulate 1000 trials, where each trial has both independent noise and parameter realizations. Each parameter is drawn from a uniform distribution ranging from ± its maximum value; for example d_0 is drawn from $\mathcal{U}(-d_{0,\text{max}}, d_{0,\text{max}})$. The polarity of b_0 and b_1 is enforced to be the same. The phase of α is uniformly distributed, and $|\alpha|$ is drawn from $\mathcal{U}(1, 5)$.

We consider a system with $f_c = 20$ GHz, $f_s = 1/T_c = 60$ MHz, $L = 2^{20}$, and $L/N = 500$ chips. For the LEO satellite channel, we consider the high acceleration regime [18], and select $d_{0,\text{max}} = 20$, $b_{0,\text{max}} = 2.0 \times 10^{-6}$, $b_{1,\text{max}} = 2.36 \times 10^{-15}$, which with the previous system parameters corresponds to a maximum initial Doppler frequency shift of $f_{D,0} = 40$ kHz, a maximum Doppler rate of 5.67 kHz/s, a maximum of 2.10 code phase bins migrated, and a maximum of 1.73 Doppler bins migrated. While the LEO satellite channel is considered a multipath channel with Rician fading [24, 25, 26, 142], we do not model any multipath or fading effects as the key channel impediment of interest is the time-varying Doppler frequency shift.

Shown in Fig. 4.6(a) is P_A vs. SNR (dB) for fixed $P_{FA} = 0.01$ for both DEES (purple curve) and core DEES (dark red curve). As the SNR increases, P_A also increases, with DEES achieving $P_A > 0.9$ when SNR ≥ -41 dB. Once the SNR exceeds -40 dB, P_A has diminishing performance gains with increasing SNR, as $\hat{d}_0$ is now within a fraction of a chip of the true value, and the initial Doppler frequency estimate is now accurate to within tens of Hz. This can be seen in Fig. 4.6(b) which plots the mean absolute error (MAE) for $\{\hat{d}_0, \hat{f}_{D,0}, \hat{f}_A\}$ vs. SNR (dB) for DEES. The MAE of $\hat{d}_0$ (blue curve) and $\hat{f}_{D,0}$ reaches a lower bound that only exists due to the quantization error of DEES. On the other hand, DEES has difficulty obtaining an accurate $\hat{f}_A$ when the SNR is low, as evidenced by the gold curve obtaining an upper bound at low SNR, which exists only due to knowledge of $b_{1,\text{max}}$. However, when SNR ≥ -30 dB, the Doppler rate error is less than 1 kHz/s, which is well within the pull-in range of tracking loops [154].

Due to the presence of both CPM and DFM, DEES outperforms core DEES by a wide margin. This can be seen in Fig. 4.6(a), where core DEES requires approximately 5 dB of additional SNR to achieve the same $P_A \approx 0.7$. The performance benefit of the DEES augmentations are more apparent as SNR increases, as evidenced by the widening gap between the purple and dark red curves. This indicates that the SOKT and phase

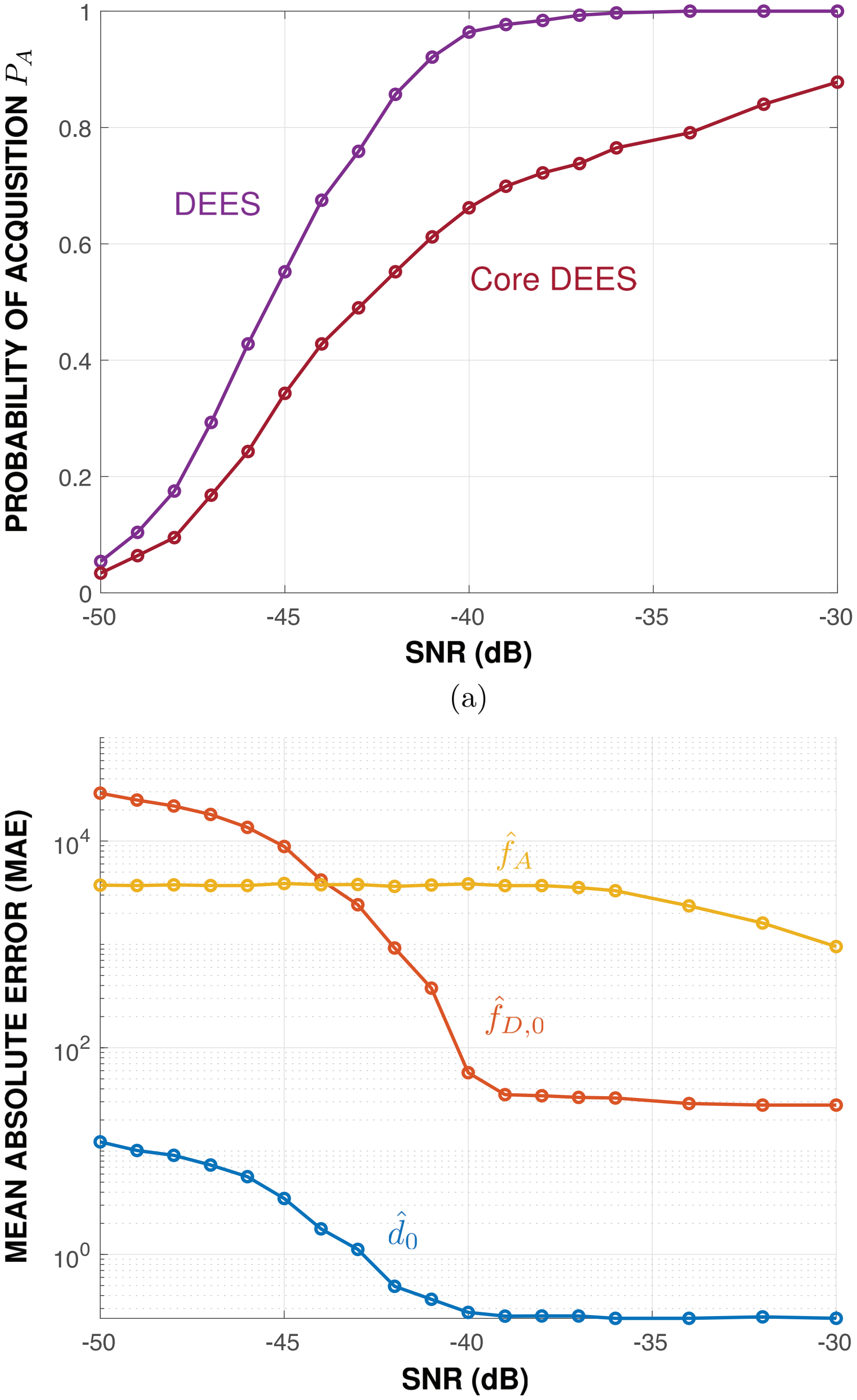

(a)

(b)

Figure 4.6: (a) Probability of acquisition P_A vs. SNR (dB) with fixed $P_{FA} = 0.01$ for DEES (purple curve) and core DEES (dark red curve). (b) DEES Mean absolute error (MAE) vs. SNR (dB) for $\hat{d}_0$ (blue curve), $\hat{f}_{D,0}$ (red curve), and $\hat{f}_A$ (gold curve).

compensation via the FrFT are successful at mitigating the time-varying Doppler effects of the LEO satellite channel.

Given the large performance advantage DEES has over its core form, it would seem natural to compare DEES against the 3D exhaustive search over $\{d_0, b_0, b_1\}$. However, due to our choice of parameters, namely $L = 2^{20}$, is it computationally infeasible to simulate the acquisition performance of the 3D exhaustive search. Using the methodology described in the end of Section 4.3, we briefly compare the computational complexities of both algorithms, and show that the computational complexity of DEES is less than that of the 3D search for practical parameters.

Unlike the 2D exhaustive search described in Chapter 3, the 3D exhaustive search cannot first compensate the received signal r_k by the Doppler frequency (and Doppler rate) due to the time-varying channel delay. Instead, the 3D exhaustive search must compute the correlation in (4.3) for all possible candidate tuples of $\{d_0, b_0, b_1\}$. Assuming the received signal r_k is of length $(L + D)$, it takes a total of $2(L + D)$ operations to compute the correlation and its L_2 norm for a given candidate tuple. If there are N candidate initial Doppler frequencies, and M candidate Doppler rates, there are total of MND candidate tuples. This means the 3D exhaustive search has complexity $\mathcal{O}(2MND(L + D))$.

We now characterize the computational complexity of DEES. From Chapter 3, core DEES has complexity $\mathcal{O}(D(2L + N[\log_2(N) - 1]))$, which means we need only determine the complexity of the augmentations. Referencing Fig. 4.4, the FFT and IFFT to produce $\mathbf{\Gamma}$ and $\mathbf{Y}_{\mathrm{T}}$ have total complexity $\mathcal{O}(2ND\log_2(D))$. Each SOKT has complexity $\mathcal{O}(7ND)$. Since we assume that a single discrete FrFT on a length n sequence has complexity $n\log_2(n)$ [155, 156], the D length N FrFTs searching over M candidate Doppler rates, along with the phase compensation have total complexity $\mathcal{O}(D(MN\log_2(N) + N + 8))$. This means DEES has total computational complexity $\mathcal{O}(2ND\log_2(N^{\frac{(M+1)}{2}}D) + 14ND + 2LD + 8D)$.

From this analysis it should be clear for practical values (e.g. $N >> 1$ or $M >>$

1) DEES has significantly lower computational complexity when compared to the 3D exhaustive search. For the parameters used to produce the results in Fig. 4.6, the 3D exhaustive search has a computational complexity approximately 10^5 times larger than DEES.

4.5 Summary

In this chapter we have introduced DEES, an efficient algorithm that can acquire DSSS signals in an environment with time-varying Doppler frequency shifts. DEES utilizes a composition of the SOKT and the FrFT to reduce an expensive 3D search over initial code phase offset, Doppler frequency, and Doppler rate into a 2D search with limited post-processing. Numerical results show DEES can acquire long-code DSSS signal in the high-acceleration regime of the LEO satellite channel, whereas core DEES struggles and is significantly outperformed due to its inability to deal with both code phase migration and Doppler frequency migration.

CHAPTER 5

NONCOOPERATIVE DSSS DETECTION OF QPSK CODED SIGNALS

In this chapter we shift our attention to the noncooperative detection problem, in which an eavesdropper armed with a detector is interested in detecting the presence of a DSSS signal buried in noise [157]. Due to the noncooperative nature of the problem, the detector lacks knowledge of key parameters such as the spreading sequence or the type of spreading code utilized, and thus cannot take advantage of processing gain to aid in detecting a signal buried deep below the noise floor. Given the difficulty of noncooperative detection, the detector should exploit every possible advantage available to it to improve performance. In particular, we explore the advantage of a detector that knows the DSSS signal is coded using QPSK.

We propose a multi-antenna likelihood ratio test detector that takes advantage of knowledge of the signal alphabet, and whose computational complexity grows linearly with the detector observation window length. We compare the proposed alphabet-aware detector against a battery of benchmark detectors, and characterize the benefits of alphabet awareness for detection through both numerical simulation and statistical analysis.

5.1 Received Signal Model

We adopt a simplified received signal model with no channel dispersion, perfect channel state information, identical signal delays for each antenna, and perfect carrier synchronization. Implicit in such a model is the assumption the detector has knowledge of both the carrier frequency and the signal bandwidth. Despite these limitations our model still captures the essence of the noncooperative detection problem. We will later relax the assumption that the detector has a priori knowledge of the channel state. We model the detection problem as a composite binary hypothesis test where $\mathcal{H}_0$ is the null hypothesis in which only noise was received, and $\mathcal{H}_1$ is the alternative hypothesis in which signal plus noise was received. The model for a vector of N samples at the kth antenna is:

$$\begin{cases} \mathcal{H}_1 : \mathbf{r}_k = \alpha_k \mathbf{s} + \mathbf{w}_k \\ \mathcal{H}_0 : \mathbf{r}_k = \mathbf{w}_k \end{cases} \tag{5.1}$$

where $\mathbf{r}_k$ is an $N \times 1$ received vector of baseband samples at the kth antenna, where $k \in \{0, 1, \ldots, K-1\}$, where K is the number of antennas, where α_k is the complex channel gain to the kth antenna, where $\mathbf{s}$ is the signal vector, and where $\mathbf{w}_k$ is the noise vector at the kth antenna. We assume that the components of $\mathbf{s}$ are *i.i.d.* uniform over the QPSK alphabet $\mathscr{A} = \{\pm 1 \pm j\}$, and that the components of the noise vector $\mathbf{w}_k$ are *i.i.d.* $\mathcal{CN}(0, 2\sigma^2)$, and are independent for each antenna $k \in \{0, 1, \ldots, K-1\}$.

The *i.i.d.* model for the signal vector components in (5.1) reflects our assumptions that the detector has no knowledge of the spreading sequence, the modulating information symbols, and that the spread coding period is longer than the detector observation window, which prevents the detector from exploiting any autocorrelative properties of the spreading code. In effect, these assumptions make the DSSS signal indistinguishable from a high-speed low-SNR non-spread single-carrier QPSK signal, whose symbol rate is equal to the chip rate. Subsequently, although noncooperative detection of DSSS signals is the key motivation for this work, the results in this chapter are also applicable to unspread QPSK signals.

This chapter is concerned with the noncooperative detection problem: Given $\{\mathbf{r}_0, \mathbf{r}_1, \ldots, \mathbf{r}_{K-1}\}$ and knowledge of the model in (5.1), with the noise variance and signal alphabet also known, decide whether the signal is present ($\mathcal{H}_1$) or absent ($\mathcal{H}_0$).

5.2 Proposed Detector

According to the Neyman-Pearson criterion, the test that maximizes the probability of detection P_D for a given false-alarm probability P_{FA} is the likelihood ratio test (LRT), which compares the ratio of likelihoods under $\mathcal{H}_0$ and $\mathcal{H}_1$ to a threshold [69, 70, 108]. If the likelihood ratio exceeds a threshold the null hypothesis $\mathcal{H}_0$ is rejected, and the presence of a signal is declared. Otherwise, the null hypothesis is accepted and the absence of a signal is declared.

Applying the LRT directly to binary hypothesis testing problem in (5.1) leads to the proposed alphabet-aware detector, which in terms of $\mathbf{R} = [\mathbf{r}_0, \mathbf{r}_1, \ldots, \mathbf{r}_{K-1}]$ is:

$$L_{\text{AA}} = \log\left[\frac{f(\mathbf{R}|\mathcal{H}_1)}{f(\mathbf{R}|\mathcal{H}_0)}\right]. \tag{5.2}$$

The numerator in (5.2) can be rewritten as:

$$\begin{aligned} f(\mathbf{R}|\mathcal{H}_1) &= \mathbb{E}_{\mathbf{s}}\left[\left(\frac{1}{2\pi\sigma^2}\right)^{NK} e^{-\sum_{k=0}^{K-1}\frac{||\mathbf{r}_k-\alpha_k\mathbf{s}||^2}{2\sigma^2}}\right] \\ &= \mathbb{E}_{\mathbf{s}}\left[\left(\frac{1}{2\pi\sigma^2}\right)^{NK} e^{-\sum_{k=0}^{K-1}\frac{||\mathbf{r}_k||^2+||\alpha_k\mathbf{s}||^2}{2\sigma^2}} e^{\sum_{k=0}^{K-1}\frac{\mathrm{Re}\{\alpha_k^*\mathbf{s}^\dagger\mathbf{r}_k\}}{\sigma^2}}\right] \\ &= \left(\frac{1}{2\pi\sigma^2}\right)^{NK} \frac{1}{2^{2N}}\sum_{i=1}^{2^{2N}} e^{-\sum_{k=0}^{K-1}\frac{||\mathbf{r}_k||^2+||\alpha_k\mathbf{s}_i||^2}{2\sigma^2}} e^{\sum_{k=0}^{K-1}\frac{\mathrm{Re}\{\alpha_k^*\mathbf{s}_i^\dagger\mathbf{r}\}}{\sigma^2}} \\ &= \left(\frac{1}{2\pi\sigma^2}\right)^{NK} e^{-\sum_{k=0}^{K-1}\frac{||\mathbf{r}_k||^2+2N|\alpha_k|^2}{2\sigma^2}} \\ &\quad \prod_{n=0}^{N-1}\cosh\left(\frac{1}{\sigma^2}\,\mathrm{Re}\sum_{k=0}^{K-1}\{\alpha_k^* r_k(n)\}\right)\cosh\left(\frac{1}{\sigma^2}\,\mathrm{Im}\sum_{k=0}^{K-1}\{\alpha_k^* r_k(n)\}\right), \end{aligned} \tag{5.3}$$

where $\mathbf{s}^\dagger$ is the Hermitian-transpose of $\mathbf{s}$, where $\mathbf{s}_i$ refers to the ith vector in an ordered list of the 2^{2N} possible QPSK signal vectors, where $||\mathbf{s}||^2 = 2N$, and where α_k^* is the complex conjugate of α_k.

The last step in (5.3) is a significant reduction in computational complexity, because it reduces the 2^{2N} computations (exponential in N) to $2N$ computations (linear in N), and allows for the practical implementation of the AA statistic even for large observation windows. Such a reduction is possible due to the constellation positions of QPSK, which lie along the real and imaginary axes.

The denominator in (5.2) is:

$$f(\mathbf{R}|\mathcal{H}_0) = \left(\frac{1}{2\pi\sigma^2}\right)^{NK} e^{-\sum_{k=0}^{K-1}\frac{||\mathbf{r}_k||^2}{2\sigma^2}}. \tag{5.4}$$

Substituting (5.3) and (5.4) into (5.2) results in:

$$\begin{aligned} L_{\text{AA}} = \sum_{n=0}^{N-1} \log\Bigg[&\cosh\left(\frac{1}{\sigma^2}\sum_{k=0}^{K-1}\text{Re}\{\alpha_k^* r_k(n)\}\right) \\ &\cosh\left(\frac{1}{\sigma^2}\sum_{k=0}^{K-1}\text{Im}\{\alpha_k^* r_k(n)\}\right)\Bigg] - \sum_{k=0}^{K-1}\frac{N|\alpha_k|^2}{\sigma^2}. \end{aligned} \tag{5.5}$$

The AA decision statistic in (5.5) accommodates for multiple antennas by first maximal-ratio combining (MRC) the K received signal vectors, yielding $\mathbf{z} = \sum_{k=0}^{K-1} \alpha_k^* \mathbf{r}_k$. The detector then averages over all possible QPSK signal combinations with the two cosh functions.

A block diagram of the AA detector is shown in Fig. 5.1. In terms of $z(n) = z_{\text{R}}(n) + jz_{\text{I}}(n)$, we can write $L_{\text{AA}} = \sum_n J(z(n))$, where $J(x + jy) = \text{logcosh}(x/\sigma^2) + \text{logcosh}(y/\sigma^2)$. For brevity the last term of (5.5) was omitted from the block diagram; doing so does not affect detector performance as it is equivalent to changing the detection threshold.

5.3 Benchmark Detectors

We compare the performance of our proposed AA detector to four benchmark detectors. The first two benchmarks of interest are the AA detector's alphabet-unaware (AU) counterpart, and the energy detector (ED). Both the AU detector and ED lack knowledge of the signal alphabet, making them prime candidates for benchmarking the benefits of alphabet awareness. The other two benchmarks of interest are the alphabet-aware channel-unaware (AA-CU) and alphabet-unaware channel-unaware (AU-CU) detectors, which are versions of the AA and AU detectors that do not have a priori knowledge of

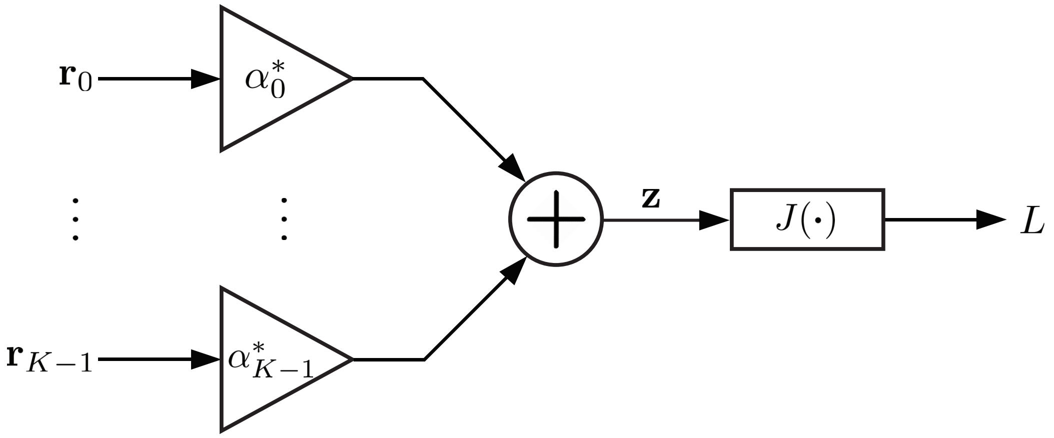

Figure 5.1: Block diagram of both the proposed alphabet-aware detector and the benchmark alphabet-unaware detector. Both detectors consist of a maximal-ratio combining front end, followed by a mapping from a complex vector to a scalar.

the channel gains $\{\alpha_0, \alpha_1, \ldots, \alpha_{K-1}\}$. In practice, the detector does not have a priori knowledge of the channel in a noncooperative detection scenario; the CU detectors are practical realizations of both the AA and AU detectors, respectively.

With the exception of ED, each of the benchmark detectors' decision statistic can derived by applying the generalized likelihood ratio test (GLRT) to the binary hypothesis testing problem in (5.1). For some of the benchmark detectors, it is convenient to adopt a mathematically equivalent vectorized received signal model. Namely:

$$\begin{cases} \mathcal{H}_1 : \boldsymbol{\mathcal{R}} = \mathbf{H}\mathbf{s} + \mathbf{W} \\ \mathcal{H}_0 : \boldsymbol{\mathcal{R}} = \mathbf{W} \end{cases} \tag{5.6}$$

where $\boldsymbol{\mathcal{R}} = [\mathbf{r}_0; \mathbf{r}_1; \ldots; \mathbf{r}_{K-1}] = \text{vec}(\mathbf{R})$ is the $NK \times 1$ received signal vector and is the vectorization of matrix $\mathbf{R}$, $\mathbf{s}$ is the $N \times 1$ transmitted signal vector, $\mathbf{W}$ is the $NK \times 1$ noise vector with entries $\mathbf{W} = [\mathbf{w}_0, \mathbf{w}_1, \ldots, \mathbf{w}_{K-1}]$, and $\mathbf{H}$ is a $NK \times N$ channel coefficient matrix with entries $\mathbf{H} = [\alpha_0 \mathbf{I}_N; \alpha_1 \mathbf{I}_N; \ldots; \alpha_{K-1} \mathbf{I}_N]$. We will shift between the notations when convenient to maintain the compactness of expressions.

Alphabet-unaware detector

The first benchmark we consider is the alphabet-unaware (AU) detector, which as its name suggests does not know the distribution of s. Rather than assume a potentially incorrect distribution for s, the alphabet-unaware detector models s as a vector of deterministic unknowns and applies the GLRT to (5.1), in which the unknown parameters under each hypothesis are replaced with their maximum-likelihood estimates (MLE) [69, 70].

The PDF of $\mathbf{R}$ under $\mathcal{H}_0$ is the same as (5.4). The PDF of $\mathbf{R}$ under $\mathcal{H}_1$ is:

$$\begin{aligned}
\arg\max_{\mathbf{s}} f(\boldsymbol{\mathcal{R}};\mathbf{s}|\mathcal{H}_1) &= \arg\max_{\mathbf{s}} \left(\frac{1}{2\pi\sigma^2}\right)^{NK} e^{-\frac{||\boldsymbol{\mathcal{R}}-\mathbf{Hs}||^2}{2\sigma^2}} \\
&= \arg\max_{\mathbf{s}} \left(\frac{1}{2\pi\sigma^2}\right)^{NK} e^{-\frac{||\boldsymbol{\mathcal{R}}||^2+||\mathbf{Hs}||^2}{2\sigma^2}} e^{\frac{\mathrm{Re}\{(\mathbf{Hs})^\dagger\boldsymbol{\mathcal{R}}\}}{\sigma^2}} \\
&= \left(\frac{1}{2\pi\sigma^2}\right)^{NK} e^{-\frac{1}{2\sigma^2}\left[||\boldsymbol{\mathcal{R}}||^2+\frac{||\mathbf{H}^\dagger\boldsymbol{\mathcal{R}}||^2}{\sum_{k=0}^{K-1}|\alpha_k|^2}-2\frac{||\mathbf{H}^\dagger\boldsymbol{\mathcal{R}}||^2}{\sum_{k=0}^{K-1}|\alpha_k|^2}\right]} \\
&= \left(\frac{1}{2\pi\sigma^2}\right)^{NK} e^{-\frac{1}{2\sigma^2}\left[\sum_{k=0}^{K-1}||\mathbf{r}_k||^2-\frac{||\sum_{k=0}^{K-1}\alpha_k^*\mathbf{r}_k||^2}{\sum_{k=0}^{K-1}|\alpha_k|^2}\right]},
\end{aligned} \tag{5.7}$$

where the MLE of s is $\hat{\mathrm{s}} = (\mathbf{H}^\dagger\mathbf{H})^{-1}\mathbf{H}^\dagger\boldsymbol{\mathcal{R}}$, and where $\mathbf{H}^\dagger$ is the conjugate-transpose of $\mathbf{H}$.

A few important relationships were utilized to simplify (5.7). First consider the reduction of $\mathrm{Re}\{(\mathbf{H}\hat{\mathrm{s}})^\dagger\mathbf{H}\}$ which was introduced in the second line:

$$\begin{aligned}
\mathrm{Re}\{(\mathbf{H}\hat{\mathrm{s}})^\dagger\mathbf{H}\} &= \mathrm{Re}\{(\mathbf{H}^\dagger\boldsymbol{\mathcal{R}})^\dagger(\mathbf{H}^\dagger\mathbf{H})^{-1}\mathbf{H}^\dagger\boldsymbol{\mathcal{R}})\} \\
&= \left(\sum_{k=0}^{K-1}|\alpha_k|^2\right)^{-1} \mathrm{Re}\{\mathbf{I}_N(\mathbf{H}^\dagger\mathbf{R})^\dagger\mathbf{H}^\dagger\boldsymbol{\mathcal{R}})\} \\
&= \left(\sum_{k=0}^{K-1}|\alpha_k|^2\right)^{-1} ||\mathbf{H}^\dagger\boldsymbol{\mathcal{R}}||^2,
\end{aligned} \tag{5.8}$$

where $(\mathbf{H}^\dagger\mathbf{H})^{-1} = \left(\sum_{k=0}^{K-1}|\alpha_k|^2\right)^{-1}\mathbf{I}_N$ commutes with $(\mathbf{H}^\dagger\boldsymbol{\mathcal{R}})^\dagger$ due to identity properties of the former. We now shift our attention to the other quantity of interest, $||\mathbf{H}\hat{\mathrm{s}}||^2$, which can be reduced as follows:

$$\begin{aligned} ||\mathbf{H}\hat{\mathbf{s}}||^2 &= ||\mathbf{H}(\mathbf{H}^\dagger\mathbf{H})^{-1}\mathbf{H}^\dagger\boldsymbol{\mathcal{R}}||^2 \\ &= \left(\sum_{k=0}^{K-1}|\alpha_k|^2\right)^{-2}||\mathbf{H}\mathbf{H}^\dagger\boldsymbol{\mathcal{R}}||^2 \\ &= \left(\sum_{k=0}^{K-1}|\alpha_k|^2\right)^{-1}||\mathbf{H}^\dagger\boldsymbol{\mathcal{R}}||^2. \end{aligned} \tag{5.9}$$

Taking the logarithm of the ratio of (5.7) and (5.4) results in the AU decision statistic:

$$L_{\text{AU}} = \log\left[\frac{\underset{\mathbf{s}}{\arg\max} f(\mathbf{R};\mathbf{s}|\mathcal{H}_1)}{f(\mathbf{R}|\mathcal{H}_0)}\right] = \frac{||\sum_{k=0}^{K-1}\alpha_k^*\mathbf{r}_k||^2}{\sigma^2\sum_{k=0}^{K-1}|\alpha_k|^2}. \tag{5.10}$$

As (5.10) suggests, this detector first combines the signals from the different antennas using MRC, and then performs ED after combining. Ignoring the constant term in the denominator, the AU detector has the same block diagram as the AA detector as shown in Fig. 5.1, except with $J(x+jy) = x^2 + y^2$ instead of $J(x+jy) = \text{logcosh}(x/\sigma^2) + \text{logcosh}(y/\sigma^2)$. As before, ignoring the constant does not impact detection performance.

Recognizing that (5.10) follows a noncentral χ^2 distribution with $2N$ degrees of freedom and noncentrality parameter $\delta = 2N$ SNR under $\mathcal{H}_1$, the probability of detection of the AU detector is [158]:

$$P_{D,\text{AU}} = Q_N(\sqrt{\delta}, \sqrt{\eta}) \tag{5.11}$$

where $Q_M(a,b) = \int_b^\infty x(\frac{x}{a})^{M-1}e^{-\frac{x^2+a^2}{2}}I_{M-1}(ax)\,dx$ is the Marcum-Q function [159] and $I_{M-1}(ax)$ is the modified Bessel function of order $M-1$. Recognizing that (5.10) follows a central χ^2 distribution with $2N$ degrees of freedom under $\mathcal{H}_0$, the probability of false alarm is:

$$P_{FA,\text{AU}} = 1 - \frac{\gamma(N,\eta/2)}{\Gamma(N)} \tag{5.12}$$

where $\Gamma(x) = \int_0^\infty x^{z-1}e^{-x}dx$ is the gamma function, and where $\gamma(z,x) = \int_0^x t^{z-1}e^{-t}dt$ is the lower incomplete gamma function [158].

In practice, even if the AU detector had a priori knowledge of the channel gains, it would be difficult for the detector to obtain synchronization due to its alphabet-unawareness. Thus, the received signal model in (5.1) is unrealistic for any alphabet-unaware detector that relies on coherent combining before performing detection. While this idealized received signal model results in optimistic detector performance from alphabet-unaware detectors, these detectors now represent a higher benchmark for the proposed AA detector to overcome, and allows for the direct characterization of the effects of detector alphabet-awareness.

Energy detector

The second benchmark we consider is the energy detector (ED). Like AU, the ED does not have knowledge of the signal alphabet, but unlike AU the ED has no knowledge of the channel gains. As the name suggests the ED uses the energy of the observations to determine the presence or absence of the signal. The ED decision statistic is:

$$L_{\text{ED}} = \frac{1}{\sigma^2} \sum_{k=0}^{K-1} ||\mathbf{r}_k||^2, \tag{5.13}$$

which follows a noncentral χ^2 distribution with $2NK$ degrees of freedom and noncentrality parameter $\delta = 2N$ SNR under $\mathcal{H}_1$, and a central χ^2 distribution with $2NK$ degrees of freedom under $\mathcal{H}_0$. Subsequently the analytical expression for the detection and false alarm rates are:

$$P_{D,\text{ED}} = Q_{NK}(\sqrt{\delta}, \sqrt{\eta}), \tag{5.14}$$

and

$$P_{FA,\text{ED}} = 1 - \frac{\gamma(NK, \eta/2)}{\Gamma(NK)}, \tag{5.15}$$

respectively. These expressions are the same as the AU detector's P_D and P_{FA} expressions, except the $2N$ degrees of freedom have been replaced with $2NK$ degrees of freedom.

It is important to notice the performance of ED scales with NK at a given SNR. For example, if the number of antennas is halved, than the observation window length must be doubled to main the same detector performance. For large values of NK or as SNR $\to \infty$, the ED decision statistic approximately follows a normal distribution [160] with $L_{\text{ED}} \sim \mathcal{N}(2N(K+\rho), 4N(K+\rho))$ under $\mathcal{H}_1$, and $L_{\text{ED}} \sim \mathcal{N}(2NK, 4NK)$ under $\mathcal{H}_0$.

Alphabet-aware channel-unaware detector

The third benchmark is the channel-unaware version of the proposed AA detector, namely the AA-CU detector. There are two approaches of modeling the unknown channel gains α_k. One approach is to take the Bayesian perspective and assume a distribution for α_k, and apply the LRT to obtain the decision statistic. This requires a priori knowledge of the channel environment the detector will be engaged in, and an inaccurate assumption will lead to suboptimal detector performance. Furthermore, even if the distribution of the channel gains were known, in many cases it is analytically intractable to derive the decision statistic; this is shown in Appendix A. Subsequently, we take a similar approach as before and model the α_k as deterministic unknowns.

The AA-CU decision statistic is obtained by applying the GLRT to (5.1); its derivation follows in a similar fashion as the AA detector. The resulting decision statistic is:

$$\begin{aligned} L_{\text{AA-CU}} = \sum_{n=0}^{N-1} \log \bigg[&\cosh\bigg(\frac{1}{\sigma^2} \sum_{k=0}^{K-1} \operatorname{Re}\{\hat{\alpha}_k^* r_k(n)\} \bigg) \\ &\cosh\bigg(\frac{1}{\sigma^2} \sum_{k=0}^{K-1} \operatorname{Im}\{\hat{\alpha}_k^* r_k(n)\} \bigg) \bigg] - \sum_{k=0}^{K-1} \frac{N|\hat{\alpha}_k|^2}{\sigma^2}. \end{aligned} \tag{5.16}$$

where $\hat{\boldsymbol{\alpha}} = [\hat{\alpha}_0, \hat{\alpha}_1, \ldots, \hat{\alpha}_{K-1}] = \arg\max_{\boldsymbol{\alpha}} f(\mathbf{R}; \boldsymbol{\alpha}|\mathcal{H}_1)$. A closed-form solution for $\hat{\boldsymbol{\alpha}}$ is not known, but it can be estimated using numerical techniques such as gradient descent. The relevant equation for a gradient descent implementation of the AA-CU statistic can be found in the Appendix B.

Alphabet-unaware channel-unaware detector

Finally, the last benchmark considered is the channel-unaware version of the AU detector, namely the AU-CU detector. Proposed in [126], the AU-CU detector is derived by applying the GLRT to (5.1) assuming both s and $\boldsymbol{\alpha} = [\alpha_0, \alpha_1, \ldots, \alpha_{K-1}]$ are vectors of deterministic unknowns. Following a treatment of [126], the PDF of $\mathbf{R}$ under $\mathcal{H}_1$ is:

$$\begin{aligned} f(\mathbf{R}; \boldsymbol{\alpha}, \mathrm{s}|\mathcal{H}_1) &= \arg\max_{\boldsymbol{\alpha},\mathbf{s}} \left(\frac{1}{2\pi\sigma^2}\right)^{NK} e^{-\sum_{k=0}^{K-1} \frac{||\mathbf{r}_k - \alpha_k \mathbf{s}||^2}{2\sigma^2}} \\ &= \arg\max_{\boldsymbol{\alpha},\mathbf{s}} \left(\frac{1}{2\pi\sigma^2}\right)^{NK} e^{-\sum_{k=0}^{K-1} \frac{||\mathbf{r}_k||^2 + ||\alpha_k \mathbf{s}||^2}{2\sigma^2}} e^{\sum_{k=0}^{K-1} \frac{\mathrm{Re}\{(\alpha_k \mathbf{s})^\dagger \mathbf{r}_k\}}{\sigma^2}} \end{aligned} \tag{5.17}$$

The ML estimate of α_k, $\hat{\alpha}_k = \frac{\mathbf{s}^\dagger \mathbf{r}_k}{||\mathbf{s}||^2}$ [126, 124]. Substituting this in to the previous expression yields:

$$\begin{aligned} f(\mathbf{R}; \boldsymbol{\alpha}, \mathrm{s}|\mathcal{H}_1) &= \arg\max_{\boldsymbol{\alpha}} \left(\frac{1}{2\pi\sigma^2}\right)^{NK} e^{-\sum_{k=0}^{K-1} \frac{||\mathbf{r}_k||^2 - \frac{|\mathbf{s}^\dagger \mathbf{r}_k|^2}{||\mathbf{s}||^2}}{2\sigma^2}} \\ &= \arg\max_{\boldsymbol{\alpha}} \left(\frac{1}{2\pi\sigma^2}\right)^{NK} e^{-\sum_{k=0}^{K-1} \frac{||\mathbf{r}_k||^2}{2\sigma^2} + \sum_{k=0}^{K-1} \frac{1}{2\sigma^2} \frac{\mathbf{s}^\dagger \mathbf{R}\mathbf{R}^\dagger \mathbf{s}}{||\mathbf{s}||^2}} \end{aligned} \tag{5.18}$$

The ML estimate of s is that which maximizes:

$$\arg\max_{\mathbf{s}} \frac{\mathbf{s}^\dagger \mathbf{R}\mathbf{R}^\dagger \mathbf{s}}{||\mathbf{s}||^2}. \tag{5.19}$$

This quantity is the Rayleigh quotient, and is maximized when $\mathrm{s} = \lambda_{\text{max}}(\boldsymbol{\Phi})$ where $\boldsymbol{\Phi} = \mathbf{R}^\dagger \mathbf{R}$ [124, 126]. Thus $\hat{\mathrm{s}} = \lambda_{\text{max}}(\boldsymbol{\Phi})$.

The AU-CU decision statistic is then:

$$\begin{aligned} L_{\text{AU-CU}} = \log\left[\frac{\arg\max_{\boldsymbol{\alpha},\mathbf{s}} f(\mathbf{R}; \boldsymbol{\alpha}, \mathrm{s}|\mathcal{H}_1)}{f(\mathbf{R}|\mathcal{H}_0)}\right] &= \frac{1}{\sigma^2}\lambda_{\text{max}}(\boldsymbol{\Phi}) \\ = \frac{||\sum_{k=0}^{K-1} \tilde{\alpha}_k^* \mathbf{r}_k||^2}{\sigma^2 \sum_{k=0}^{K-1} |\tilde{\alpha}_k^*|^2}, \end{aligned} \tag{5.20}$$

where $\lambda_{\text{max}}\big(\mathbf{\Phi}\big)$ is the maximum eigenvalue of the $K \times K$ Gramian matrix $\mathbf{\Phi} = \mathbf{R}^\dagger\mathbf{R}$, and where $\tilde{\alpha}_k$ is the maximum-likelihood (ML) estimate of the kth channel gain. Analytic expressions for the cumulative distribution function (CDF) and probability density function (PDF) of (5.20) have been derived in [161].

The second form of the decision statistic in the last line of (5.20) can be derived by estimating the channel gains before estimating the signal vector, which is different from the derivation in [126]. It should be noted that the channel estimates $\tilde{\alpha}_k$ differ from the channel estimates $\hat{\alpha}_k$ in (5.16), as $\tilde{\alpha}_k$ is obtained when s is unknown. The second form of the AU-CU statistic is more insightful as it shows that the AU-CU detector takes advantage of multiple antennas with MRC, and that the only difference between the AU detector and the AU-CU detector is the use of the actual channel gains in place of their estimates.

The ED can be related to the AU-CU detector in terms of the number of eigenvalues utilized, since the ED statistic can also be written as $L_{\text{ED}} = \text{Tr}(\mathbf{\Phi})/\sigma^2 = \sum_{k=0}^{K-1} \lambda_k(\mathbf{\Phi})/\sigma^2$. Thus, while the AU-CU statistic takes the maximum eigenvalue of $\mathbf{\Phi}$, the ED statistic sums over all eigenvalues. It follows that the AU-CU statistic reduces to ED when there is only a single antenna ($K = 1$). Furthermore, the AU statistic is also equivalent to ED when $K = 1$, since the extra constant factor in the denominator is equivalent to changing the detection threshold.

It is important to note that, with the exception of ED, all the benchmark detectors as well as the proposed AA detector share the same topology shown in Fig. 5.1. They all first perform MRC, apply a nonlinear operator $J(\cdot)$ to each component of the resulting combined vector, and finally sum over the vector components to produce a scalar decision statistic. The CU detectors must first obtain channel estimates before performing MRC, but otherwise follow the same process.

The only difference between the alphabet-aware and alphabet-unaware detectors is the nonlinear operator used. The alphabet-aware detectors use $J(x) = \text{logcosh}(x/\sigma^2)$, while alphabet-unaware detectors use $J(x) = x^2$. This distinction is not significant at low SNR,

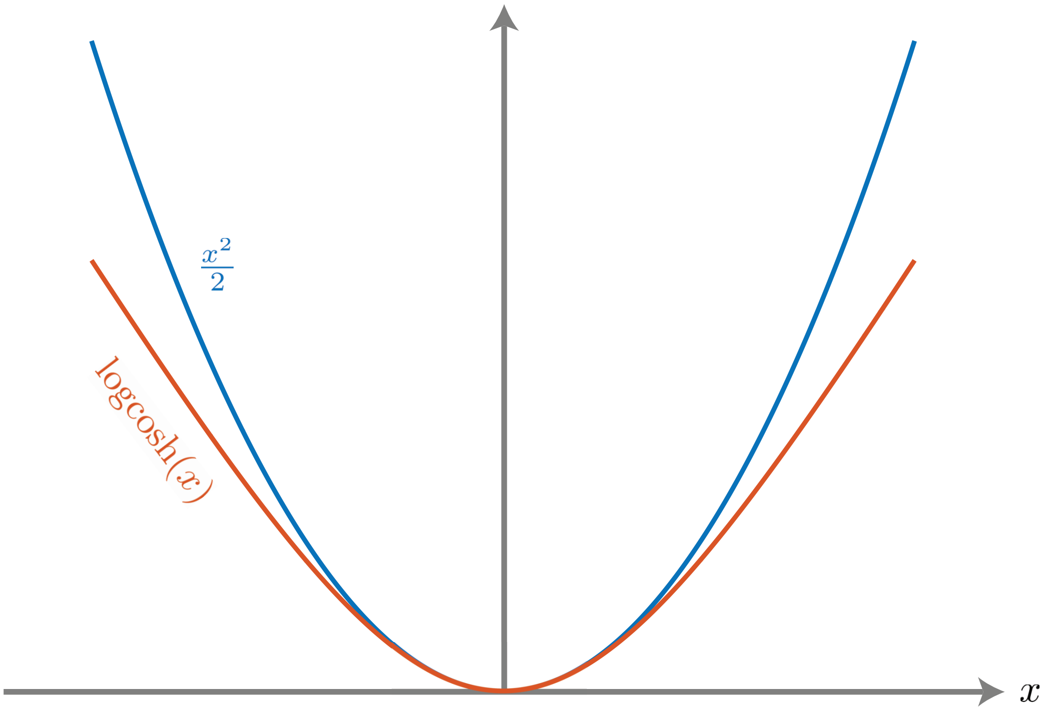

Figure 5.2: Comparison of logcosh(x) and $x^2/2$.

since $\log[\cosh(x)] \approx x^2/2$ for small values of x, which often holds when the SNR is low. Both functions are illustrated in Fig. (5.2), where they both exhibit similar behavior when x is small.

With the exception of ED, all the benchmark detectors discussed were derived by applying the GLRT to the binary hypothesis testing problem in (5.1). These detectors have inherently suboptimal detection performance within their particular class, as the GLRT is not optimal in the Neyman-Pearson sense, although it can be asymptotically optimal under certain conditions [162]. However, the GLRT is the uniformly most powerful invariant (UMPI) test for signal detection problems that fit the linear model, is in general asymptotically UMPI as the number of observations approaches infinity $(N \to \infty)$ [163], and is invariant to the same set of transformations that the original hypothesis testing problem is invariant to [122, 164]. As the name suggests, the UMPI test has the highest statistical power among tests that are invariant to a particular transformation group. For example, the GLRT AU-CU detector does not necessarily maximize P_D for a given P_{FA}

among detectors that neither have a priori knowledge of the channel gains nor knowledge of the signal alphabet, but it does provide optimal detection performance among detectors that are invariant with respect to element-wise rotations of the received signal vector in the limit as $N \to \infty$.

5.4 Performance Characterization

In this section we compare the performance of the proposed detector to its benchmarks as a function of three key parameters: the number of antennas K, the observation window length N, and the SNR.

We begin by describing the simulation methodology for numerical results presented later in this section. For a given SNR, N, K, and P_{FA}, each decision statistic is simulated with $M = 10^5$ trials when the signal is present and M trials when the signal is absent. Each trial has independent realizations of the noise vector, the signal vector, and the complex channel gains α_k, each of which is modeled as $\alpha_k = e^{j\theta_k}$ where each θ_k is uniformly distributed over the interval $[0, 2\pi)$. The SNR is the same at each of the K antennas. The probabilities P_D and P_{FA} are estimated by the fractions of trials that the test statistic exceeds the threshold when the signal is present and absent, respectively.

For all detectors we measure performance as probability of detection P_D for a given false alarm rate P_{FA}. Therefore every detector must choose its own threshold to achieve the desired P_{FA}. We numerically determine the thresholds for the AA-CU, AU-CU, and AA detectors. The thresholds for AU and ED can be determined analytically, since both of these detectors have closed-form expressions for P_{FA}.

This section is divided into two subsections. In the first subsection we characterize detector performance when the SNR is low, and show that in this case alphabet awareness does not result in performance gain, regardless of the values of the other key parameters. In the second subsection we examine the conditions in which alphabet awareness results in appreciable performance gains, followed by a brief discussion on detector computational complexity.

5.4.1 Low-SNR Performance

We now investigate the performance of each detector in the low SNR regime. The per-antenna SNR at the kth antenna is $\text{SNR}_k = \rho_k = \frac{|\alpha_k|^2 ||\mathbf{s}||^2}{2\sigma^2 N}$, and the overall SNR is $\rho = \sum_{k=0}^{K-1} \rho_k$. The first parameter of interest is the observation window length N.

Increasing N improves the detection performance of all detectors considered. This effect can most easily be explained through the mechanics of the energy detector. As the observation window length (sometimes referred to as the integration time in the context of ED) increases, the ED captures an increasing amount of signal energy (assuming the signal is present), while averaging out the noise whose variance is already known to the detector. As Fig. 5.3 shows, this results in the narrowing of the PDFs of the decision statistic, which allows for easier discrimination between $\mathcal{H}_1$ and $\mathcal{H}_0$, and ultimately results in improved detection performance. For small values of N, both the AA-CU and AU-CU detectors have difficulty obtaining accurate channel estimates, which limits their detection performance to be similar to that of ED. This is seen in Fig. 5.4 which plots P_D vs. N for $K = 4$, $\text{SNR}_k = -20$ dB, and $P_{FA} = 0.01$ where both the purple (AA-CU) and red curves (AU-CU), which are virtually on top of one another, approach the gold curve (ED) when $N < 10^3$. From the same figure, it is apparent that while increasing N does improve detection performance, it does not influence the relative performance between alphabet-aware detectors and their alphabet-unaware counterparts.

Still operating in the low SNR regime, we shift our attention to detector performance as a function of the number of antennas K. As the number of antennas increases, the SNR available to the detector increases, which results in improved detection performance for all detectors considered. However, not all detectors reap equal performance gains from an increase in K. For instance, ED will underperform both AA and AU as K grows since ED does not utilize a coherent combining technique. This is evidenced by Fig. 5.5, which

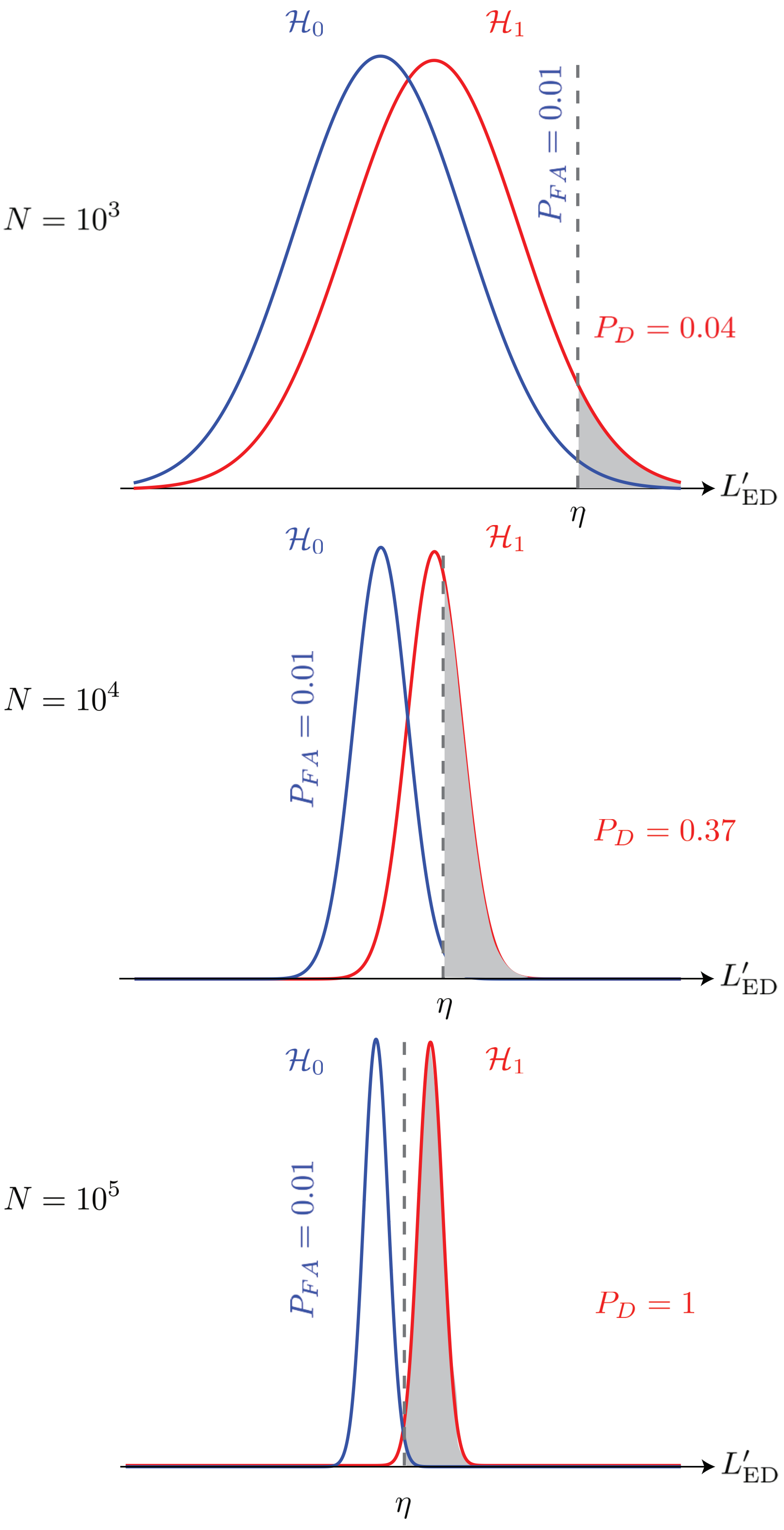

Figure 5.3: Probability density functions for $L'_{\text{ED}} = L_{\text{ED}}/2N$ under $\mathcal{H}_1$ (red curve) and $\mathcal{H}_0$ (blue curve) with $\text{SNR}_k = -20$ dB and $K = 4$. Central limit theorem applied to allow for normal distribution approximation of the PDFs.

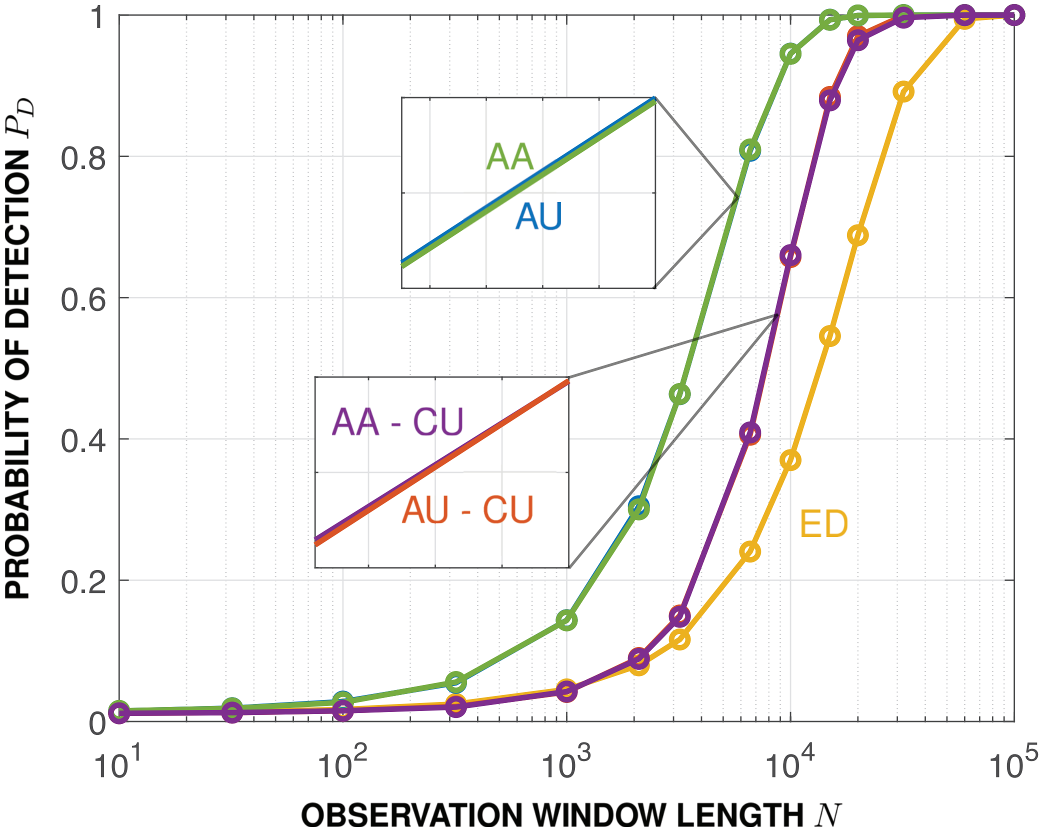

Figure 5.4: Probability of detection P_D vs. observation window length N for $K = 4$, $P_{FA} = 0.01$, and $\text{SNR}_k = -20$ dB. Inset plots are zoomed-in sections of the same set of curves.

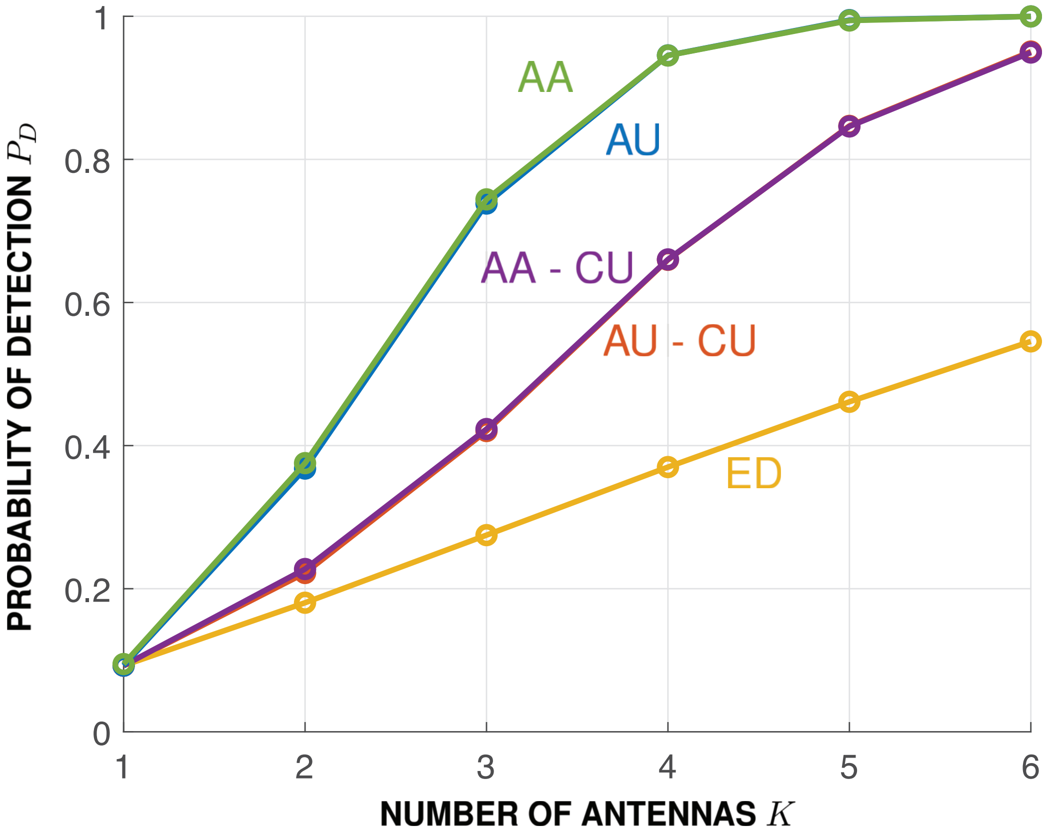

Figure 5.5: Probability of detection P_D vs. number of antennas K for $N = 10^4$, $P_{FA} = 0.01$, and SNR$_k = -20$ dB.

plots P_D vs. K for $N = 10^4$, SNR$_k = -20$ dB, and $P_{FA} = 0.01$. From this figure it is also apparent that the AA and AU (blue and green curves) are able to outperform their CU counterparts (purple and red curves) as both the AA and AU detectors have a priori knowledge of the channel gains and can flawlessly perform MRC.

The results in Fig. 5.5 suggest that while P_D improves with increasing K, at low SNR multiple antennas will not give an alphabet-aware detector a performance edge over its alphabet-unaware counterpart. This is evidenced by the consistent overlap of the AA and AU detection curves. Likewise, when these detectors are stripped of their a priori channel knowledge, the alphabet-aware advantage is still not apparent. Interestingly, when $K = 1$ all the detectors exhibit the same performance, as there is neither benefit from MRC, nor from alphabet awareness. In the following we show that the performance convergence of all detectors at $K = 1$ is to be expected, as in the limit of low SNR the performance of the single-antenna AA detector approaches that of the single-antenna ED. This statement holds regardless of the observation window length, and regardless of the false alarm rate.

Our approach is to show that, in the limit of low SNR and with a single antenna, the AA statistic has the same moment generating function (MGF) as the ED statistic, which indicates they have the same distribution, and therefore have the same performance. Since $K = 1$ we will temporarily suppress any k subscripts for readability. For mathematical convenience, we consider the adjusted AA statistic $Z = L_{\text{AA}} + N|\alpha|^2/\sigma^2$, which is simpler to work with and achieves the same performance (since it is equivalent to changing the threshold), namely:

$$\begin{aligned} Z &= \sum_{n=0}^{N-1} \log\left[\cosh\left(\frac{\text{Re}\{\alpha^* r(n)\}}{\sigma^2}\right)\cosh\left(\frac{\text{Im}\{\alpha^* r(n)\}}{\sigma^2}\right)\right] \\ &= \sum_{n=0}^{N-1} \log\big[\cosh\big(X(n)\big)\cosh\big(Y(n)\big)\big] \\ &= \sum_{n=0}^{2N-1} \log\big[\cosh\big(X(n)\big)\big], \end{aligned} \tag{5.21}$$

where the last line follows from the fact that $X(n) = \text{Re}\{\alpha^* r(n)\}/\sigma^2$ and $Y(n) = \text{Im}\{\alpha^* r(n)\}/\sigma^2$ have the same distribution under both $\mathcal{H}_1$ and $\mathcal{H}_0$. Under $\mathcal{H}_1$, both $X(n)$ and $Y(n)$ have probability density function (PDF) $0.5f(x-\rho)+0.5f(x+\rho)$, where $f(x)$ is the PDF of a normal random variable with zero mean and variance ρ, and where $\rho = \text{SNR}$. Under $\mathcal{H}_0$: $X(n) \sim \mathcal{N}(0, \rho)$, and $Y(n) \sim \mathcal{N}(0, \rho)$.

The MGF of Z is:

$$M_Z(\tau) = \prod_{n=0}^{2N-1} M_{Z(n)}(\tau) \tag{5.22}$$

where $Z(n) = \log\big[\cosh\big(X(n)\big)\big]$. From (5.22) it is apparent that we can calculate the MGF of $Z(n)$ and raise it to the $2N$th power since $\{X(n)\}$ are *i.i.d.*. First consider the case in which the real part of $s(n)$, $s_R(n)$, is 1:

$$\begin{aligned}
M_{Z(n)}(\tau|s_R(n)=1) &= \mathbb{E}\big[e^{\tau Z(n)}\big] \\
&= \mathbb{E}\big[\cosh(X(n))^{\tau}\big] \\
&= \mathbb{E}\bigg[\frac{e^{X(n)\tau}}{2^{\tau}}\sum_{k=0}^{\infty}\binom{\tau}{k}e^{-2X(n)k}\bigg] \\
&= \frac{1}{2^{\tau}}\sum_{k=0}^{\infty}\binom{\tau}{k}e^{\frac{\rho}{2}[4k^2-4k(1+\tau)+\tau(2+\tau)]} \qquad (5.23)\\
&= \frac{1}{2^{\tau}}\sum_{k=0}^{\infty}\binom{\tau}{k}e^{\frac{\rho}{2}\beta(\tau,k)} \\
&= \frac{1}{2^{\tau}}\sum_{k=0}^{\infty}\sum_{m=0}^{\infty}\binom{\tau}{k}\bigg(\frac{\rho^m\beta(\tau,k)^m}{2^m m!}\bigg),
\end{aligned}$$

where $\beta(\tau,k)=4k^2-4k(1+\tau)+\tau(2+\tau)$, and where $\binom{\tau}{k}=\tau(\tau-1)\ldots(\tau-k)(\tau-k+1)/k!$ is the generalized binomial coefficient for non-integer τ [158]. In the limit as $\rho\to 0$, terms of order $O(\rho^2)$ or higher can be ignored, which leads to:

$$\begin{aligned}
\lim_{\rho\to 0} M_{Z(n)}(\tau|s_R(n)=1) &= \frac{1}{2^{\tau}}\sum_{k=0}^{\infty}\binom{\tau}{k}\bigg(1+\frac{\rho\beta(\tau,k)}{2}\bigg) \\
&= 1+\frac{1}{2^{\tau}}\sum_{k=0}^{\infty}\binom{\tau}{k}\frac{\rho}{2}\big[4k^2 \qquad (5.24)\\
&\quad -4k(1+\tau)+\tau(2+\tau)\big] \\
&= 1+\frac{\rho\tau}{2}.
\end{aligned}$$

The case in which $s_R(n)=-1$ follows a similar derivation and leads to the same result: $\lim_{\rho\to 0} M_{Z(n)}(\tau|s_R(n)=-1)=\lim_{\rho\to 0} M_{Z(n)}(\tau|s_R(n)=1)=1+\rho\tau/2$.

Squaring (5.24), ignoring terms of $O(\rho^2)$ or higher, then raising the result to the Nth power yields:

$$\lim_{\rho\to 0} M_Z(\tau)=(1+\rho\tau)^N \qquad (5.25)$$

The MGF of Z under $\mathcal{H}_0$ is:

$$\begin{aligned} M_{Z(n)}(\tau) &= \mathbb{E}\big[e^{\tau Z(n)}\big] \\ &= \mathbb{E}\big[\cosh(X(n))^{\tau}\big] \\ &= \int_{-\infty}^{\infty} \frac{e^{-\frac{x^2}{2\rho}}}{\sqrt{2\pi\rho}} \left[\sum_{k=0}^{\infty} \binom{\tau}{k} \frac{e^{x(\tau-2k)}}{2^{\tau}}\right] dx \\ &= \frac{1}{2^{\tau}} \sum_{k=0}^{\infty} \binom{\tau}{k} e^{\frac{\rho}{2}(\tau-2k)^2} \\ &= \frac{1}{2^{\tau}} \sum_{k=0}^{\infty} \sum_{m=0}^{\infty} \binom{\tau}{k} \left(\frac{\rho^m(\tau-2k)^{2m}}{2^m m!}\right), \end{aligned} \tag{5.26}$$

where a binomial series was used to expand $\cosh(x)^{\tau}$ on the third line [158]. In the limit as $\rho \to 0$ terms of order $O(\rho^2)$ or higher will be small, and thus can be ignored. Using the following relationships:

$$\begin{aligned} 2^{\tau} &= \sum_{k=0}^{\infty} \binom{\tau}{k} \\ \tau 2^{(\tau-1)} &= \sum_{k=0}^{\infty} \binom{\tau}{k} k \\ \tau(\tau-1)2^{(\tau-2)} &= \sum_{k=0}^{\infty} \binom{\tau}{k} (k^2-k), \end{aligned}$$

we can compute:

$$\begin{aligned} \lim_{\rho\to 0} M_{Z(n)}(\tau) &= \frac{1}{2^{\tau}} \sum_{k=0}^{\infty} \binom{\tau}{k} \left(1 + \frac{\rho(\tau-2k)^2}{2}\right) \\ &= 1 + \frac{\rho\tau}{2}. \end{aligned} \tag{5.27}$$

In the limit as $\rho \to 0$, the MGF of $Z = \sum_{n=0}^{2N-1} Z(n)$ is:

$$\lim_{\rho\to 0} M_Z(\tau) = (1+\rho\tau)^N. \tag{5.28}$$

Interestingly, both (5.25) and (5.28) hold even when $K > 1$, since the distribution of (5.21) remains the same even in the multi-antenna case. This is because the AA detector can flawlessly perform MRC, which means the distributions of $X(n,K) = \sum_{k=0}^{K-1} \mathrm{Re}\{\alpha_k^* r_k(n)\}/\sigma^2$ and $Y(n,K) = \sum_{k=0}^{K-1} \mathrm{Im}\{\alpha_k^* r_k(n)\}/\sigma^2$ only depend on the total SNR $\rho = \sum_{k=0}^{K-1} \rho_k$. Despite this, neither (5.25) nor (5.28) can be used to predict the detection performance of the AA detector for non-zero ρ, and as (5.23) suggests we do not have a closed-form analytical expression for $M_Z(\tau)$.

We now consider the ED statistic ζ:

$$\zeta = \frac{\rho}{2\sigma^2} \sum_{n=0}^{N-1} |r(n)|^2 = \sum_{n=0}^{N-1} \zeta(n), \tag{5.29}$$

which is the same as (5.13) but with $K = 1$ and scaled by constant $\rho/2$ for mathematical convenience.

Under $\mathcal{H}_1$ the nth entry of (5.29) has a noncentral χ^2 distribution with 2 degrees of freedom and noncentrality parameter $\lambda = 2\rho$, scaled by constant $\rho/2$. Thus the MGF of $\zeta(n)$ is:

$$\begin{aligned} M_{\zeta(n)}(\tau) &= \mathbb{E}\left[e^{\tau\zeta(n)}\right] \\ &= \frac{e^{\frac{\rho^2\tau}{2(1-\rho\tau)}}}{(1-\rho\tau)} \\ &= \sum_{q=0}^{\infty} \frac{(\rho^2\tau)^q}{q!2^q(1-\rho\tau)^{q+1}} \end{aligned} \tag{5.30}$$

where the above expression is valid for $\tau < 1/\rho$ [165]. In the limit as $\rho \to 0$, terms of order $O(\rho^2)$ or higher can be ignored, yielding:

$$\lim_{\rho\to 0} M_{\zeta(n)}(\tau) = 1 + \rho\tau. \tag{5.31}$$

The MGF of ζ is $\prod_{n=0}^{N-1} M_{\zeta(n)}(\tau)$, which leads to:

$$\lim_{\rho \to 0} M_{\zeta}(\tau) = (1 + \rho\tau)^N. \tag{5.32}$$

We now consider the MGF of ζ under $\mathcal{H}_0$. Realizing $\zeta(n)$ is a χ^2 distribution with 2 degrees of freedom, scaled by constant $\rho/2$, the MGF is:

$$M_{\zeta(n)}(\tau) = \frac{1}{(1 - \rho\tau)}, \tag{5.33}$$

where the above expression is valid for $\tau < 1/\rho$ [165]. Applying a Taylor series with respect to ρ about 0 and ignoring terms of order $O(\rho^2)$ or higher yields $\lim_{\rho \to 0} M_{\zeta(n)}(\tau) = 1 + \rho\tau$. The MGF of ζ is then:

$$\lim_{\rho \to 0} M_{\zeta}(\tau) = (1 + \rho\tau)^N. \tag{5.34}$$

Since both (5.32) and (5.25), and (5.34) and (5.28), are identical, we have proven that Z and ζ have the same MGF in the limit as $\rho \to 0$, and thus have the same distribution under both $\mathcal{H}_1$ and $\mathcal{H}_0$.

Since, in the limit of low SNR, Z and ζ have the same MGF and thus the same distribution under both $\mathcal{H}_1$ and $\mathcal{H}_0$, the performance of the AA detector approaches the performance of an ED. This is consistent with the conclusions in [137, 29]. As this discussion has demonstrated, with a single antenna and knowledge of the channel gains, the advantage of knowing the signal alphabet disappears as SNR $\to 0$. Since the primary advantage of multiple antennas is MRC, an alphabet-aware advantage is still not apparent even when $K > 1$, as evidenced by the numerical results in Fig. 5.5.

5.4.2 The Alphabet-Aware Advantage

The AA detector can outperform the AU detector when the SNR is high and N is small. The high SNR allows the AA detector to recognize the signal constellation positions with minimal noise corruption, and exploit its knowledge of the signal alphabet for a performance advantage.

We now briefly discuss the influence of the observation window length N on detector performance. As Fig. 5.4 in the previous section has shown, at low SNR the value of N does not influence the relative performance of alphabet-aware detectors and their alphabet-unaware counterparts. At high SNRs, empirically, we have found that alphabet-aware detectors have the greatest performance gains over their alphabet-unaware counterparts when the observation window is small.

We can see the alphabet-aware advantage in Fig. 5.6 which plots P_D vs. SNR$_k$ with $K = 4$, $N = 5$, and $P_{FA} = 10^{-6}$. To accommodate for this reduced false alarm rate, the number of simulation trials was increased from $M = 10^5$ to $M = 10^7$. The AA (green curve) clearly outperforms its alphabet-unaware counterpart, the AU detector (blue curve). For example, in comparison to AA, the AU detector needs approximately 0.4 dB higher SNR$_k$ to obtain the same $P_D = 0.66$. Likewise, the AA-CU (purple curve) outperforms its alphabet unaware counterpart, the AU-CU detector (red curve) once the SNR is high. At high SNRs, the ED (gold curve) is significantly outperformed by the other four detectors.

When operating in the small N and high SNR regime, the alphabet-aware detectors have increasing performance gains over their alphabet-unaware counterpart as P_{FA} decreases. This can be seen in Fig. 5.7 which plots P_D vs. P_{FA} with SNR$_k$ $= 0$ dB for all five detectors. The performance gap between the AA and AU detectors (green and blue curves), as well their CU versions (purple and red curves), widens as P_{FA} decreases.

Our numerical results show that the proposed AA detector has performance benefits over its alphabet-unaware counterpart, the AU detector, when the observation window length N is small and the SNR is high. It has increasing performance gains over the AU

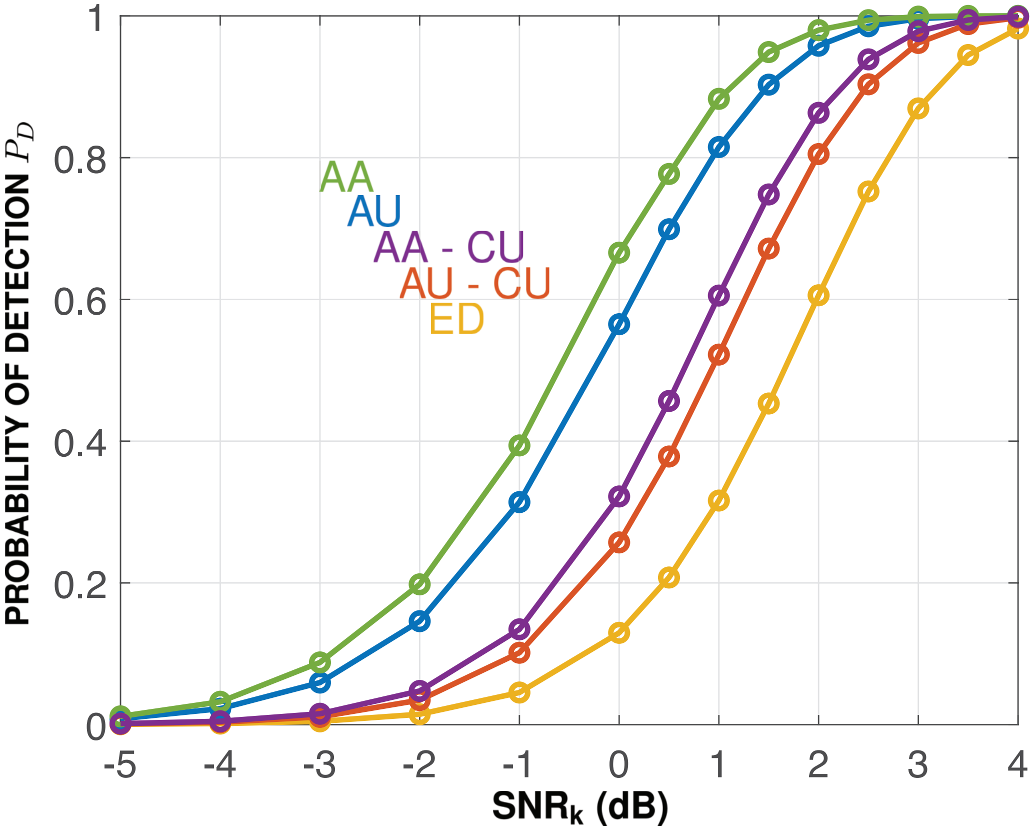

Figure 5.6: Probability of detection P_D vs. SNR$_k$ (dB) for $P_{FA} = 10^{-6}$, $N = 5$, and $K = 4$.

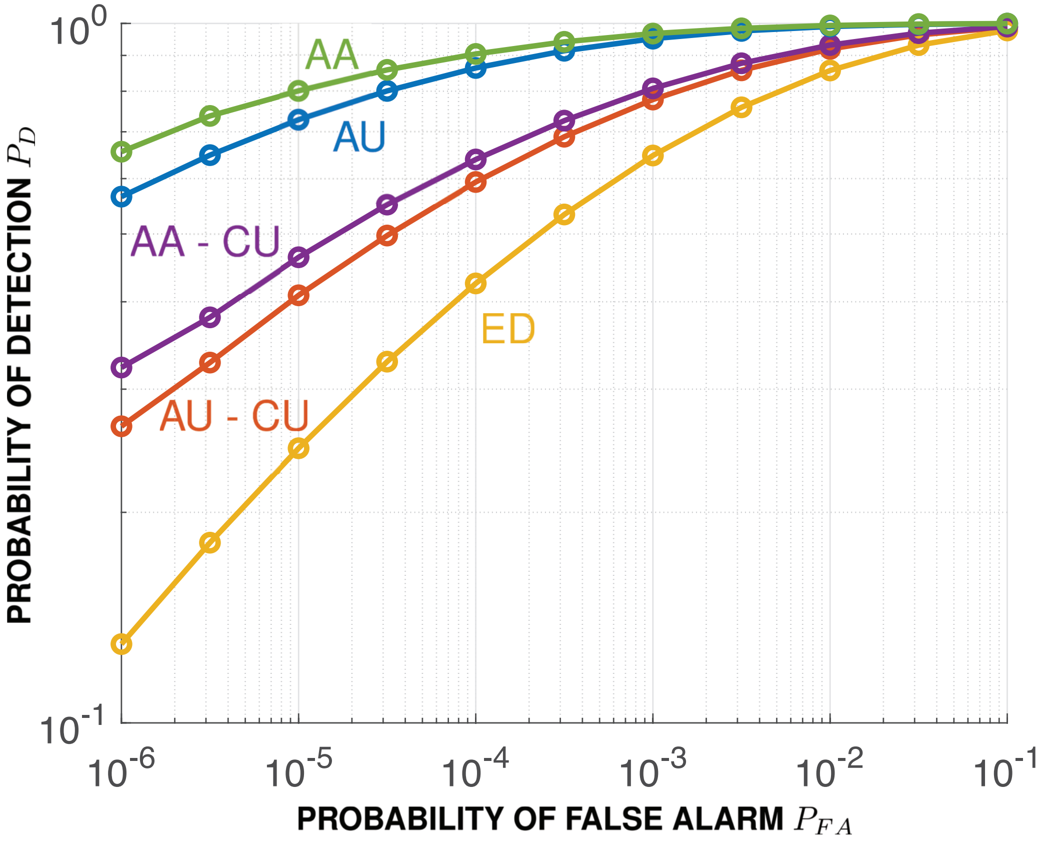

Figure 5.7: Probability of detection P_D vs. false alarm rate P_{FA} for $N = 5$, $\text{SNR}_k = 0$ dB, and $K = 4$.

detector as the false alarm rate P_{FA} decreases. The AA-CU and AU-CU detectors exhibit the same performance trends as well. Adjusting the number of antennas K does not affect the relative performance of alphabet-aware detectors over alphabet-unaware detectors.

Despite these performance gains, the AA detector has a higher computational complexity than the AU detector. We measure computational complexity as the number of operations needed to calculate a given decision statistic. If each complex add, complex multiply, and transcendental function computation is considered to be one operation, and if each conjugate transpose and memory load is assumed to be negligible, then the computational complexity of the AA detector is $\mathcal{O}(N(4K + 7))$, where $\mathcal{O}$ refers to the "Big O" notation. Using the same methodology, we can compute the computational complexity of ED, which is $\mathcal{O}(2NK)$, and the computational complexity of AU, which is $\mathcal{O}(N(2K + 1))$. From this analysis ED has lowest computational complexity of the three detectors, followed by the AU detector, and then the AA detector, which has the highest computational complexity.

The computational complexities of both the AA-CU and AU-CU detectors are less straightforward to characterize as both complexities are implementation dependent. The computational complexity of a P step gradient descent AA-CU is $\mathcal{O}(N(4K + 7) + 2K + P[K(4NK+16N]))$. The AU-CU detector as described in (5.20) is difficult to characterize as our methodology does not accommodate for computing the eigenvalues of a matrix. If we assume finding the maximum eigenvalue of a $K \times K$ matrix is $\mathcal{O}(K^3)$ [166, 167, 168], then AU-CU has computational complexity $\mathcal{O}(K^3 + N(K^2 + K))$. From these expressions it is clear that only when the number of antennas is large such that the K^3 term dominates does the AU-CU have greater complexity than AA-CU; this holds even if gradient descent were to converge in one step ($P = 1$). Thus for the channel-unaware detectors, in practical circumstances alphabet-awareness still results in a higher computational complexity. A summary of the detector complexities can be found in Table 5.1.

While the AA detector outperforms the AU detector when the SNR is high and N is

Table 5.1: Summary of Detector Computational Complexities

DETECTOR	**COMPLEXITY ORDER**
AA	$\mathcal{O}(N(4K+7)))$
AU	$\mathcal{O}(N(2K+1)))$
ED	$\mathcal{O}(2NK)$
AA-CU	$\mathcal{O}(N(4K+7)+2K+P[K(4NK+16N]))$
AU-CU	$\mathcal{O}(K^3+(N-0.5)(K^2+K))$

small, the performance gains are less than 1 dB even when the false alarm rate is small. Given the previous discussion, the AU detector has the advantage when computational resources are limited, or when a low false alarm rate is not required. At low SNR, we see a similar case against alphabet awareness, with the AA detector providing nearly indistinguishable performance from the AU detector. When considering the CU detectors the case is even more apparent, as both the AA-CU and AU-CU have similar performance at low SNR, and in the case of small N both can actually be outperformed by the simpler ED.

5.5 Summary

In this chapter we have proposed a LRT detector that can detect long-code DSSS signals with QPSK coded chips, whose has computational complexity grows linearly with observation window length, and that can take advantage of multiple antennas. We have compared the performance of this proposed detector against other multi-antenna alphabet unaware detectors, and only under the specific conditions of high SNR, small observation window length, and low false alarm rate does knowledge of the signal alphabet provide a measurable advantage. For noncooperative DSSS signal detection at low SNR, knowledge of QPSK coded chips cannot be leveraged to significantly improve detection performance.

CHAPTER 6

CONCLUSION AND SUGGESTED FUTURE WORK

In this thesis we have explored two key communication problems that are expected to be present on the modern battlefield: DSSS acquisition in high dynamic environments, and noncooperative DSSS signal detection. Both are motivated by the use of long spreading codes in military communications, with the former also drawing its roots from hypersonic aircraft communication, and LEO satellite communication.

In the case of DSSS acquisition we have proposed delay-Doppler efficient exhaustive search (DEES), an algorithm that can acquire long-code DSSS signals in the face of both time-varying channel delays and time-varying Doppler frequency shifts. DEES utilizes a composition of second-order keystone-transforms and the fractional Fourier transform to remove time-varying channel effects, before utilizing an efficient FFT-based algorithm derived from the optimal 2D exhaustive search to acquire the post-processed signal. The advantage of this post-processing method is it utilizes the fractional Fourier transform to efficiently search over the Doppler rate, and avoids the high complexity associated with the optimal 3D exhaustive search. Simulation results show this composition of transforms are effective in mitigating the high dynamic effects of the channel, as DEES provides superior acquisition performance to its core DEES sibling in the LEO satellite channel.

While the DEES algorithm is suitable for performing acquisition in environments characterized by both time-varying Doppler and time-varying channel delays, there are still many improvements that could be made to the algorithm. First, as presented in this thesis DEES can only handle a multipath channel environment if each channel path experiences the same Doppler rate. While this may hold in the AtS channel when the aircraft is far away from the ship, it certainly does not hold in others. Therefore, we consider the augmentation of DEES to accommodate for those situations. Given the parallels between the estimation portion of DSSS acquisition and target detection in radar signal processing, it would be interesting to see if the CLEAN algorithm [101, 152, 169] could be modified for this purpose. Second, the second-order keystone-transform and fractional Fourier transform augmentations for core DEES (that resulted in DEES) were derived under the assumption that fading effects were absent from the channel. It would be interesting to see how DEES performs in a channel with Rician fading, as this is a more accurate characterization of the LEO satellite channel, and if performance does suffer with this adjustment, what improvements could be made to DEES. Lastly, while the fractional Fourier transform can be used to estimate the Doppler rate, in the case of DEES it provides less than satisfactory performance at low SNR. It would be interesting to see what other improvements could be made to the DEES algorithm to improve Doppler rate estimates.

In the case of noncooperative DSSS detection, we have proposed a LRT detector that can take advantage of multiple antennas, exploits knowledge that the signal alphabet is QPSK, and has computational complexity that grows linearly with observation window length. Our results have shown that despite the proposed detector's knowledge of the signal alphabet, at low SNR it provides comparable performance to its alphabet-unaware counterpart, regardless of the observation window length, and regardless of the number of antennas. Only under the specific conditions of high SNR, small observation window length, and low false alarm rate does knowledge of the signal alphabet provide a measurable advantage. In nearly all situations considered, either the multi-antenna alphabet-unaware detector or the energy detector provided similar detection performance as the alphabet-aware detector, but with lower computational complexity.

Although we have established the lack of an alphabet-aware advantage in detecting DSSS signals with QPSK coded chips, the received signal models in Chapter 5 did not accommodate for either fading effects or synchronization mismatch. While these assumptions are useful in directly measuring the benefits of alphabet awareness, they are incredibly idealistic to say the least. It would be interesting to see if the lack of an alphabet-aware advantage in the noncooperative detection of DSSS signals still holds when a fading channel model is considered, along with a time-varying phase term that models the carrier frequency offset. This thesis has shown, in the case where the channel effects are modeled as a complex channel gain, the optimal solution is to perform maximal-ratio combining on the received signal vectors at each antenna, which effectively boosts the SNR at the detector. It would be interesting to see how the detector decision statistic changes under these proposed channel model adjustments. In addition to changes to the channel model, another interesting direction would be to add interference to the received signal model. It is unlikely that a detector deployed on a battlefield will only collect its target signal of interest, and there are likely other communication signals, possibly friendly, that will make its detection task more difficult.

Appendices

APPENDIX A

BAYESIAN APPROACH TO DERIVING ALPHABET-AWARE CHANNEL-UNAWARE DETECTOR

In this Appendix we derive the alphabet-aware channel-unaware (AA-CU) decision statistic assuming that the magnitude of the channel gains $|\alpha_k|$ are known to the detector, and the phases of each of the channel gains are uniformly distributed, i.e. $\theta_k \sim \mathcal{U}(-\pi, \pi)$.

Under these conditions the PDF of $\mathbf{r}$ under $\mathcal{H}_1$ can be expressed as:

$$\begin{aligned} f(\mathbf{R}|\mathcal{H}_1) &= \mathbb{E}_\theta\Bigg[\mathbb{E}_{\mathbf{s}}\Bigg[\left(\frac{1}{2\pi\sigma^2}\right)^{NK} e^{-\sum_{k=0}^{K-1} \frac{||\mathbf{r}_k - |\alpha_k| e^{j\theta_k}\mathbf{s}||^2}{2\sigma^2}}\Bigg]\Bigg] \\ &= \mathbb{E}_\theta\Bigg[\left(\frac{1}{2\pi\sigma^2}\right)^{NK} e^{-\sum_{k=0}^{K-1} \frac{(||\mathbf{r}_k||^2 + N|\alpha_k|^2)}{2\sigma^2}} \frac{1}{2^{2N}} \sum_{i=1}^{2^{2N}} e^{\sum_{k=0}^{K-1} \frac{\mathrm{Re}\{|\alpha_k| e^{-j\theta_k}\mathbf{s}_i^\dagger \mathbf{r}_k\}}{\sigma^2}}\Bigg] \\ &= \left(\frac{1}{2\pi\sigma^2}\right)^{NK} e^{-\sum_{k=0}^{K-1} \frac{(||\mathbf{r}_k||^2 + N|\alpha_k|^2)}{2\sigma^2}} \left(\frac{1}{2\pi}\right)^{K} \int_{-\pi}^{\pi}\int_{-\pi}^{\pi}\cdots\int_{-\pi}^{\pi} \prod_{n=0}^{N-1} \\ &\quad \cosh\left(\sum_{k=0}^{K-1} \frac{\mathrm{Re}\{|\alpha_k| e^{-j\theta_k} r_k(n)\}}{\sigma^2}\right) \cosh\left(\sum_{k=0}^{K-1} \frac{\mathrm{Im}\{|\alpha_k| e^{-j\theta_k} r_k(n)\}}{\sigma^2}\right) d\theta_0 d\theta_1 \ldots d\theta_{K-1}. \end{aligned} \tag{A.1}$$

The PDF of $\mathbf{R}$ under $\mathcal{H}_0$ can be expressed as:

$$f(\mathbf{R}|\mathcal{H}_0) = \left(\frac{1}{2\pi\sigma^2}\right)^{NK} e^{\sum_{k=0}^{K-1} \frac{-||\mathbf{r}_k||^2}{2\sigma^2}} \tag{A.2}$$

Forming the likelihood ratio yields the decision statistic:

$$\begin{aligned} \mathcal{L} = \log\Bigg[\left(\frac{1}{2\pi}\right)^{K} \int_{-\pi}^{\pi}\int_{-\pi}^{\pi}\cdots\int_{-\pi}^{\pi} \prod_{n=0}^{N-1} \cosh\left(\sum_{k=0}^{K-1} \frac{\mathrm{Re}\{|\alpha_k| e^{-j\theta_k} r_k(n)\}}{\sigma^2}\right) d\theta_0 d\theta_1 \ldots d\theta_{K-1}\Bigg] \\ - \sum_{k=0}^{K-1} \frac{N|\alpha_k|^2}{\sigma^2}. \end{aligned} \tag{A.3}$$

As is apparent from (A.3), this approach has resulted in a K dimensional integral which has no closed-form analytical solution.

A different, but mathematically equivalent, result can be obtained by changing the order of the expectations in (A.1).

$$\begin{aligned} f(\mathbf{R}|\mathcal{H}_1) &= \mathbb{E}_{\mathbf{s}}\left[\mathbb{E}_{\theta}\left[\left(\frac{1}{2\pi\sigma^2}\right)^{NK} e^{-\sum_{k=0}^{K-1}\frac{||\mathbf{r}_k-|\alpha_k|e^{j\theta_k}\mathbf{s}||^2}{2\sigma^2}}\right]\right] \\ &= \mathbb{E}_{\mathbf{s}}\left[\left(\frac{1}{2\pi\sigma^2}\right)^{NK} e^{-\sum_{k=0}^{K-1}\frac{(||\mathbf{r}_k||^2+N|\alpha_k|^2)}{2\sigma^2}}\mathbb{E}_{\theta}\left[e^{\sum_{k=0}^{K-1}\frac{|\alpha_k||\mathbf{s}^\dagger\mathbf{r}_k|\cos(\theta_k)}{\sigma^2}}\right]\right] \\ &= \mathbb{E}_{\mathbf{s}}\left[\left(\frac{1}{2\pi\sigma^2}\right)^{NK} e^{-\sum_{k=0}^{K-1}\frac{(||\mathbf{r}_k||^2+N|\alpha_k|^2)}{2\sigma^2}}\prod_{k=0}^{K-1} I_0\left(\frac{|\alpha_k||\mathbf{s}^\dagger\mathbf{r}_k|}{\sigma^2}\right)\right] \\ &= \left(\frac{1}{2\pi\sigma^2}\right)^{NK} e^{-\sum_{k=0}^{K-1}\frac{(||\mathbf{r}_k||^2+N|\alpha_k|^2)}{2\sigma^2}}\left[\frac{1}{2^{2N}}\sum_{i=1}^{2^{2N}}\prod_{k=0}^{K-1} I_0\left(\frac{|\alpha_k||\mathbf{s}_i^\dagger\mathbf{r}_k|}{\sigma^2}\right)\right], \end{aligned} \tag{A.4}$$

where $I_0(x)$ is the modified Bessel function of the first kind.

The decision statistic is then:

$$\mathcal{L} = \log\left(\frac{f(\mathbf{R}|\mathcal{H}_1)}{f(\mathbf{R}|\mathcal{H}_0)}\right) = \log\left[\frac{1}{2^{2N}}\sum_{i=1}^{2^{2N}}\prod_{k=0}^{K-1} I_0\left(\frac{|\alpha_k||\mathbf{s}_i^\dagger\mathbf{r}_k|}{\sigma^2}\right)\right] - \sum_{k=0}^{K-1}\frac{N|\alpha_k|^2}{\sigma^2}. \tag{A.5}$$

In comparison to (A.3), (A.5) no longer has a K dimensional integral and can be implemented numerically. However, due to the presence of the 2^{2N} sum terms, (A.5) has high computational complexity and is not practical for even modest values of N. Furthermore, unlike (5.16), the presence of the modified Bessel function $I_0(x)$ prevents the logcosh reduction.

APPENDIX B

GRADIENT DESCENT EQUATIONS FOR ALPHABET-AWARE CHANNEL-UNAWARE DETECTOR

In this Appendix we calculate the gradient descent equations for the alphabet-aware channel-unaware (AA-CU) detector described in (5.3). Separating the real and imaginary components of the received signal vector and the channel gains for mathematical convenience, the log PDF under $\mathcal{H}_1$ is:

$$\begin{aligned}\log\bigl(f(\mathbf{R}_{\mathrm{R}},\mathbf{R}_{\mathrm{I}}|\mathcal{H}_1)\bigr) = &-\sum_{k=0}^{K-1}\frac{1}{2\sigma^2}[||\mathbf{r}_{k,\mathrm{R}}||^2+||\mathbf{r}_{k,\mathrm{I}}||^2+2N(\alpha_{k,\mathrm{R}}^2+\alpha_{k,\mathrm{I}}^2)] \\ &+\sum_{n=0}^{N-1}\log\Biggl[\cosh\Biggl(\frac{1}{\sigma^2}\sum_{k=0}^{K-1}\alpha_{k,\mathrm{R}}r_{k,\mathrm{R}}(n)+\alpha_{k,\mathrm{I}}r_{k,\mathrm{I}}(n)\Biggr) \\ &\qquad\cosh\Biggl(\frac{1}{\sigma^2}\sum_{k=0}^{K-1}\alpha_{k,\mathrm{I}}r_{k,\mathrm{R}}(n)-\alpha_{k,\mathrm{R}}r_{k,\mathrm{I}}(n)\Biggr)\Biggr]-NK\log(2\pi\sigma^2)\end{aligned} \tag{B.1}$$

where $\mathbf{r}_{k,\mathrm{R}}$, $\mathbf{r}_{k,\mathrm{I}}$ refer to the real and imaginary parts of $\mathbf{r}_k$, respectively, and $\alpha_{k,\mathrm{R}}$, $\alpha_{k,\mathrm{I}}$ refer to the real and imaginary parts of α_k.

Taking the partial derivative with respect to $\alpha_{k,\mathrm{R}}$ yields:

$$\begin{aligned}\frac{\partial\log\bigl(f(\mathbf{R}_{\mathrm{R}},\mathbf{R}_{\mathrm{I}}|\mathcal{H}_1)\bigr)}{\alpha_{k,\mathrm{R}}} = &\sum_{n=0}^{N-1}\Biggl[\tanh\Biggl(\sum_{k=0}^{K-1}\frac{\alpha_{k,\mathrm{R}}r_{k,\mathrm{R}}(n)+\alpha_{k,\mathrm{I}}r_{k,\mathrm{I}}(n)}{\sigma^2}\Biggr)\frac{r_{k,\mathrm{R}}(n)}{\sigma^2} \\ &+\tanh\Biggl(\sum_{k=0}^{K-1}\frac{\alpha_{k,\mathrm{I}}r_{k,\mathrm{R}}(n)-\alpha_{k,\mathrm{R}}r_{k,\mathrm{I}}(n)}{\sigma^2}\Biggr)\frac{r_{k,\mathrm{I}}(n)}{\sigma^2}\Biggr]-\frac{2N\alpha_{k,\mathrm{R}}}{\sigma^2}\end{aligned} \tag{B.2}$$

Taking the partial derivative with respect to $\alpha_{k,\mathrm{I}}$ yields:

$$\frac{\partial \log\big(f(\mathbf{R}_\mathrm{R},\mathbf{R}_\mathrm{I}|\mathcal{H}_1)\big)}{\alpha_{k,\mathrm{I}}} = \sum_{n=0}^{N-1}\Bigg[\tanh\Bigg(\sum_{k=0}^{K-1}\frac{\alpha_{k,\mathrm{R}}r_{k,\mathrm{R}}(n)+\alpha_{k,\mathrm{I}}r_{k,\mathrm{I}}(n)}{\sigma^2}\Bigg)\frac{r_{k,\mathrm{I}}(n)}{\sigma^2} - \tanh\Bigg(\sum_{k=0}^{K-1}\frac{\alpha_{k,\mathrm{I}}r_{k,\mathrm{R}}(n)-\alpha_{k,\mathrm{R}}r_{k,\mathrm{I}}(n)}{\sigma^2}\Bigg)\frac{r_{k,\mathrm{R}}(n)}{\sigma^2}\Bigg] - \frac{2N\alpha_{k,\mathrm{I}}}{\sigma^2} \tag{B.3}$$

The gradient of $L = \log\big(f(\mathbf{R}_\mathrm{R},\mathbf{R}_I|\mathcal{H}_1)\big)$ can then be expressed as:

$$\nabla L = \begin{bmatrix} \frac{\partial L}{\partial \alpha_{0,\mathrm{R}}} \\ \frac{\partial L}{\partial \alpha_{0,\mathrm{I}}} \\ \frac{\partial L}{\partial \alpha_{1,\mathrm{R}}} \\ \frac{\partial L}{\partial \alpha_{1,\mathrm{I}}} \\ \vdots \\ \frac{\partial L}{\partial \alpha_{K-1,\mathrm{R}}} \\ \frac{\partial L}{\partial \alpha_{K-1,\mathrm{I}}} \end{bmatrix} \tag{B.4}$$

The update equation of gradient descent is given by:

$$\mathbf{x}_{p+1} = \mathbf{x}_p - \gamma_p \nabla L(\mathbf{x}_p) \tag{B.5}$$

where x_p is vector of input values at the pth step, γ_p is the step size, ∇ is the gradient operator, and L is function of interest. The step size γ_p can be calculated:

$$\gamma_p = \frac{|(\mathbf{x}_p - \mathbf{x}_{p-1})^\mathrm{T}[\nabla L(\mathbf{x}_p) - \nabla L(\mathbf{x}_{p-1})]|}{||\nabla L(\mathbf{x}_p) - \nabla Y(\mathbf{x}_{p-1})||^2}. \tag{B.6}$$

The equations update iteratively until a convergence criteria met. One possible criteria is if the step size γ_p is smaller than a certain value.

APPENDIX C

PDFS OF SELECT FUNCTIONS OF RANDOM VARIABLES

C.1 PDF of Cosh of a Normal R.V.

We begin with a derivation of the probability density function (PDF) of $Y = \cosh[X]$ where $X \sim \mathcal{N}(\mu, \sigma^2)$, $\mu, \sigma \in \mathcal{R}$, and $\sigma > 0$. We use the cumulative distribution function (CDF) to derive the PDF of Y:

$$\begin{aligned} \mathcal{F}_Y(y) &= P[Y \leq y] \\ &= P[\cosh(X) \leq y] \\ &= P[X \leq \cosh^{-1}(y)] + P[X \geq -\cosh^{-1}(y)] \\ &= \mathcal{F}_X(\cosh^{-1}(y)) + 1 - \mathcal{F}_X(-\cosh^{-1}(y)) \end{aligned} \tag{C.1}$$

where $\mathcal{F}_Y(y)$ and $\mathcal{F}_X(x)$ refer to the CDFs of Y and X, respectively, and where:

$$\mathcal{F}_X(x) = \frac{1}{2}\left[1 + \text{erf}\left(\frac{x - \mu}{\sqrt{2\sigma^2}}\right)\right], \tag{C.2}$$

where $\text{erf}(x) = 2/\sqrt{\pi}\int_0^x e^{-t^2}dt$. We can obtain the PDF of Y, $f_Y(y)$, by taking the derivative of $\mathcal{F}_Y(y)$. Doing this yields:

$$f_Y(y) = \begin{cases} \frac{2}{\sqrt{2\pi\sigma^2}}\frac{1}{\sqrt{y^2-1}}e^{-\frac{(\mu^2+(\cosh^{-1}(y))^2)}{2\sigma^2}}\cosh\left(\frac{\mu}{\sigma^2}\cosh^{-1}(y)\right) & y \geq 1 \\ 0 & \text{otherwise} \end{cases} \tag{C.3}$$

The mean and the variance can be easily calculated by applying the law of the unconscious statistician (LOTUS). The mean is:

$$\begin{aligned}\mathbb{E}[Y] &= \int_{-\infty}^{\infty} \cosh(x) \frac{1}{\sqrt{2\pi\sigma^2}} e^{-\frac{(x-\mu)^2}{2\sigma^2}} dx \\ &= e^{\frac{\sigma^2}{2}} \cosh(\mu).\end{aligned} \tag{C.4}$$

The variance can be obtained in a similar fashion.

$$\text{Var}[Y] = \frac{1}{2}\big(1 + e^{2\sigma^2}\cosh(2\mu)\big) - e^{\sigma^2}\cosh(\mu)^2. \tag{C.5}$$

The author is unaware of any closed form solution for the moment generating function (MGF) of Y.

C.2 Distribution of Log Cosh of a Normal R.V.

In this section we derive the PDF of $Z = \log[Y] = \cosh[X]$ where $X \sim \mathcal{N}(\mu, \sigma^2)$, $\mu, \sigma \in \mathcal{R}$, and $\sigma > 0$. We use the CDF to derive the PDF of Z:

$$\begin{aligned}\mathcal{F}_Z(z) &= P[Z \leq z] \\ &= P[\log(Y) \leq z] \\ &= \mathcal{F}_Y(\exp(z)) \\ &= \frac{1}{2}\left(2 - \text{erf}\left[\frac{\mu - \cosh^{-1}(e^z)}{\sqrt{2\sigma^2}}\right] + \text{erf}\left[\frac{\mu + \cosh^{-1}(e^z)}{\sqrt{2\sigma^2}}\right]\right)\end{aligned} \tag{C.6}$$

where $\mathcal{F}_Z(z)$ and $\mathcal{F}_Y(y)$ refer to the CDFs of Z and Y, respectively. $\mathcal{F}_Y(y)$ was derived in the previous section. Taking the derivative of $\mathcal{F}_Z(z)$ with respect to z yields the PDF:

$$f_Z(z) = \begin{cases} \frac{\cosh\left(\frac{\mu}{\sigma^2}\cosh^{-1}(e^z)\right)}{\sqrt{\pi\sigma^2}\sqrt{e^z\sinh(z)}} e^{z - \frac{1}{2\sigma^2}(\mu^2 + (\cosh^{-1}(e^z))^2)} & z > 0 \\ 0 & \text{otherwise} \end{cases} \tag{C.7}$$

The author is unaware of a closed form solution for either the mean or the variance. The expected value cannot be obtained from LOTUS, since the $\log(\cosh(x))$ term cannot be integrated, and subsequently the variance cannot be determined either.

REFERENCES

[1] A. Finlan, “The shape of warfare to come: A swedish perspective 2020–2045,” *Defense & Security Analysis*, vol. 37, no. 4, pp. 472–491, Oct. 2021.

[2] D. Sziroczak and H. Smith, “A review of design issues specific to hypersonic flight vehicles,” *Progress in Aerospace Sciences*, vol. 84, pp. 1–28, Jul. 2016.

[3] I. Oelrich, “Cool your jets: Some perspective on the hyping of hypersonic weapons,” *Bulletin of the Atomic Scientists*, vol. 76, no. 1, pp. 37–45, Jan. 2020.

[4] D. Wilkening, “Hypersonic weapons and strategic stability,” *Survival*, vol. 61, no. 5, pp. 129–148, Sep. 2019.

[5] D. M. Van Wie, S. M. D’Alessio, and M. E. White, “Hypersonic airbreathing propulsion,” *Johns Hopkins APL technical digest*, vol. 26, no. 4, pp. 430–437, 2005.

[6] J. Njuguna, *Lightweight composite structures in transport : design, manufacturing, analysis and performance*. Oxford: Woodhead Publishing, 2016, ISBN: 978-1782423256.

[7] H. Taguchi *et al.*, “Research on hypersonic aircraft using pre-cooled turbojet engines,” *Acta Astronautica*, vol. 73, pp. 164–172, Apr. 2012.

[8] M. Tang and R. Chase, “The quest for hypersonic flight with air-breathing propulsion,” in *15th AIAA International Space Planes and Hypersonic Systems and Technologies Conference*, American Institute of Aeronautics and Astronautics, Apr. 2008.

[9] Z. Niu, T. Su, and J. Zheng, “Target detection algorithm for hypersonic vehicle based on wideband radar echo model,” *IEEE Access*, vol. 7, pp. 7678–7690, 2019.

[10] M. S. Vassiliou, J. R. Agre, S. Shah, and T. MacDonald, “Crucial differences between commercial and military communications technology needs: Why the military still needs its own research,” in *MILCOM 2013 - 2013 IEEE Military Communications Conference*, IEEE, Nov. 2013.

[11] C. Wang, Z. Zhang, J. Wu, C. Chen, and F. Gao, “An overview of protected satellite communications in intelligent age,” *Science China Information Sciences*, vol. 64, no. 6, May 2021.

[12] Y. Lee and J. P. Choi, “Performance evaluation of high-frequency mobile satellite communications,” *IEEE Access*, vol. 7, pp. 49 077–49 087, 2019.

[13] M. E. Ray *et al.*, “Tactical ka-band MIL-SATCOM using LEO small satellites,” in *2017 IEEE MTT-S International Microwave Symposium (IMS)*, IEEE, Jun. 2017.

[14] K.-X. Li *et al.*, “Downlink transmit design for massive MIMO LEO satellite communications,” *IEEE Transactions on Communications*, pp. 1–1, 2021.

[15] S. Liu *et al.*, *Leo satellite constellations for 5g and beyond: How will they reshape vertical domains?* 2021. arXiv: 2106.09897 `[eess.SP]`.

[16] E. Meng, X. Bu, and C. Wang, “A novel anti-interception waveform in LEO satellite system,” in *2020 IEEE 4th Information Technology, Networking, Electronic and Automation Control Conference (ITNEC)*, IEEE, Jun. 2020.

[17] I. Leyva-Mayorga *et al.*, “LEO small-satellite constellations for 5g and beyond-5g communications,” *IEEE Access*, vol. 8, pp. 184 955–184 964, 2020.

[18] I. Ali, N. Al-Dhahir, and J. Hershey, “Doppler characterization for LEO satellites,” *IEEE Transactions on Communications*, vol. 46, no. 3, pp. 309–313, Mar. 1998.

[19] S. Glisic, R. Pickholtz, and W. Wu, “Issues in CDMA applications for mobile LEO satellite communications,” in *Proceedings of ISSSTA'95 International Symposium on Spread Spectrum Techniques and Applications*, IEEE.

[20] M. Lucente *et al.*, “Experimental missions in W-band: A small leo satellite approach,” *IEEE Systems Journal*, vol. 2, no. 1, pp. 90–103, Mar. 2008.

[21] T. Pratt, *Satellite communications*. Hoboken, NJ, USA: Wiley, 2020, ISBN: 978-1-119-48205-5.

[22] Y. Zhang, Y. Wu, A. Liu, X. Xia, T. Pan, and X. Liu, “Deep learning-based channel prediction for LEO satellite massive MIMO communication system,” *IEEE Wireless Communications Letters*, vol. 10, no. 8, pp. 1835–1839, Aug. 2021.

[23] L. Shi, L. Zhao, C. Zhang, and B. Yao, “Fast telemetry and communication scheme based on doppler diversity reception under large dynamic doppler for hypersonic vehicles,” *Electronics*, vol. 8, no. 7, 2019.

[24] L. You, K.-X. Li, J. Wang, X. Gao, X.-G. Xia, and B. Otterstenx, “LEO satellite communications with massive MIMO,” in *ICC 2020 - 2020 IEEE International Conference on Communications (ICC)*, IEEE, Jun. 2020.

[25] L. You, K.-X. Li, J. Wang, X. Gao, X.-G. Xia, and B. Ottersten, “Massive MIMO transmission for LEO satellite communications,” *IEEE Journal on Selected Areas in Communications*, vol. 38, no. 8, pp. 1851–1865, Aug. 2020.

[26] O. Kodheli *et al.*, "Satellite communications in the new space era: A survey and future challenges," *IEEE Communications Surveys & Tutorials*, vol. 23, no. 1, pp. 70–109, 2021.

[27] J. Chu, X. Chen, C. Zhong, and Z. Zhang, "Robust design for NOMA-based multibeam LEO satellite internet of things," *IEEE Internet of Things Journal*, vol. 8, no. 3, pp. 1959–1970, Feb. 2021.

[28] D. Torrieri, *Principles of Spread-Spectrum Communication Systems*, 3rd. Springer Publishing Company, Incorporated, 2015, ISBN: 3319140957.

[29] M. Simon *et al.*, *Spread Spectrum Communications Handbook*. New York: McGraw-Hill, Sep. 2001, p. 1248, ISBN: 978-0071382151.

[30] L.Simone, G.Fitlipaldi, and I. Aguilar Sanchez, "Fast acquisition techniques for very long pn codes for on-board secure ttc transponders," IEEE, 2011, pp. 1748–1753.

[31] P. Beckmann, *The Scattering of Electromagnetic Waves from Rough Surfaces (Artech House Radar Library)*. Artech Print on Demand, Mar. 1987, ISBN: 0890062382.

[32] Z. Xu, X. Dong, and J. Bornemann, "A statistical model for the MIMO channel with rough reflection surfaces in the THz band," *Nano Communication Networks*, vol. 8, pp. 25–34, Jun. 2016.

[33] S. Priebe, M. Jacob, C. Jansen, and T. Kürner, "Non-specular scattering modeling for thz propagation simulations," in *Proceedings of the 5th European Conference on Antennas and Propagation (EUCAP)*, 2011, pp. 1–5.

[34] A. Moldovan, M. A. Ruder, I. F. Akyildiz, and W. H. Gerstacker, "LOS and NLOS channel modeling for terahertz wireless communication with scattered rays," in *2014 IEEE Globecom Workshops (GC Wkshps)*, IEEE, Dec. 2014.

[35] R. Mital and V. Gregers-Hansen, "A computer model for bistatic sea surface microwave reflectivity," Washington, DC, Tech. Rep., 2014.

[36] Q. Lei and M. Rice, "Multipath channel model for over-water aeronautical telemetry," *IEEE Transactions on Aerospace and Electronic Systems*, vol. 45, no. 2, pp. 735–742, Apr. 2009.

[37] D. W. Matolak and R. Sun, "Air–ground channel characterization for unmanned aircraft systems—part i: Methods, measurements, and models for over-water settings," *IEEE Transactions on Vehicular Technology*, vol. 66, no. 1, pp. 26–44, Jan. 2017.

[38] F. Huang, X. Liao, and Y. Bai, “Multipath channel model for radio propagation over sea surface,” *Wireless Pers Commun*, vol. 90, no. 1, pp. 245–257, May 2016.

[39] M. Marom, “Effects of irregular sea surface and evaporation duct on radar detection performance,” M.S. thesis, Naval Postgraduate School, Jun. 1988.

[40] C. Balanis, *Advanced engineering electromagnetics*. Hoboken, N.J: John Wiley & Sons, 2012, ISBN: 0470589485.

[41] F. Ulaby, *Fundamentals of applied electromagnetics*. Boston: Pearson, 2015, ISBN: 1292082445.

[42] J. Richter, “Radio wave propagation modeling,prediction and assessment,” San Diego,CA, Tech. Rep., 1990.

[43] A. Miller, R. Brown, and E. Vegh, “New derivation for the rough-surface reflection coefficient and for the distribution of sea-wave elevations,” *IEE Proceedings H Microwaves, Optics and Antennas*, vol. 131, no. 2, p. 114, 1984.

[44] L. Barclay, Ed., *Propagation of Radiowaves*. Institution of Engineering and Technology, Jan. 2003.

[45] L. Yee Hui, F. Dong, and Y. S. Meng, “Near sea-surface mobile radiowave propagation at 5 ghz: Measurements and modeling,” *Radioengineering*, vol. 23, no. 3, pp. 824–830, 2014.

[46] X. Cao and T. Jiang, “Research on sea surface ka-band stochastic multipath channel modeling,” in *Proceedings of 2014 3rd Asia-Pacific Conference on Antennas and Propagation*, IEEE, Jul. 2014.

[47] R. Sun and D. W. Matolak, “Over-harbor channel modeling with directional ground station antennas for the air-ground channel,” in *2014 IEEE Military Communications Conference*, IEEE, Oct. 2014.

[48] Y. S. Meng and Y. H. Lee, “Measurements and characterizations of air-to-ground channel over sea surface at c-band with low airborne altitudes,” *IEEE Transactions on Vehicular Technology*, vol. 60, no. 4, pp. 1943–1948, May 2011.

[49] J. Teti, “Wide-band airborne radar operating considerations for low-altitude surveillance in the presence of specular multipath,” *IEEE Transactions on Antennas and Propagation*, vol. 48, no. 2, pp. 176–191, 2000.

[50] J. Rybak and R. Churchill, “Progress in reentry communications,” *IEEE Transactions on Aerospace and Electronic Systems*, vol. AES-7, no. 5, pp. 879–894, Sep. 1971.

[51] L. Shi, B. Guo, Y. Liu, and J. Li, "CHARACTERISTIC OF PLASMA SHEATH CHANNEL AND ITS EFFECT ON COMMUNICATION," *Progress In Electromagnetics Research*, vol. 123, pp. 321–336, 2012.

[52] R. P. Starkey, "Hypersonic vehicle telemetry blackout analysis," *Journal of Spacecraft and Rockets*, vol. 52, no. 2, pp. 426–438, Mar. 2015.

[53] J. Zhang, G. He, P. Bai, and N. Ge, "Dynamic channel modeling for communication through turbulent plasma sheath," in *2015 International Conference on Wireless Communications & Signal Processing (WCSP)*, IEEE, Oct. 2015.

[54] Z. Zhang and C. Gao, "Infrared measurement and composite tracking algorithm for air-breathing hypersonic vehicles," *Journal of Electronic Imaging*, vol. 27, no. 02, p. 1, Apr. 2018.

[55] L. Shi *et al.*, "Transmission channel characteristics of relay dual-polarization MIMO system for hypersonic vehicles under plasma sheath," *IEEE Transactions on Plasma Science*, pp. 1–11, 2018.

[56] E. Dirsa, "The telemetry and communication problem of re-entrant space vehicles," *Proceedings of the IRE*, vol. 48, no. 4, pp. 703–713, Apr. 1960.

[57] N. Mehra, R. K. Singh, and S. C. Bera, "MITIGATION OF COMMUNICATION BLACKOUT DURING RE-ENTRY USING STATIC MAGNETIC FIELD," *Progress In Electromagnetics Research B*, vol. 63, pp. 161–172, 2015.

[58] X. Gao and B. Jiang, "A matching approach to communicate through the plasma sheath surrounding a hypersonic vehicle," *Journal of Applied Physics*, vol. 117, no. 23, p. 233 301, Jun. 2015.

[59] J. B. Perurena, C. O. Asma, R. Theunissen, and O. Chazot, "Experimental investigation of liquid jet injection into mach 6 hypersonic crossflow," *Experiments in Fluids*, vol. 46, no. 3, pp. 403–417, Sep. 2008.

[60] R. Hartunian, G. Stewart, T. Curtiss, S. Fergason, R. Seibold, and P. Shome, "Implications and mitigation of radio frequency blackout during reentry of reusable launch vehicles," in *AIAA Atmospheric Flight Mechanics Conference and Exhibit*, American Institute of Aeronautics and Astronautics, Aug. 2007.

[61] G. L. Stuber, *Principles of Mobile Communication*, 4th. USA: Kluwer Academic Publishers, 2017, ISBN: 3319556142.

[62] L. Weiss, "Wavelets and wideband correlation processing," vol. 11, no. 1, pp. 13–32, Jan. 1994.

[63] J.-M. Munoz-Ferreras and R. Gomez-Garcia, “Beyond the stop-and-go assumption in pulse-doppler radar sensors,” *IEEE Sensors Journal*, vol. 14, no. 9, pp. 3046–3051, Sep. 2014.

[64] E. J. Kelly and R. P. Wishner, “Matched-filter theory for high-velocity, accelerating targets,” vol. 9, no. 1, pp. 56–69, 1965.

[65] M. Strom, “Waveform and receiver filter selection for wideband radar applications,” Ph.D. dissertation, Goteborg, Sweden, 2015.

[66] R. L. Peterson, D. E. Borth, and R. E. Ziemer, *An Introduction to Spread-Spectrum Communications*, 1st. USA: Prentice-Hall, Inc., 1995, ISBN: 0024316237.

[67] A. Polydoros and C. Weber, “A unified approach to serial search spread-spectrum code acquisition–part i: General theory,” *IEEE Transactions on Communications*, vol. 32, no. 5, pp. 542–549, 1984.

[68] C. O’Driscoll, “Performance analysis of the parallel acquisition of weak GPS signals,” Ph.D. dissertation, University College Cork, 2007.

[69] S. M. Kay, *Fundamentals of Statistical Signal Processing: Estimation Theory*. USA: Prentice-Hall, Inc., 1993, ISBN: 0133457117.

[70] ——, *Fundamentals of Statistical Signal Processing: Detection Theory*. USA: Prentice-Hall, Inc., 1998, ISBN: 013504135X.

[71] G. E. Corazza and R. Pedone, “Generalized and average likelihood ratio testing for post detection integration,” *IEEE Transactions on Communications*, vol. 55, no. 11, pp. 2159–2171, Nov. 2007.

[72] R. Ward, “Acquisition of pseudonoise signals by sequential estimation,” *IEEE Transactions on Communications*, vol. 13, no. 4, pp. 475–483, Dec. 1965.

[73] R. Ward and K. Yiu, “Acquisition of pseudonoise signals by recursion-aided sequential estimation,” *IEEE Transactions on Communications*, vol. 25, no. 8, pp. 784–794, Aug. 1977.

[74] J. Vlok, “Detection of direct sequence spread spectrum signals,” Ph.D. dissertation, University of Tasmania, 2014.

[75] H. L. V. Trees, *Detection, Estimation, and Modulation Theory: Radar-Sonar Signal Processing and Gaussian Signals in Noise*. Melbourne, FL, USA: Krieger Publishing Co., Inc., 1992, ISBN: 0894647482.

[76] M. Foucras, O. Julien, C. Macabiau, and B. Ekambi, “A novel computationally efficient Galileo E1 OS acquisition method for GNSS software receiver,” in *ION GNSS 2012, 25th International Technical Meeting of The Satellite Division of the Institute of Navigation*, Nashville, United States, Sep. 2012, pp 365–383.

[77] W. Zhang and M. Ghogho, “Improved fast modified double-block zero-padding (fmdbzp) algorithm for weak gps signal acquisition,” IEEE, 2010, pp. 1617–1621.

[78] H. Li, M. Lu, and Z. Feng, “Direct gps p-code acquisition method based on fft,” *Tsinghua Science and Technology*, vol. 13, no. 1, pp. 9–16, Feb. 2008.

[79] H. Li, M. Lu, X. Cui, and Z. Feng, “Generalized zero-padding scheme for direct gps p-code acquisition,” *IEEE Transactions on Wireless Communications*, vol. 8, no. 6, pp. 2866–2871, Jun. 2009.

[80] C. Yang, J. Vasquez, and J. Chaffee, “Fast direct p(y)-code acquisition using xfast,” *ION Journal of Navigation*, pp. 317–324, Sep. 1999.

[81] C. Yang, “Fast direct p(y)-code acquisition using xfast,” *ION Journal of Navigation*, pp. 137–147, Sep. 2001.

[82] H. Li, X. Cui, M. Lu, and Z. Feng, “Dual-folding based rapid search method for long pn-code acquisition,” *IEEE Transactions on Wireless Communications*, vol. 7, no. 12, pp. 5286–5296, Dec. 2008.

[83] S. M. Spangenberg, I. Scott, S. McLaughlin, G. J. Povey, D. G. Cruickshank, and P. M. Grant, “An FFT-based approach for fast acquisition in spread spectrum communication systems,” *Wireless Personal Communications*, vol. 13, no. 1, pp. 27–55, May 2000.

[84] R. A. Stirling-Gallacher, A. P. Hulbert, and G. J. R. Povey, “A fast acquisition technique for a direct sequence spread spectrum signal in the presence of a large Doppler shift,” in *Proceedings of ISSSTA’95 International Symposium on Spread Spectrum Techniques and Applications*, vol. 1, Sep. 1996, 156–160 vol.1.

[85] P. M. Grant, S. M. Spangenberg, I. Scott, S. McLaughlin, G. J. R. Povey, and D. G. M. Cruickshank, “Doppler estimation for fast acquisition in spread spectrum communication systems,” in *1998 IEEE 5th International Symposium on Spread Spectrum Techniques and Applications - Proceedings. Spread Technology to Africa (Cat. No.98TH8333)*, vol. 1, Sep. 1998, 106–110 vol.1.

[86] H. Saarnisaari and E. Karami, “Frequency domain block filtering GNSS receivers,” in *2008 IEEE/ION Position, Location and Navigation Symposium*, May 2008, pp. 159–166.

[87] E. Karami and H. Saarnisaari, “Windowed overlapped frequency domain block filtering approach for direct sequence signal acquisition,” *Digital Communications and Networks*, vol. 4, no. 3, pp. 209–216, Aug. 2018.

[88] M. Zarrabizadeh and E. Sousa, “A differentially coherent PN code acquisition receiver for CDMA systems,” *IEEE Transactions on Communications*, vol. 45, no. 11, pp. 1456–1465, 1997.

[89] C.-D. Chung, “Differentially coherent detection technique for direct-sequence code acquisition in a rayleigh fading mobile channel,” *IEEE Transactions on Communications*, vol. 43, no. 2/3/4, pp. 1116–1126, Feb. 1995.

[90] J. B.-Y. Tsui, *Fundamentals of Global Positioning System Receivers*. John Wiley & Sons, Inc., Nov. 2004.

[91] N. Ziedan, *GNSS receivers for weak signals*. Norwood, MA: Artech House, 2006, ISBN: 9781596930520.

[92] H. Luo, Y. Wang, Z. Ma, and S. Wu, “A segmentation motion compensation-based longterm integration method for DSSS signal,” in *2012 IEEE 11th International Conference on Signal Processing*, IEEE, Oct. 2012.

[93] Y. Guo, H. Huan, R. Tao, and Y. Wang, “Long-term integration based on two-stage differential acquisition for weak direct sequence spread spectrum signal,” *IET Communications*, vol. 11, no. 6, pp. 878–886, Mar. 2017.

[94] X. Ying and Y. Hong, “High-sensitivity acquisition of ultrahigh dynamic direct sequence spread spectrum signals in space communications,” *China Communications*, vol. 10, no. 10, pp. 26–36, Oct. 2013.

[95] Z. Zhang, W. Cheng, and H. Zhang, “Search-range-correction-based Doppler shift acquisition for space communications,” *IEEE Transactions on Vehicular Technology*, vol. 65, no. 5, pp. 3271–3284, May 2016.

[96] Y. Luo, L. Zhang, and H. Ruan, “An acquisition algorithm based on FRFT for weak GNSS signals in a dynamic environment,” *IEEE Communications Letters*, vol. 22, no. 6, pp. 1212–1215, Jun. 2018.

[97] Y. Luo, C. Yu, S. Chen, J. Li, H. Ruan, and N. El-Sheimy, “A novel Doppler rate estimator based on fractional Fourier transform for high-dynamic GNSS signal,” *IEEE Access*, vol. 7, pp. 29 575–29 596, 2019.

[98] S. Wu, J. Tian, and W. Cui, “A novel parameter estimation algorithm for DSSS signals based on compressed sensing,” *Chinese Journal of Electronics*, vol. 24, no. 2, pp. 434–438, Apr. 2015.

[99] X. Li, Z. Sun, W. Yi, G. Cui, and L. Kong, “Radar detection and parameter estimation of high-speed target based on MART-LVT,” *IEEE Sensors Journal*, vol. 19, no. 4, pp. 1478–1486, Feb. 2019.

[100] X. Li, G. Cui, W. Yi, and L. Kong, “Fast coherent integration for maneuvering target with high-order range migration via TRT-SKT-LVD,” *IEEE Transactions on Aerospace and Electronic Systems*, vol. 52, no. 6, pp. 2803–2814, Dec. 2016.

[101] J. Tian, W. Cui, and S. Wu, “A novel method for parameter estimation of space moving targets,” *IEEE Geoscience and Remote Sensing Letters*, vol. 11, no. 2, pp. 389–393, Feb. 2014.

[102] X. Li, G. Cui, W. Yi, L. Kong, and J. Yang, “Range migration correction for maneuvering target based on generalized keystone transform,” in *2015 IEEE Radar Conference (RadarCon)*, IEEE, May 2015.

[103] X. Chen, J. Guan, N. Liu, and Y. He, “Maneuvering target detection via Radon-fractional Fourier transform-based long-time coherent integration,” *IEEE Transactions on Signal Processing*, vol. 62, no. 4, pp. 939–953, Feb. 2014.

[104] P. Huang, G. Liao, Z. Yang, X.-G. Xia, J. Ma, and J. Zheng, “Ground maneuvering target imaging and high-order motion parameter estimation based on second-order keystone and generalized hough-HAF transform,” *IEEE Transactions on Geoscience and Remote Sensing*, vol. 55, no. 1, pp. 320–335, Jan. 2017.

[105] P. Jin, X. Rao, X. Zhu, F. Kan, and P. Jin, “Weak target integration detection based on bistatic radar second-order keystone transform,” in *2019 IEEE International Conference on Signal, Information and Data Processing (ICSIDP)*, IEEE, Dec. 2019.

[106] X. Lv, G. Bi, C. Wan, and M. Xing, “Lv's distribution: Principle, implementation, properties, and performance,” *IEEE Transactions on Signal Processing*, vol. 59, no. 8, pp. 3576–3591, Aug. 2011.

[107] X. Gu, Z. Zhao, and L. Shen, “Blind estimation of pseudo-random codes in periodic long code direct sequence spread spectrum signals,” *IET Communications*, vol. 10, no. 11, pp. 1273–1281, Jul. 2016.

[108] E. L. Lehmann and J. P. Romano, *Testing statistical hypotheses*, Third, ser. Springer Texts in Statistics. New York: Springer, 2005, pp. xiv+784, ISBN: 0-387-98864-5.

[109] G. Burel, C. Bouder, and O. Berder, “Detection of direct sequence spread spectrum transmissions without prior knowledge,” in *GLOBECOM'01. IEEE Global Telecommunications Conference (Cat. No.01CH37270)*, vol. 1, Nov. 2001, 236–239 vol.1.

[110] Z. Zhang and J. Lei, “A detecting algorithm of dsss signal based on auto — correlation estimation,” in *2017 IEEE 2nd Advanced Information Technology, Electronic and Automation Control Conference (IAEAC)*, 2017, pp. 137–141.

[111] L. Chang, F. Wang, and Z. Wang, “Detection of dsss signal in non-cooperative communications,” in *2006 International Conference on Communication Technology*, 2006, pp. 1–4.

[112] X. Zhang, S. Li, and Z. Chen, “A dsss signal detection method based on wavelet decomposition and delay multiplication,” in *2018 IEEE Asia-Pacific Conference on Antennas and Propagation (APCAP)*, Aug. 2018, pp. 341–343.

[113] Z. Deng, L. Shen, N. Bao, B. Su, J. Lin, and D. Wang, “Autocorrelation based detection of dsss signal for cognitive radio system,” in *2011 International Conference on Wireless Communications and Signal Processing (WCSP)*, Nov. 2011, pp. 1–5.

[114] J. D. Vlok and J. C. Olivier, “Non-cooperative detection of weak spread-spectrum signals in additive white gaussian noise,” *IET Communications*, vol. 6, no. 16, pp. 2513–2524, Nov. 2012.

[115] J. D. Vlok and J. C. Olivier, “Blind sequence-length estimation of low-snr cyclostationary sequences,” *IET Communications*, vol. 8, no. 9, pp. 1578–1588, Jun. 2014.

[116] V. Le Nir and B. Scheers, “Robust blind carrier frequency synchronisation for direct sequence spread spectrum systems,” *Electronics Letters*, vol. 51, no. 5, pp. 425–427, 2015.

[117] G. Burel and C. Bouder, “Blind estimation of the pseudo-random sequence of a direct sequence spread spectrum signal,” in *MILCOM 2000 Proceedings. 21st Century Military Communications. Architectures and Technologies for Information Superiority (Cat. No.00CH37155)*, vol. 2, 2000, 967–970 vol.2.

[118] S. Mehboodi, A. Jamshidi, and M. Farhang, “Two algorithms for spread-spectrum sequence estimation for dsss signals in non-cooperative communication systems,” in *2016 24th Iranian Conference on Electrical Engineering (ICEE)*, May 2016, pp. 72–76.

[119] Zhang Yu, Chen Yong, and Wu Hao, “Chip rate estimation of weak dsss signals based on improved delay-multiply in non-cooperative communication systems,” in *2012 IEEE 14th International Conference on Communication Technology*, Nov. 2012, pp. 138–142.

[120] X. Wenlong, Z. Yuanping, G. Qinggong, and M. Qingdang, "Blind estimation of long-code dsss signals based on information symbol transition pattern," in *2016 IEEE 13th International Conference on Signal Processing (ICSP)*, Nov. 2016, pp. 1161–1164.

[121] P. Y. Qiu, Z. T. Huang, W. L. Jiang, and C. Zhang, "Blind classification of the short-code and the long-code direct sequence spread spectrum signals," *IET Signal Processing*, vol. 4, no. 1, pp. 78–88, Feb. 2010.

[122] A. Tadaion, M. Derakhtian, S. Gazor, M. Nayebi, and M. Aref, "Signal activity detection of phase-shift keying signals," *IEEE Transactions on Communications*, vol. 54, no. 8, pp. 1439–1445, Aug. 2006.

[123] T. Fusco, L. Izzo, A. Napolitano, and M. Tanda, "On the second-order cyclostationarity properties of long-code ds-ss signals," *IEEE Transactions on Communications*, vol. 54, pp. 1741–1746, 10 2006.

[124] K. S. Bialkowski, I. V. L. Clarkson, and S. D. Howard, "Generalized canonical correlation for passive multistatic radar detection," in *2011 IEEE Statistical Signal Processing Workshop (SSP)*, IEEE, Jun. 2011.

[125] N. Vankayalapati and S. Kay, "Asymptotically optimal detection of low probability of intercept signals using distributed sensors," *IEEE Transactions on Aerospace and Electronic Systems*, vol. 48, no. 1, pp. 737–748, Jan. 2012.

[126] J. Liu, H. Li, and B. Himed, "Two target detection algorithms for passive multistatic radar," *IEEE Transactions on Signal Processing*, vol. 62, no. 22, pp. 5930–5939, Nov. 2014.

[127] G. Cui, J. Liu, H. Li, and B. Himed, "Signal detection with noisy reference for passive sensing," *Signal Processing*, vol. 108, pp. 389 –399, 2015.

[128] S. Gogineni, P. Setlur, M. Rangaswamy, and R. R. Nadakuditi, "Passive radar detection with noisy reference channel using principal subspace similarity," *IEEE Transactions on Aerospace and Electronic Systems*, vol. 54, no. 1, pp. 18–36, Feb. 2018.

[129] H. Urkowitz, "Energy detection of unknown deterministic signals," *Proceedings of the IEEE*, vol. 55, no. 4, pp. 523–531, 1967.

[130] A. Sonnenschein and P. Fishman, "Radiometric detection of spread-spectrum signals in noise of uncertain power," *IEEE Transactions on Aerospace and Electronic Systems*, vol. 28, no. 3, pp. 654–660, Jul. 1992.

[131] R. Tandra and A. Sahai, “SNR walls for signal detection,” *IEEE Journal of Selected Topics in Signal Processing*, vol. 2, no. 1, pp. 4–17, Feb. 2008.

[132] E. Axell, G. Leus, and E. G. Larsson, “Overview of spectrum sensing for cognitive radio,” in *2010 2nd International Workshop on Cognitive Information Processing*, IEEE, Jun. 2010.

[133] T. Yucek and H. Arslan, “A survey of spectrum sensing algorithms for cognitive radio applications,” *IEEE Communications Surveys & Tutorials*, vol. 11, no. 1, pp. 116–130, 2009.

[134] F. Peng, H. Chen, and B. Chen, “On energy detection for cooperative spectrum sensing,” in *2012 46th Annual Conference on Information Sciences and Systems (CISS)*, IEEE, Mar. 2012.

[135] S. Gezici, Z. Sahinoglu, and H. Poor, “On the optimality of equal gain combining for energy detection of unknown signals,” *IEEE Communications Letters*, vol. 10, no. 11, pp. 772–774, Nov. 2006.

[136] W. A. Gardner, “Signal interception: A unifying theoretical framework for feature detection,” *IEEE Transactions on Communications*, vol. 36, no. 8, pp. 897–906, Aug. 1988.

[137] A. Sahai, N. Hoven, and R. Tandra, “Some fundamental limits on cognitive radio,” in *Proceedings of the Allerton Conference on Control, Communications, and Computation*, 2004.

[138] E. Axell and E. G. Larsson, “Optimal and sub-optimal spectrum sensing of OFDM signals in known and unknown noise variance,” *IEEE Journal on Selected Areas in Communications*, vol. 29, no. 2, pp. 290–304, Feb. 2011.

[139] D. M. Lin, J. B. Tsui, and D. Howell, “Direct P(Y)-Code Acquisition Algorithm forSoftware GPS Receivers,” in *Proceedings of the 12th International Technical Meeting of the Satellite Division of The Institute of Navigation*, Nashville, United States, Sep. 1999, pp 363–368.

[140] J. W. Cooley and J. W. Tukey, “An algorithm for the machine calculation of complex Fourier series,” *Mathematics of Computation*, vol. 19, no. 90, pp. 297–297, May 1965.

[141] M. Richards, *Fundamentals of Radar Signal Processing*, ser. Professional Engineering. Mcgraw-hill, 2005, ISBN: 9780071444743.

[142] D. A. Chu and J. R. Barry, “Direct-sequence spread-spectrum acquisition for high dynamic environments via signal partitioning,” in *MILCOM 2021 - 2021 IEEE Military Communications Conference (MILCOM)*, IEEE, Nov. 2021.

[143] N. Ziedan and J. Garrison, “Unaided acquisition of weak GPS signals using circular correlation or double-block zero padding,” in *PLANS 2004. Position Location and Navigation Symposium (IEEE Cat. No.04CH37556)*, IEEE.

[144] W. Hurd, J. Statman, and V. Vilnrotter, “High dynamic GPS receiver using maximum likelihood estimationand frequency tracking,” *IEEE Transactions on Aerospace and Electronic Systems*, vol. AES-23, no. 4, pp. 425–437, Jul. 1987.

[145] Y. Shen and Y. Xu, “Analysis of the code phase migration and Doppler frequency migration effects in the coherent integration of direct-sequence spread-spectrum signals,” *IEEE Access*, vol. 7, pp. 26 581–26 594, 2019.

[146] K. M. Scott, W. C. Barott, and B. Himed, “The keystone transform: Practical limits and extension to second order corrections,” in *2015 IEEE Radar Conference (RadarCon)*, IEEE, May 2015.

[147] R. P. Perry, R. C. DiPietro, and R. L. Fante, “SAR imaging of moving targets,” *IEEE Transactions on Aerospace and Electronic Systems*, vol. 35, no. 1, pp. 188–200, Jan. 1999.

[148] E. Sejdić, I. Djurović, and L. Stanković, “Fractional fourier transform as a signal processing tool: An overview of recent developments,” *Signal Processing*, vol. 91, no. 6, pp. 1351–1369, Jun. 2011.

[149] A. Serbes and O. Aldimashki, “A fast and accurate chirp rate estimation algorithm based on the fractional Fourier transform,” in *2017 25th European Signal Processing Conference (EUSIPCO)*, IEEE, Aug. 2017.

[150] L. Almeida, “The fractional Fourier transform and time-frequency representations,” *IEEE Transactions on Signal Processing*, vol. 42, no. 11, pp. 3084–3091, 1994.

[151] A. Serbes, “On the estimation of LFM signal parameters: Analytical formulation,” *IEEE Transactions on Aerospace and Electronic Systems*, vol. 54, no. 2, pp. 848–860, Apr. 2018.

[152] H.-B. Sun, G.-S. Liu, H. Gu, and W.-M. Su, “Application of the fractional Fourier transform to moving target detection in airborne SAR,” *IEEE Transactions on Aerospace and Electronic Systems*, vol. 38, no. 4, pp. 1416–1424, Oct. 2002.

[153] B. Deng, J. bao Luan, and S. qi Cui, “Analysis of parameter estimation using the sampling-type algorithm of discrete fractional Fourier transform,” *Defence Technology*, vol. 10, no. 4, pp. 321–327, Dec. 2014.

[154] Y. Guo, H. Huan, R. Tao, and Y. Wang, “Frequency tracking loop with wide pull-in range for weak DSSS signal,” *Electronics Letters*, vol. 54, no. 23, pp. 1336–1338, Nov. 2018.

[155] C. Candan, M. Kutay, and H. Ozaktas, “The discrete fractional fourier transform,” *IEEE Transactions on Signal Processing*, vol. 48, no. 5, pp. 1329–1337, May 2000.

[156] L. Zheng and D. Shi, “Maximum amplitude method for estimating compact fractional fourier domain,” *IEEE Signal Processing Letters*, vol. 17, no. 3, pp. 293–296, Mar. 2010.

[157] D. A. Chu and J. R. Barry, “The case against alphabet awareness for detection of direct-sequence spread-spectrum signals,” *Signal Processing*, vol. 194, p. 108 449, May 2022.

[158] M. Abramowitz, *Handbook of Mathematical Functions, With Formulas, Graphs, and Mathematical Tables,* USA: Dover Publications, Inc., 1974, ISBN: 0486612724.

[159] A. Nuttall, “Some integrals involving the Q_M function,” *IEEE Transactions on Information Theory*, vol. 21, no. 1, pp. 95–96, Jan. 1975.

[160] R. J. Muirhead, Ed., *Aspects of Multivariate Statistical Theory*. John Wiley & Sons, Inc., Mar. 1982.

[161] M. Kang and M. Alouini, “Largest eigenvalue of complex wishart matrices and performance analysis of MIMO MRC systems,” *IEEE Journal on Selected Areas in Communications*, vol. 21, no. 3, pp. 418–426, Apr. 2003.

[162] O. Zeitouni, J. Ziv, and N. Merhav, “When is the generalized likelihood ratio test optimal?” *IEEE Transactions on Information Theory*, vol. 38, no. 5, pp. 1597–1602, 1992.

[163] J. Gabriel and S. Kay, “On the relationship between the GLRT and UMPI tests for the detection of signals with unknown parameters,” *IEEE Transactions on Signal Processing*, vol. 53, no. 11, pp. 4194–4203, Nov. 2005.

[164] S. Kay and J. Gabriel, “An invariance property of the generalized likelihood ratio test,” *IEEE Signal Processing Letters*, vol. 10, no. 12, pp. 352–355, Dec. 2003.

[165] N. Johnson, S Kotz, and N. Balakrishnan, *Continuous Univariate Distributions*, 2nd ed. New York: John Wiley, 1996, vol. 2, ISBN: 978-0-471-58494-0.

[166] A. Haidar, P. Luszczek, and J. Dongarra, "New algorithm for computing eigenvectors of the symmetric eigenvalue problem," in *2014 IEEE International Parallel & Distributed Processing Symposium Workshops*, IEEE, May 2014.

[167] M. Ferranti and R. Vandebril, "Computing eigenvalues of normal matrices via complex symmetric matrices," *Journal of Computational and Applied Mathematics*, vol. 259, pp. 281–293, Mar. 2014.

[168] V. Y. Pan and Z. Q. Chen, "The complexity of the matrix eigenproblem," in *Proceedings of the thirty-first annual ACM symposium on Theory of computing - STOC '99*, ACM Press, 1999.

[169] J. A. Högbom, "Aperture synthesis with a non-regular distribution of interferometer baselines," *Astronomy and Astrophysics Supplement*, vol. 15, p. 417, Jun. 1974.

VITA

Derrick Albert Chu was born in Albany, NY, in 1993. He received his B.S. degree in electrical engineering from the University of California Los Angeles (UCLA) in 2015 and M.S. degree in electrical engineering from Georgia Institute of Technology in 2017. He is currently working towards the Ph.D. degree at Georgia Institute of Technology.